

Copyright by

LAURENCE ALBERT SODERBLOM

1970

THE DISTRIBUTION AND AGES OF REGIONAL
LITHOLOGIES IN THE LUNAR MARIA

Thesis by

Laurence Albert Soderblom

In Partial Fulfillment of the Requirements
For the Degree of
Doctor of Philosophy

California Institute of Technology

Pasadena, California

.1970

(Submitted April 28, 1970)

ACKNOWLEDGEMENTS

Two individuals, Dr. Bruce C. Murray and Dr. Eugene M. Shoemaker, are principally responsible for engendering my interest in the problems of lunar geology and for encouraging me in the completion of this research. Dr. Shoemaker initially introduced me to the problem of small impact erosion and suggested that it might be tractable. Discussions with Dr. Murray on the geological interpretation of spectral reflectance measurements were indispensable.

I would like to thank Mrs. Thedra A. McMillian, Miss Carmen Longo, and Mr. Jurrie J. van der Woude who devoted much of their free time to the completion of this manuscript. Mrs. Margaret Lagus provided many helpful editorial suggestions.

The author was supported by a National Aeronautics and Space Administration Traineeship during this research. Most of the research expenses were covered under NASA Grant NGL 05-002-003.

ABSTRACT

A research program was designed (1) to map regional lithological units of the lunar surface based on measurements of spatial variations in spectral reflectance, and, (2) to establish the sequence of the formation of such lithological units from measurements of the accumulated effects of impacting bodies.

Spectral reflectance data were obtained by scanning luminance variations over the lunar surface at three wavelengths (0.4μ , 0.52μ , and 0.7μ). These luminance measurements were reduced to normalized spectral reflectance values relative to a standard area in Mare Serenitatis. The spectral type of each lunar area was identified from the shape of its reflectance spectrum. From these data lithological units or regions of constant color were identified. The maria fall into two major spectral classes: circular maria like Mare Serenitatis contain S-type or red material and thin, irregular, expansive maria like Mare Tranquillitatis contain T-type or blue material. Four distinct subtypes of S-type reflectances and two of T-type reflectances exist. As these six subtypes occur in a number of lunar regions, it is concluded that they represent specific types of material rather than some homologous set of a few end members.

The relative ages or sequence of formation of these mare units were established from measurements of the accumulated impacts which have occurred since mare formation. A model was developed which relates the integrated flux of particles which have impacted a surface to the distribution of craters as functions of size and shape. Erosion of craters is caused chiefly by small bodies which produce negligible individual changes in crater shape. Hence the shape of a crater can be used to estimate the total number of small

impacts that have occurred since the crater was formed. Relative ages of a surface can then be obtained from measurements of the slopes of the walls of the oldest craters formed on the surface. The results show that different maria and regions within them were emplaced at different times. An approximate absolute time scale was derived from Apollo 11 crystallization ages under an assumption of a constant rate of impacting for the last 4×10^9 yrs. Assuming, constant flux, the period of mare formation lasted from over 4×10^9 yrs to about 1.5×10^9 yrs ago.

A synthesis of the results of relative age measurements and of spectral reflectance mapping shows that (1) the formation of the lunar maria occurred in three stages; material of only one spectral type was deposited in each stage, (2) two distinct kinds of maria exist, each type distinguished by morphology, structure, gravity anomalies, time of formation, and spectral reflectance type, and (3) individual maria have complicated histories; they contain a variety of lithic units emplaced at different times.

TABLE OF CONTENTS

<u>Chapter</u>	<u>Page</u>
I. INTRODUCTION	1
Summary of Previous Work	3
Scope and Approach.	11
II. SPECTRAL REFLECTANCE MAPPING	14
Introduction.	14
Instrumentation and Observation	15
Data Reduction and Boundary Recognition	17
Classification of Spectral Types	18
Compilation of Regional Maps	25
Discussion of Results.	38
Comparison with Previous Studies	39
Summary and Conclusions	41
III. DETERMINATION OF RELATIVE AGE FROM CRATER MORPHOLOGY	43
Introduction.	43
Impact Erosion Model	45
Method of Determination of Relative Age	51
Discussion of Results.	56
Comparison with Previous Work.	56
Calibration of Relative Age Determinations with Preliminary Age Results from Apollo 11 and 12	59
Conclusions	62
IV. THE SEQUENCE OF FORMATION OF REGIONAL MARE UNITS	64

TABLE OF CONTENTS (CONT.)

<u>Chapter</u>	<u>Page</u>
IV. (CONT.)	
Major Stages of Mare Formation	64
Sequence and Distribution of Lithologies in Individual Maria	66
Conclusions	69
APPENDICIES	
I. SPECTRAL REFLECTANCE MAPPING: OBSERVATIONAL TECHNIQUES AND DATA REDUCTION.	72
II. A MODEL FOR SMALL-IMPACT EROSION APPLIED TO THE LUNAR SURFACE	91
III. A TECHNIQUE FOR OBTAINING RELATIVE AGES FOR REGIONS OF THE LUNAR SURFACE	115
IV. RELATIVE AGE DATA	131
LIST OF REFERENCES	137

LIST OF ILLUSTRATIONS

<u>Number</u>	<u>Page</u>
1. Bivariate frequency distribution of lunar spectra (all data).	20
2. Bivariate frequency distributions of two independent sets of data	21
3. The regions used to classify reflectance values along scans	26
4. The positions of grids on the lunar surface and the distribution of each type along scans in the grids	28
5. and 6. The distributions of the seven spectral types in the Mare Serenitatis and Mare Tranquillitatis regions	37
7. The predicted ratio of unshadowed to shadowed craters as a function of diameter	54

LIST OF ILLUSTRATIONS (CONT.)

<u>Number</u>	<u>Page</u>
8. Comparison of observed and predicted ratios of unshadowed to shadowed craters	55
9. Relative ages of mare units and major craters.	57
10. Absolute ages of Apollo landing sites assuming a constant impact flux	61
11. Spectral reflectance type and relative age of units in the lunar maria	65
12. Comparison of ages, regional morphologies and spectral reflectance types of units in the lunar maria	71
13. The transmissions of the three narrow band filters	77
14. Data reduction sequence for spectral reflectance measurements	79
15. The step-function model boundary and its output form	82
16. Location of color boundaries.	83
17. The bivariate distribution of lunar reflectance spectra and the region defined for each type	85
18. Stages in the construction of regional maps	87
19. Comparison of normalized relative reflectance values with those measured by McCord (1968)	88
20. Comparison of albedo and color variations across the upland-Mare Crisium boundary	90
21. The observed distribution of craters in the lunar maria	95
22. The geometry of the trajectories of material ejected from a crater formed on a slope	98
23. The evolution of the idealized crater considered in the model	106
24. The ratio of R_{\max} to crater radius as a function of slope.	108
25. Comparison of observed and predicted size - frequency distributions of craters	118

LIST OF ILLUSTRATIONS (CONT.)

<u>Number</u>		<u>Page</u>
26.	Frequency of craters as a function of the slope of the crater wall	120
27.	The predicted ratio of unshadowed to shadowed craters as a function of crater diameter	123
28.	Comparison of the observed and predicted ratio of unshadowed to shadowed craters	126

LIST OF TABLES

<u>Number</u>		<u>Page</u>
1.	Comparison of maxima positions in two data sets	23
2.	The positions and radii of the regions used to classify the reflectance spectra along scans	27
3.	Comparison of results from direct crater counting (C_s) and regolith thickness determinations with relative age measurements	59
4.	Dependence of erosion rate on ejecta profile of eroding crater	100
5.	Comparison of determinations of relative ages of individual surfaces from different photographs	125
6.	Comparison of relative ages determined for various areas in Oceanus Procellarum	127

1. INTRODUCTION

It has become increasingly apparent in the last few years that the surfaces of the moon and Mars contain important records of the early history of the environment of the solar system. For the most part, such a record is no longer preserved in the crust of the earth. The ancient morphologies of the moon and Mars are still to a large extent preserved. Detailed accounts of the time variations of the abundance and the distribution of cometary and asteroidal bodies, the history and evolution of the solar wind and radiation, and possibly other phenomena which are as yet undiscovered can be obtained from the study of these surfaces.

The impact flux histories recorded on the moon and Mars have been distorted to a considerable extent as on the earth by processes related to the planetary interiors and, in the case of Mars, to the atmosphere which modify and redistribute material. Consequently, the geologic development of these planetary surfaces must be understood before the effects of impact can be individually interpreted. Furthermore, the geologic history places important constraints on theories of the formation and evolution of the planetary interior. The intent of this study is to develop the basic framework of the geologic evolution of the lunar maria, and to extract from this information the flux history of asteroids and comets in the earth-moon environment.

The extent to which the lunar geologic history can be understood

depends on the identification of the compositional, morphological, structural, and historical relationships between the various lunar terrains. Only with this information is it possible to infer, in a geologic sense, the genetic processes, time scales, and chronology of surface evolution. It is unlikely that sample return from a few localities will by itself yield this information over a sufficiently large fraction of the surface. It then becomes necessary to develop and apply techniques to determine variations in the mineralogy, texture, and age. Such methods rely on earth-based and spacecraft measurements of the nature in which a surface reflects or emits radiant energy or, in the case of age determination, the extent to which the surface has been altered by the accumulation of impacts. For the most part these techniques can yield only relative differences in composition and age. When calibrated with isotope ages and chemical information obtained directly from the Apollo samples, however, they provide powerful tools for extending to large regions the knowledge of the chemical nature and absolute ages of a few rock samples.

The intent of this study is to identify the distributions and sequences of formation of lithologies in the lunar maria and to extract from this information the flux history for the last several billion years of asteroids and comets in the earth-moon vicinity. The technique used here to map the distributions of various lunar lithologies is based on measurements of the visible spectral reflectance. The relative ages of these lithologies were determined from investigations of the distributions in shape and size of small craters

(diameters <1 kilometer). Before presenting the details of these techniques and the results of their application, it is appropriate to briefly outline the available knowledge obtained from earth-based observations and from unmanned and manned space flights.

SUMMARY OF PREVIOUS WORK

Texture and Composition: Earth-Based and Surveyor Observations

Visible reflectance. Recent studies of the wavelength-dependent reflectance (0.4μ to 1.1μ) of numerous areas on the lunar surface (McCord, 1968; McCord and Johnson, 1969) have shown that (1) differences of the order of 10% exist among the relative reflectance spectra of a large number of areas, (2) this range of variation is considerably smaller than the equivalent range for terrestrial rocks, (3) the lunar spectra fall into groups indicating a variety of distinct types rather than general mixtures of a few types, and, (4) the reflectance spectra do not appear to be uniquely related to morphology or texture, suggesting that the differences between reflectance spectra are related instead to compositional and/or mineralogical differences.

Far infrared emissivity. Measurements of infrared emissivity differences between lunar regions (8.2μ to 13.4μ) by Goetz (1968) and Goetz and Soderblom (1969) indicate (1) that the lunar surface is very uniform in texture, and, (2) that the silicon-oxygen polymerization is very constant over the surface, suggesting fairly uniform mineralogy by comparison to the variations among terrestrial rock types.

Only two areas (Plato and East Humorum) were observed by Goetz (1968) to show detectable differences from the average surface in infrared emissivity. Major differences between areas in either silicate structure or surface texture can create such observable emissivity differences. Surveyor studies of the fine texture of lunar surface support the conclusion that most of the particles are smaller than 60 microns on both young surfaces such as Tycho ejecta and older surfaces such as Mare Tranquillitatis. It is therefore likely that the infrared emissivity anomalies found in Plato and Mare Humorum are due to different assemblages of silicates exposed in these areas compared to the bulk of the lunar surfaces. Again, these differences are small compared to the total variation that exists in terrestrial igneous rocks.

Broad band thermal emission. Observations of variations in far infrared brightness temperature during periods of varying insolation have provided information about the thermal inertia of the lunar surface. Studies of eclipse cooling (Petit and Nicholson, 1930; Petit, 1940; Sinton, 1962; and Shorthill and Saari, 1969) and measurements of nighttime cooling (Murray and Wildey, 1964) are compatible with a uniform, thick dust layer on the lunar surface. The similar thermal properties of maria and uplands suggest similar dust layers in those regions. Fresh-rayed craters usually show anomalies indicative of a higher percentage of more conductive material, for example, rocks exposed on those surfaces.

Radar reflectivity and radio emission. Radar and radio measurements of the electromagnetic properties and roughness of the lunar surface have

been made by numerous observers from both earth-based observatories and spacecraft radars. Measurements of radar cross-section at wavelengths between a few centimeters and a few meters yield dielectric constants compatible with a loosely compacted silicate material to depths of at least a few meters (Muhleman, et al., 1969; Hagfors, et al., 1969). Radio emission measurements give a somewhat lower dielectric constant (Troitsky, 1965). By taking surface roughness into account, this lower dielectric constant can be corrected to agree with the higher value determined from radar reflectivity. (Hagfors, 1970; Hansen and Muhleman, 1970). These data indicate that the near surface density of the lunar regolith is between 1 and 2 gm/cc depending on the solid dielectric constant (Muhleman, et al., 1969). Measurements of the dielectric constant of the Apollo 11 surface fines as a function of porosity have confirmed the results obtained from earth-based and spacecraft radar (Gold, et al., 1970).

Cross-polarized radar reflectivity measurements have been used to estimate the surface roughness at scales of a few centimeters. Maps made at a wavelength of 3 centimeters indicate that (1) the roughness at this scale is fairly uniform over and between regional provinces (uplands and maria), and, (2) the roughness is considerably higher on fresh young craters which is compatible with a higher percentage of rocks and clumps exposed on those surfaces (Lincoln Laboratory Report, V.2, 1968).

Comparison with Surveyor measurements. The Surveyor results which are relevant to this section include studies of the size-frequency distribution of exposed particles, measurements of regolith thickness, determinations of the near surface mechanical properties, and chemical data obtained in the α -scattering experiments. It is important to compare the Surveyor results for different landing sites in order to test the conclusions described above, which were based on the comparison of remote observations of these sites.

Television observations at all Surveyor sites have shown that more than 80% of the surface is covered by particles smaller than 1 mm. Studies of Surveyor footpad imprints at various sites by Jaffe (1969) indicate that the mid-point of the particle distribution occurs at about 10μ and the bulk of the material is composed of 2 to 60μ particles. Although the bulk of the material at the Tycho site was the same as at other sites, the frequency of rocks larger than 50 cm was at least a factor of ten higher here than at any other site.

The regolith thicknesses at the various Surveyor sites were obtained by studying the distribution of craters penetrating the regolith whose rims were blanketed by large rock fragments (Shoemaker, et. al., 1969). It was found that the average depth of the regolith at the Surveyor I, III, V, and VI sites was of the order of a few meters. The depth at the Surveyor VII site (Tycho) was only about 10 cm.

The measurements of bearing strength and general behavior of near surface materials are compatible with a loosely compacted fine-grained layer with density of about 1.5 gm/cc (Scott and Roberson, 1968).

Surveyors V, VI, and VII were provided with α -scattering instruments to obtain information on the general chemical nature of the surface. Analysis of these data by Turkevich, et. al., (1969) indicate that (1) the three areas studied have nearly identical composition which suggests that surface composition may be very uniform over the moon, (2) the upland site (Surveyor VII) differs from the two maria sites primarily in lower abundance of iron-group minerals, and (3) the chemical abundances of lunar rocks are most similar to those of terrestrial basalts.

Conclusions. Using the earth-based and Surveyor data described above, several strong conclusions may be drawn concerning the chemical and textural character of the surface and the magnitude and nature of variations in these properties over the moon. These conclusions set the stage for interpreting the new observations presented in this thesis.

Conclusions regarding the general chemical nature of the lunar surface are as follows:

- a. The surface materials have a composition similar to terrestrial basalts (α -scattering).
- b. The compositional differences between lunar regions are small compared to the variations over the spectrum of terrestrial igneous rocks

(α -scattering, visible relative reflectivity, and far infrared emissivity).

c. Compositional differences that do exist between regions are in part related to minor variations in iron-group abundance (α -scattering and visible relative reflectance) and to small variations in SiO polymerization (infrared emissivity), the former being more common.

Similarly, the conclusions about particle size distribution, thickness and porosity of the lunar regolith, and variations in these parameters between different lunar regions can be stated as follows:

a. The lunar regolith extends to depths of at least several meters over most of the lunar uplands and maria (radar cross-section and Surveyor studies). The regolith depth on fresh young features such as Tycho flows is about 10 cm.

b. Most of the surface material in the regolith is finer than 60μ (including the regolith on fresh craters) (infrared emissivity and Surveyor studies).

c. The density of the near surface regolith is about 1.5 gm/cc (radar cross-section and Surveyor studies).

d. Fresh rayed craters are characterized by a higher concentration of larger rock fragments compared to most of the surface (cross-polarized radar reflection, infrared thermal emission, Surveyor television studies).

Implications of Apollo 11 and 12 Samples

The return of lunar material by two recent Apollo landings has provided new information which has dramatic relevance to the above discussions. Preliminary studies have confirmed most of the conclusions in the preceding section and have left the rest unresolved. The samples returned from the Apollo 11 and 12 landing sites are similar to terrestrial basalt. The sites differ primarily in the abundance of ferro-magnesium elements.

These data confirm the conclusions about chemical variation derived from visible reflectivity, far infrared emissivity, and Surveyor α -scattering studies. The more "acidic" rock found at the Apollo 12 site (sample 12013) indicates that some variation in bulk SiO polymerization does exist on the moon. The spectrum of types of lunar rocks remains narrow by comparison to the total terrestrial variation.

Probably the most important data provided by the Apollo missions concerning lunar geologic history are the absolute crystallization ages of the surface materials. Ages of the Mare Tranquillitatis basalts are in the neighborhood of 4×10^9 years. Preliminary results from Apollo 12 rock samples indicate ages somewhat younger, perhaps the order of a billion years younger. The fine material in the regolith indicates an older age ($\sim 4.5 \times 10^9$ years). The discrepancy between the ages of the rocks and overlying regolith is presently unresolved, but evidence indicates there may be contamination of the fines by materials transported from other areas

(Silver, 1970). It is improbable, however, that the process of impact mixing has produced a uniform surface layer over the entire moon since (1) the fines at both Apollo sites are compositionally similar to underlying rocks, and (2) regional albedo boundaries are sharp to about two kilometers.

The results of the Apollo sample studies establish important calibration for earth-based measurements and morphology studies used to measure relative differences in composition and age.

General Chronology of Lunar Surface Evolution

Studies of large scale lunar morphology from earth-based, Ranger, and Orbiter photography have yielded important information concerning the general sequence of events in lunar history. Chronological order can be inferred from superposition of various formations, features, and structures; for example, craters flooded with mare material are assumed older than the flooding event, and ejecta blankets which lie on top of formations are assumed to be younger than those formations. From such studies four stratigraphic time units in the lunar geological record have been identified by Shoemaker and Hackman (1962). The chronological order of these four periods is based on three important events: (1) the formation of the Imbrium structure and associated ejecta blankets, (2) the filling of the lunar maria, and, (3) the formation of the crater Eratosthenes, whose rays are only barely still visible. Pre-Imbrium time is defined as that

period before the formation of the Imbrium structure with its associated ejecta and debris patterns. During this period most of the large subdued lunar craters which exist in the uplands and various mare basins were formed. A period of time known as the Imbrian commenced at the formation of the Imbrium basin and its associated ejecta (Fra Mauro Formation). The Imbrian includes the extensive dark deposits that flooded the mare basins. It is extremely difficult to subdivide the Procellarum Group (mare deposits) using superposition criteria because of the strong morphological similarities between different maria. The Eratosthenian includes craters which postdate the period of mare filling but are old enough that their associated ray patterns are no longer visible. The Copernician period extended from the formation of Eratosthenes to the present. Included in this period are the formation of young features such as Tycho, Kepler, Aristarchus, and Copernicus. Although the relative durations of the four lunar periods are not known, the suggested sequence provides a necessary framework for discussion of the new results presented in this study.

SCOPE AND APPROACH

The preceding discussion of the general chronology and compositional and textural character of the lunar surface provides a framework for understanding the approach and relevance of the studies presented in this thesis.

The research program can be divided into two parts. The first involves the development and application of a technique to map regional variations in visible spectral reflectance (0.4μ to 0.7μ). Of the previously described remote sensing techniques such color mapping is the only one known to be sensitive to the minor compositional differences reported between the various Surveyor and Apollo landing sites. On the basis of such a mapping program it has been possible to establish regional units of constant spectral reflectance. These in turn represent to some degree regions of homogeneous composition. A discussion of the results and conclusions and a brief outline of the technique are presented in Chapter II. A more detailed description of the observational technique and data reduction is provided in Appendix I.

The second goal of this program was to establish the ages of the lithologies mapped in the spectral reflectance study. A model of impact erosion was developed and applied to lunar photography to obtain relative ages of various regions. Absolute ages were obtained through calibrating relative ages with preliminary crystallization ages from Apollo 11 and 12 samples. The results of the morphological age dating and calibration from Apollo samples are discussed in Chapter III. The complete development of the erosion model and the details of the photographic age dating methods are presented in Appendices II and III, respectively.

Chapter IV presents the synthesis of the spectral mapping and age dating studies in an attempt to establish the sequence of events within the

period of mare formation. The ages and distributions of lithologies in the lunar maria are related in that chapter to the overall time scales of lunar geologic history, episodes of mare formation within individual maria, the regional morphologies of and structures associated with individual maria, and three major stages of mare flooding which are correlated with the spectral reflectances of the units which they produced.

II. SPECTRAL REFLECTANCE MAPPING

INTRODUCTION

A detailed laboratory study of reflectance spectra of igneous rocks (Adams and Filice, 1967) has shown that the spectra are related chiefly to elemental composition, mineralogy, and particle size. Adams (1968) demonstrated that electronic absorption bands that occur in silicate spectra are caused by iron-group transition elements in various coordination and valence states. Observations of McCord (1968) have shown that lunar reflectance spectra are not strongly correlated with morphology or albedo, suggesting that differences in relative reflectance are predominately due to compositional and/or mineralogical differences.

Recent studies of the reflectance spectra of Apollo 11 lunar samples (Adams, 1970) reveal that four electronic absorption bands are present which arise from ferrous iron and titanium in the clinopyroxenes and olivine. Adams also found that: (1) the laboratory reflectance spectra of fine-grained material from the Apollo 11 landing site are in agreement with the reflectance spectrum of the site telescopically observed by McCord (1969); (2) both rocks and fine particles have clean, unaltered surfaces; thus the reflectance is related directly to the bulk composition of the material rather than to thin coatings, and, (3) the fine particles include large amounts of dark-brown glasses which suppresses the electronic bands and increase absorption of the fine material at shorter wavelengths.

A close relationship between spectral reflectance and composition of the material on the surface of the moon is now strongly established. A telescopic observational study was therefore undertaken to map and classify the spectral reflectance of part of the lunar surface. This chapter deals primarily with the results and implications of that study. The observational technique and method of data analysis summarized below are described in detail in Appendix 1.

INSTRUMENTATION AND OBSERVATION

Lunar observations were made at the Cassegrain focus of the Mount Wilson 24-inch telescope, using a single-beam photoelectric photometer with a high-speed pulse-counting data system. The observations were made by scanning luminance variations across the moon at three wavelengths.

The system response was sufficiently linear over a large brightness range to allow the measurement of small differences in spectral reflectance ($\sim 1\%$) in the presence of large albedo variations of the order of 200%.

Luminance of the lunar surface was measured at wavelengths between 0.4 and 0.7 microns. Below 0.4 microns the atmospheric transmission rapidly decreases; at wavelengths longer than 0.7 microns, the sensitivity of the photomultiplier used and solar illumination decrease. The lower signal levels outside the range 0.4 to 0.7 microns would have required slower scanning in order to maintain the accuracy of the measurement. Slower scanning, in turn, would have reduced the data acquisition,

increased telescope tracking errors, and increased the errors caused by variations in atmospheric transmission.

A survey of normalized relative reflectance spectra of a large number of lunar areas measured by McCord (1968); McCord, Johnson, and Kieffer (1969); and McCord and Johnson (1969) shows that the spectral reflectance curves in the wavelength range 0.4 to 0.7 microns are usually composed of two linear segments joined near 0.52 microns. By taking measurements at 0.4, 0.52, and 0.7 microns, it is possible to distinguish the various spectral types observed. Narrow band ($\Delta\lambda \sim 0.02$ microns) filters were used for the measurements reported here. The data reported accurately represent the true spectral character at the three observed wavelengths, rather than an average over a broad wavelength band, as in the case of UBV photometry.

McCord (1968) has shown that there exist differences in phase angle dependence of lunar spectral reflectance of the order of 2 to 3% between phase angles of 0° and 35° . The variations between phase angles of 35° to 90° are generally of the order of 1%. In this study, observations were taken over a range of phase angle from 30° to 60° . In this way the phase dependent variations between data taken on different nights were minimized.

Measurements were taken by scanning strips 130 arc seconds in length and 18 arc seconds in width (220 by 30 kilometers on the lunar surface near the sub-earth point). Two scans with each of the three filters were taken of each strip. The signal was integrated and recorded at nine

equally spaced intervals while the telescope was moved continuously along the scan. After the six scans were made on each strip, a standard area in Mare Serenitatis (17.6°N , 19.4°E) was measured. This standard measurement was used to remove atmospheric transmission and system throughput functions.

DATA REDUCTION AND COLOR BOUNDARY RECOGNITION

The luminance measured along a scan in one filter depends not only on the relative spectral reflectance, but also on solar illumination, albedo, atmospheric and instrumental effects. Ratioing techniques similar to those used by McCord (1968) were applied to remove these effects; the observed luminance along the scan at each wavelength was divided by the measured luminance of the standard area at the same wavelength. Corrections for differences in albedo and phase angle were then made by dividing the relative luminance of each point along the scan at each wavelength by the relative luminance at one wavelength (0.52μ). After these operations the data are in the form of normalized relative spectral reflectance.

Boundaries between regions of different spectral reflectance which appear in the reduced data are smeared by the finite spatial response of the instrument which depends on the scan rate, integration time, and aperture diameter. Over those parts of a scan along which the relative reflectance is constant, this smearing produces no effect. As the factors which produce the smearing are known, it is possible to calculate the form of a sharp

boundary as it would appear in the reduced data. Lunar color boundaries which can be detected photographically are sharp down to resolutions of 1 or 2 kilometers. For this reason all color boundaries were assumed to be step functions. The output form of a step function model boundary was compared with the reduced scans by autocorrelation in order to locate and identify sharp boundaries. As will be discussed in the following section, variations in the normalized spectral reflectance are usually in the form of a rotation about the 0.52 micron wavelength, that is a change in the overall slope of the curve. Consequently, the autocorrelation functions between the model boundary and the normalized relative reflectance ratios ($0.4\mu/0.52\mu$ and $0.7\mu/0.52\mu$) along a scan should be anticorrelated at color boundaries. This criterion was used as a test of the reality of a color boundary.

CLASSIFICATION OF LUNAR SPECTRAL TYPES

A primary goal of this study was to investigate the variety of lunar reflectance spectra in order to determine whether a variety of discrete spectral types exist or whether the variations over the lunar surface can be characterized by mixtures of a few end members. The reflectance spectra obtained by McCord (1968) suggest that the spectral reflectance characteristics of the lunar surface fall into discrete classes with restricted spectral ranges. As a considerably greater area of the lunar surface was included in the present study, it was possible to test this hypothesis more conclusively

and to accurately identify the spectral types.

The reflectivities of 1107 lunar areas (nine on each scan) were measured at three wavelengths (0.4μ , 0.52μ , and 0.7μ) relative to a standard area in Mare Serenitatis. These relative reflectance values were normalized to the value at 0.52 microns for each area. A correlation diagram was constructed of normalized relative reflectance at 0.4 microns versus that at 0.7 microns in which each lunar area was represented by a point; the bivariate frequency diagram is illustrated with contours in Figure 1. Points for lunar areas located at or near color boundaries were not included in this plot as they would induce artificial mixing. The grid size used in contouring the distribution shown in Figure 1 was 0.005 in the units given on the scale in that figure. The contouring method was tested by comparing contours made with grid sets shifted one-half of a grid cell relative to one another. No significant change in the positions of the maxima was noted.

An examination of Figure 1 indicates that four to eight distinct maxima are present. In order to determine which of the observed maxima may be the result of insufficient statistics and which represent real maxima or spectral types, it was necessary to test the significance of the maxima.

First, the data were divided into two approximately equal parts, each part containing a representative proportion of mare and upland areas. The bivariate frequency distributions for these two sets of data were then contoured (Figure 2) as in Figure 1. Table 1 contains a list of the relative

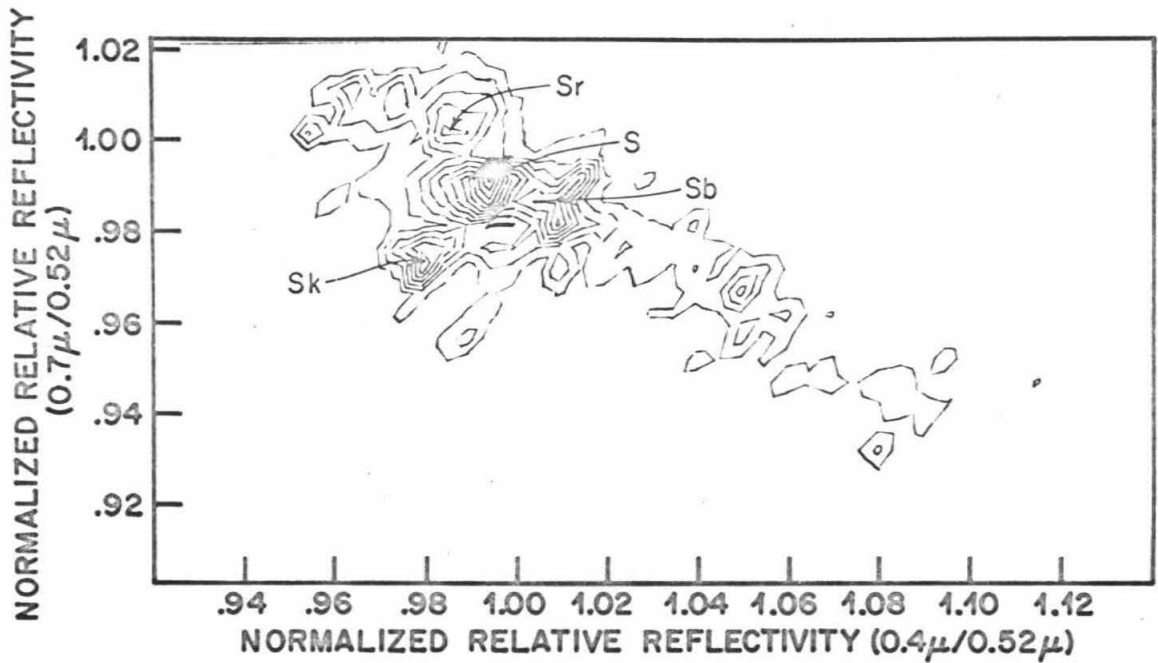


Figure 1. The bivariate frequency distribution of lunar reflectance spectra. Each point was plotted as a point representing its normalized relative reflectance at 0.4μ to 0.7μ . The density of all such points was contoured. The contour interval is 5 points per grid cell (0.005 on each side in units given in the figure).

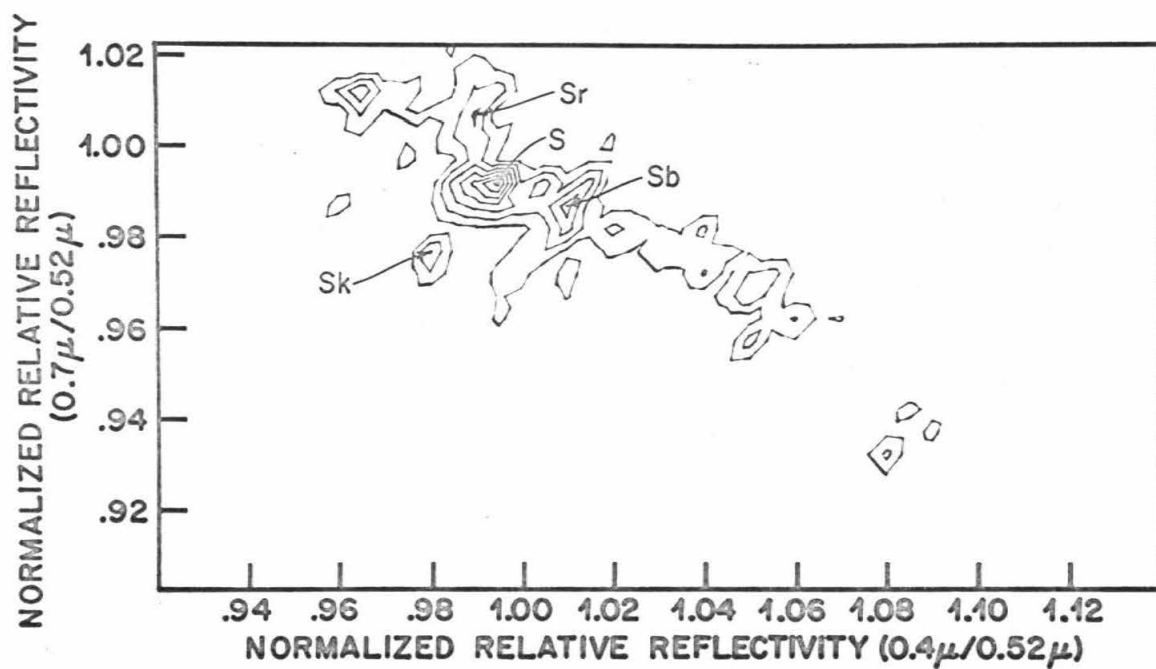


Figure 2a. The bivariate frequency distribution of approximately one-half of the data of Figure 1.

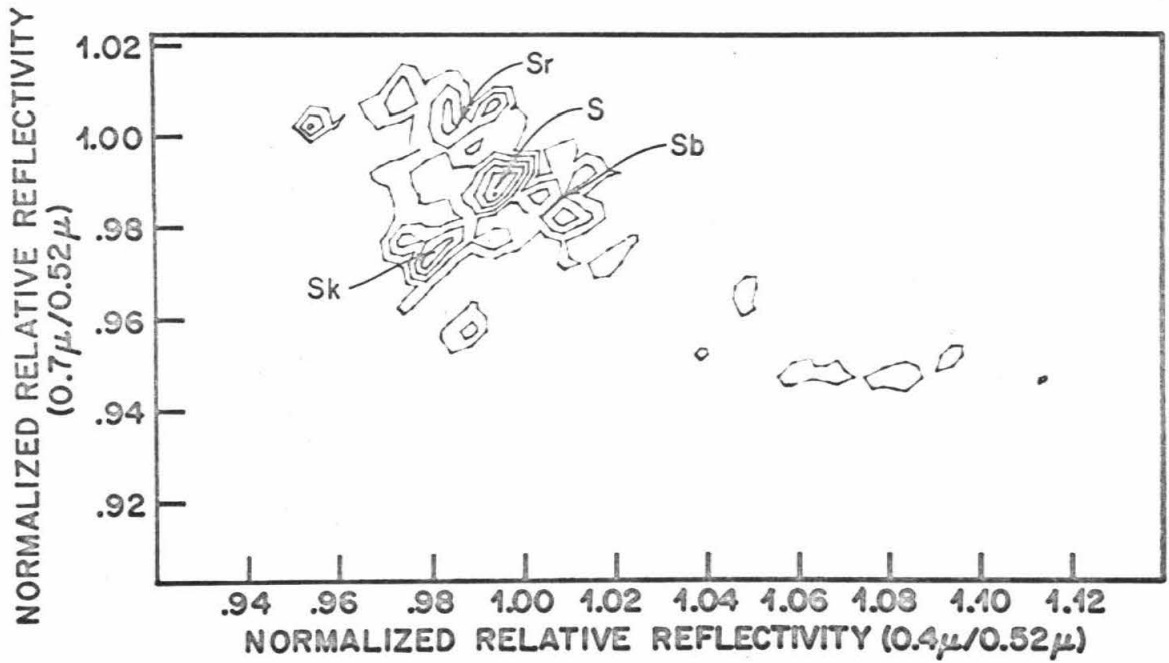


Figure 2b. The bivariate frequency distribution of the second half of the data of Figure 1.

reflectance values of four maxima which can be identified in each of the two contour maps in Figure 2. The agreement in the positions of the maxima demonstrates that the groupings are not produced by insufficient statistics. These maxima are labeled "S" since, as is discussed below, they occur predominantly in Mare Serenitatis and surrounding uplands.

Table 1. Comparison of maxima positions in two data sets.

Spectral Type	Data Set 1 Normalized Relative Reflectance		Data Set 2 Normalized Relative Reflectance	
	$0.4\mu/0.52\mu$	$0.7\mu/0.52\mu$	$0.4\mu/0.52\mu$	$0.7\mu/0.52\mu$
Sb	1.010	0.990	1.010	0.985
S	0.995	0.995	0.995	0.990
Sk	0.980	0.975	0.980	0.975
Sr	0.990	1.005	0.985	1.005

The bivariate distribution shown in Figure 1 was further tested to determine what effects were introduced by variation in lunar phase angle between data taken on different nights. This was accomplished by comparing the normalized relative reflectance values measured along scans taken at different phase angles across a region in which one spectral type predominates. The position of only one type, Sk, was found to vary significantly with phase angle. At phase angles less than about 35° the regions in which this type are found show spectral reflectance values near those

listed for Sk in Table 1. As the phase angle increases, the position of this type migrates toward type S. At phase angles in excess of 50° these types (S and Sk) are indistinguishable. Most of the regions which contain type Sk were found in the lunar uplands east of Mare Serenitatis. Most of the scans of the regions were taken at low phase angles ($<35^\circ$). Hence the appearance of Sk as an isolated maximum in Figure 1 is an observational effect. In the construction of regional maps, discussed in the next section, Sk and S were mapped as one unit to avoid this ambiguity. No major variations with phase angle were found in the positions of the other maxima listed in Table 1.

As is evident from the amplitudes of the maxima in Figure 1, the four spectral types discussed above are the predominant types in the region studied. Other types do exist in the distribution shown in Figure 1, but cannot, on the basis of that figure alone, be distinguished from groupings arising from insufficient statistics, variable phase angle effects, or errors in standard measurements. These less common types which occur in a few small areas can be identified because: (1) the normalized relative reflectance values were reproduced in different scans taken of the same areas on different nights and at different phase angles, (2) the spectral reflectance which typifies each of these groups was correlated between parallel scans within the small regions, and, (3) the spectral reflectances in these regions were in agreement with those found by other studies

such as those of McCord (1968).

Three spectral types in addition to those listed in Table 1 were identified using such criteria. These types, included in Table 2, were found in Mare Tranquillitatis (types T and Tb) and in the vicinity of the crater Proclus (type P). The two Tranquillitatis types are visible in Figure 1 as minor groups. These are well documented in Figures 4f and 4g which show the strong correlation among values measured along different scans of the small regions in which these types occur. Type P was found on the only scan line which traversed the crater Proclus. The spectral reflectance measured in that crater was in agreement with that found by McCord (1968) (see Figure 19, Appendix 1).

COMPILATION OF REGIONAL MAPS

In order to map the distribution of spectral types over the lunar surface, the spectral type of each point along a scan line was identified and labeled according to the regions shown in Figure 3. Table 2 lists the positions and radii of the regions defined for each of the spectral types.

One spectral type is introduced here that was not mentioned in the preceding section. The symbol "Tr" refers to the spectral reflectance type of some light mare units found in Mare Tranquillitatis. From preliminary maps which did not include this type, it was discovered that these lighter regions could not be identified with any of the spectral types discussed in the preceding section. The reflectance spectra of these areas fall into a

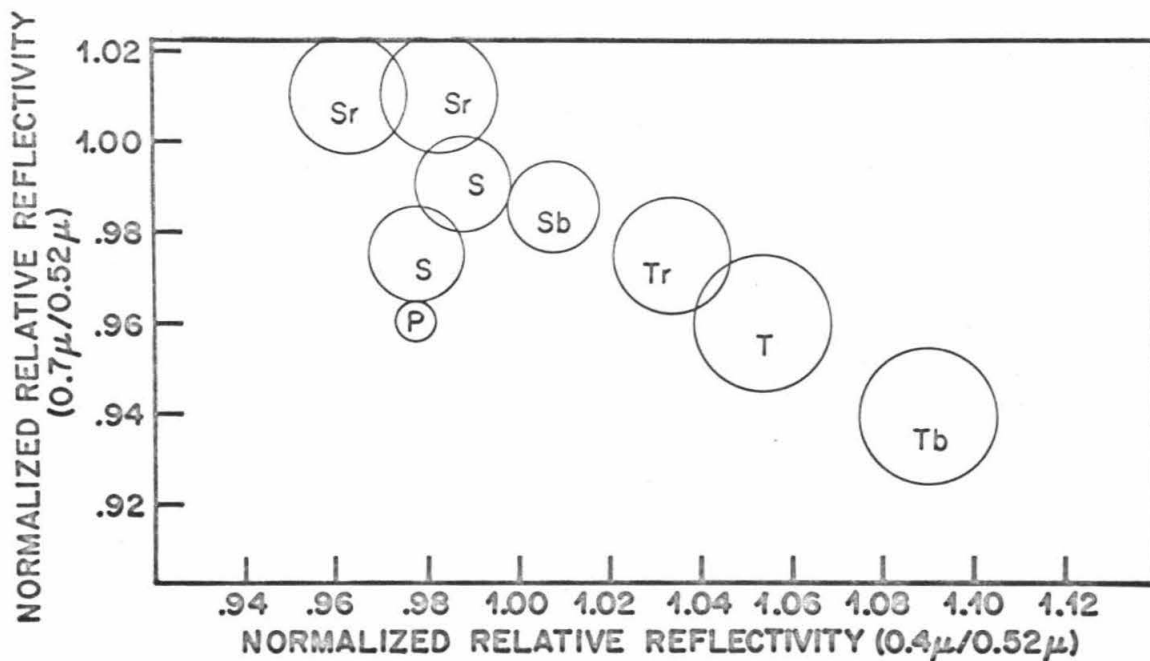


Figure 3. The regions used to classify the reflectance of each point along the lunar scans. Points resting outside of all or within two of the circles were not classified. Points resting inside individual circles were labeled with the corresponding symbols that are shown.

broad region between types Sb and T. Since no concentration or type center is visible there in the bivariate reflectance distribution (Figure 1), Tr may represent some variable mixture of materials.

Table 2. The positions and radii of the regions used to classify the reflectance spectra along scans.

Type	Normalized Relative Reflectance(0.4 μ /0.52 μ)	Normalized Relative Reflectance(0.7 μ /0.52 μ)	Radius of Region
Sr	0.985	1.010	0.0125
Sr	0.965	1.010	0.0125
S	0.990	0.990	0.010
S	0.980	0.975	0.010
Sb	1.010	0.985	0.010
Tr	1.035	0.975	0.0125
T	1.055	0.960	0.015
Tb	1.090	0.940	0.015
P	0.980	0.960	0.005

Scan lines were taken in sets, each set forming a rectangular grid. Figure 4a shows the positions of the thirteen grids in which data were taken. The distortion of individual rectangular sets arose because the observations were made over a large range of lunar geometric libration. Figures 4b through 4h show the distribution of each type along scan lines in the grids.

Figures 5 and 6 show the final stage in the construction of the

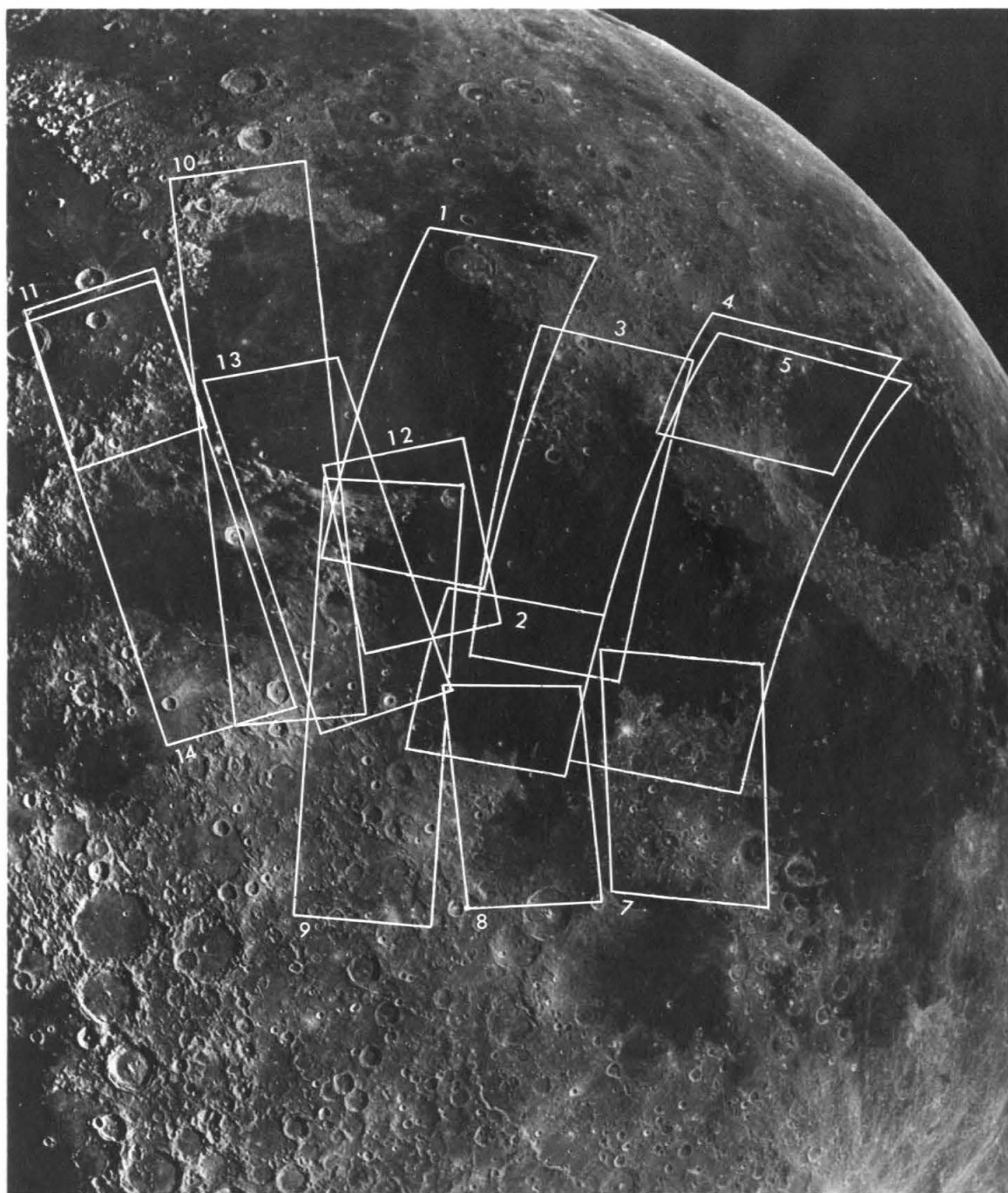


Figure 4a. The position of each of the thirteen scan grids. Each grid contains parallel scan lines separated by 36 arc sec (approximately 60 kilometers). Positions of individual scan lines can be seen in Figures 4b through 4h. Each scan line is approximately 250 kilometers in length.

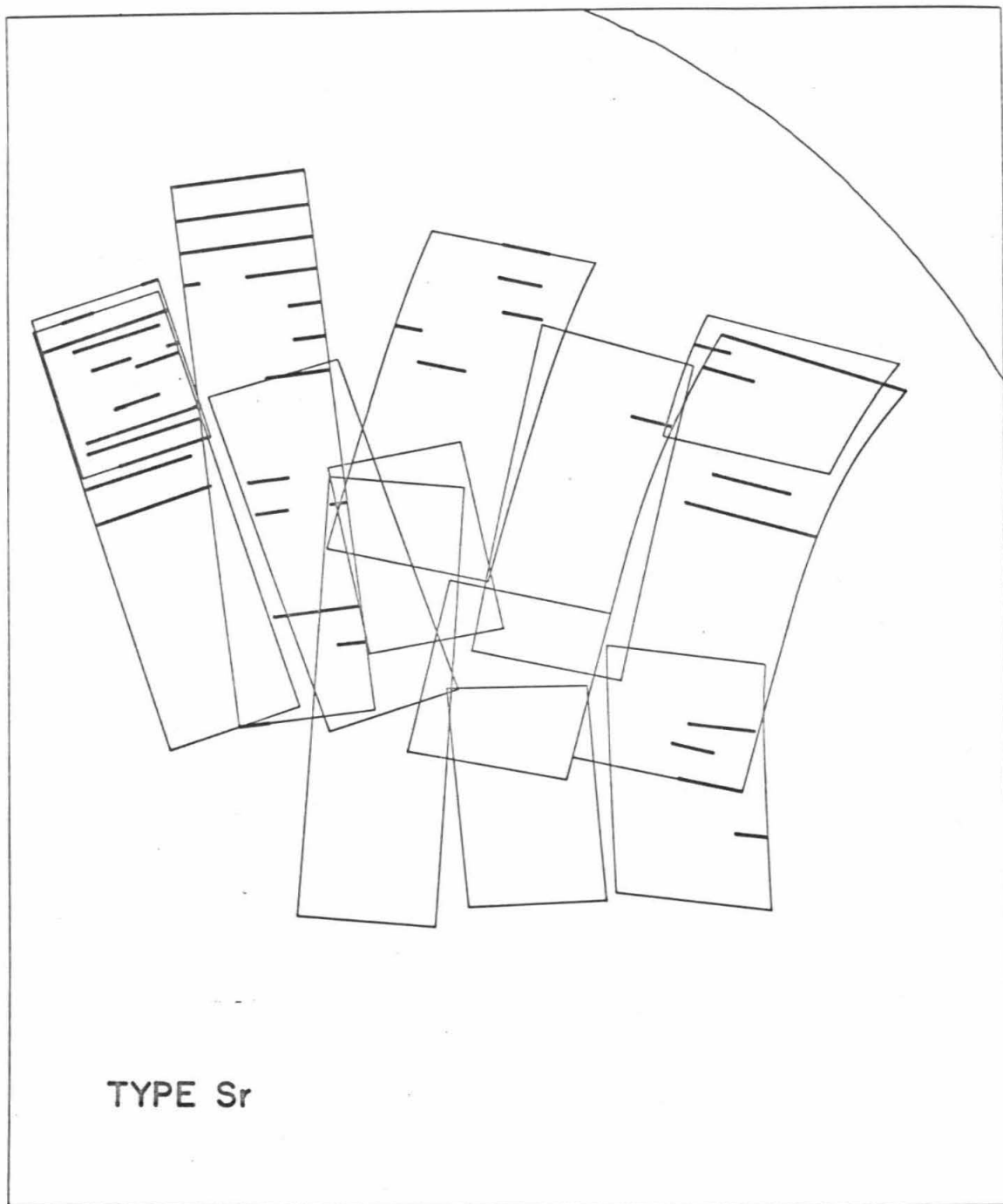


Figure 4b. The distribution of type Sr along individual scan lines.

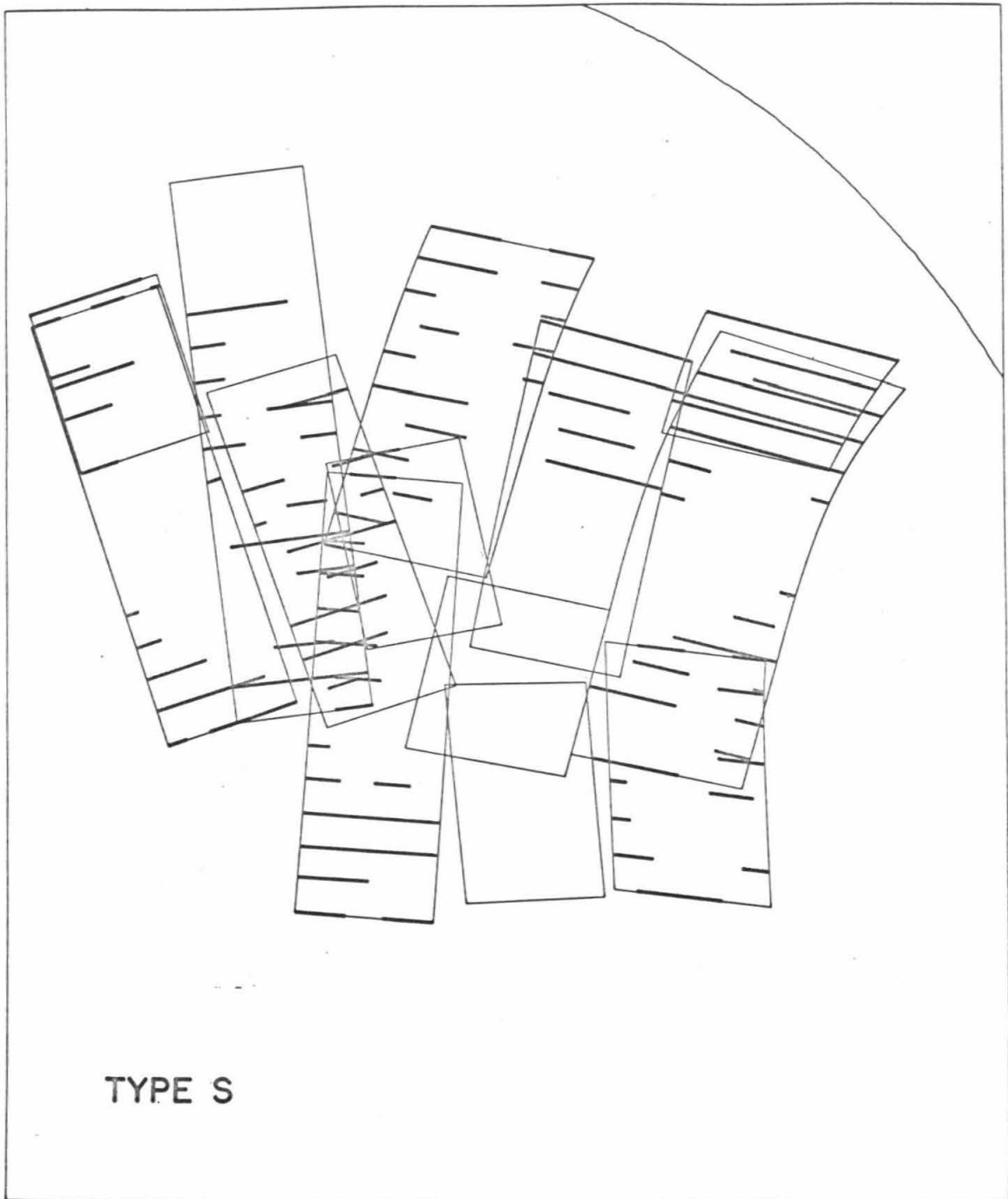


Figure 4c. The distribution of type S along individual scan lines.

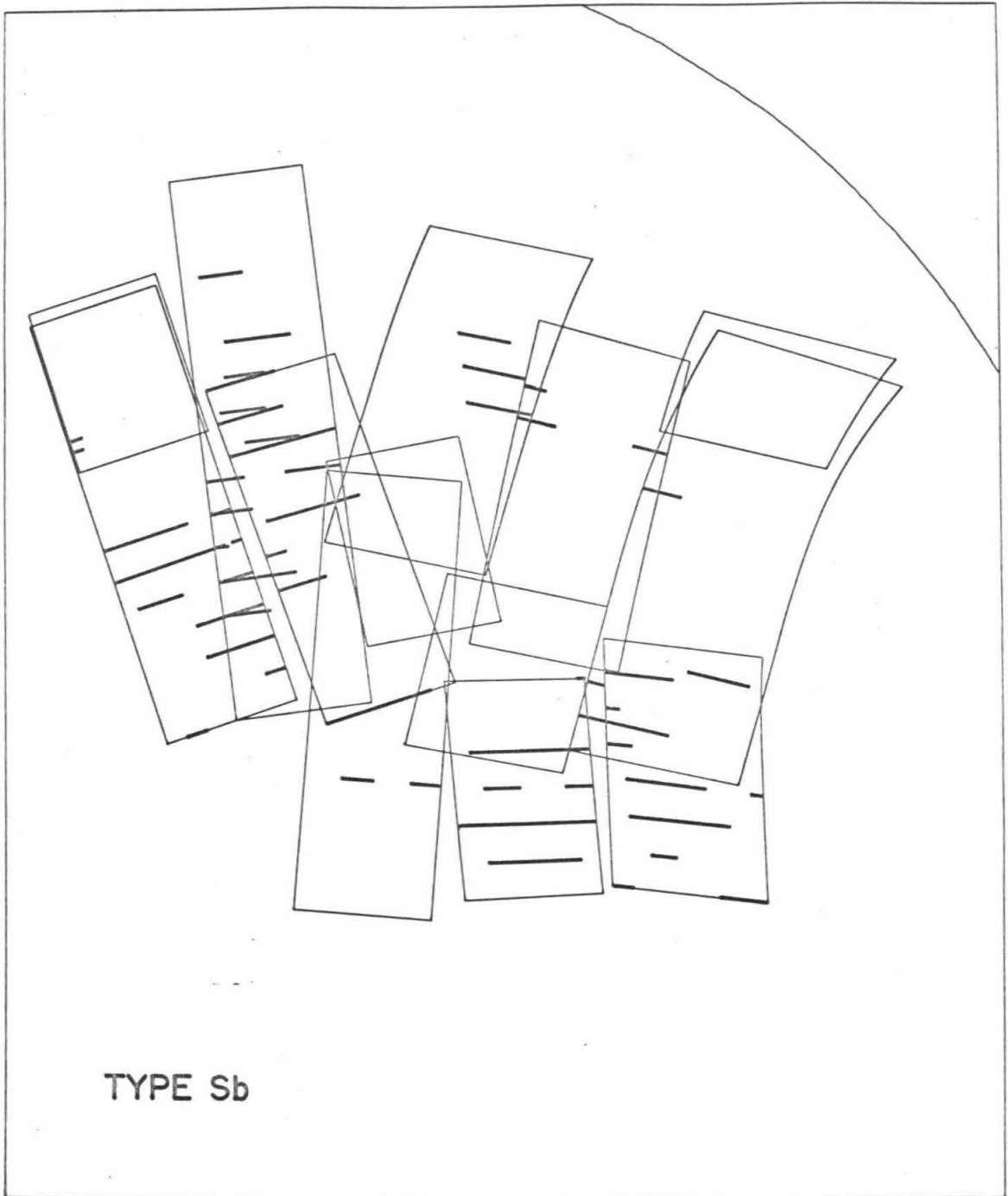


Figure 4d. The distribution of type Sb along individual scan lines.

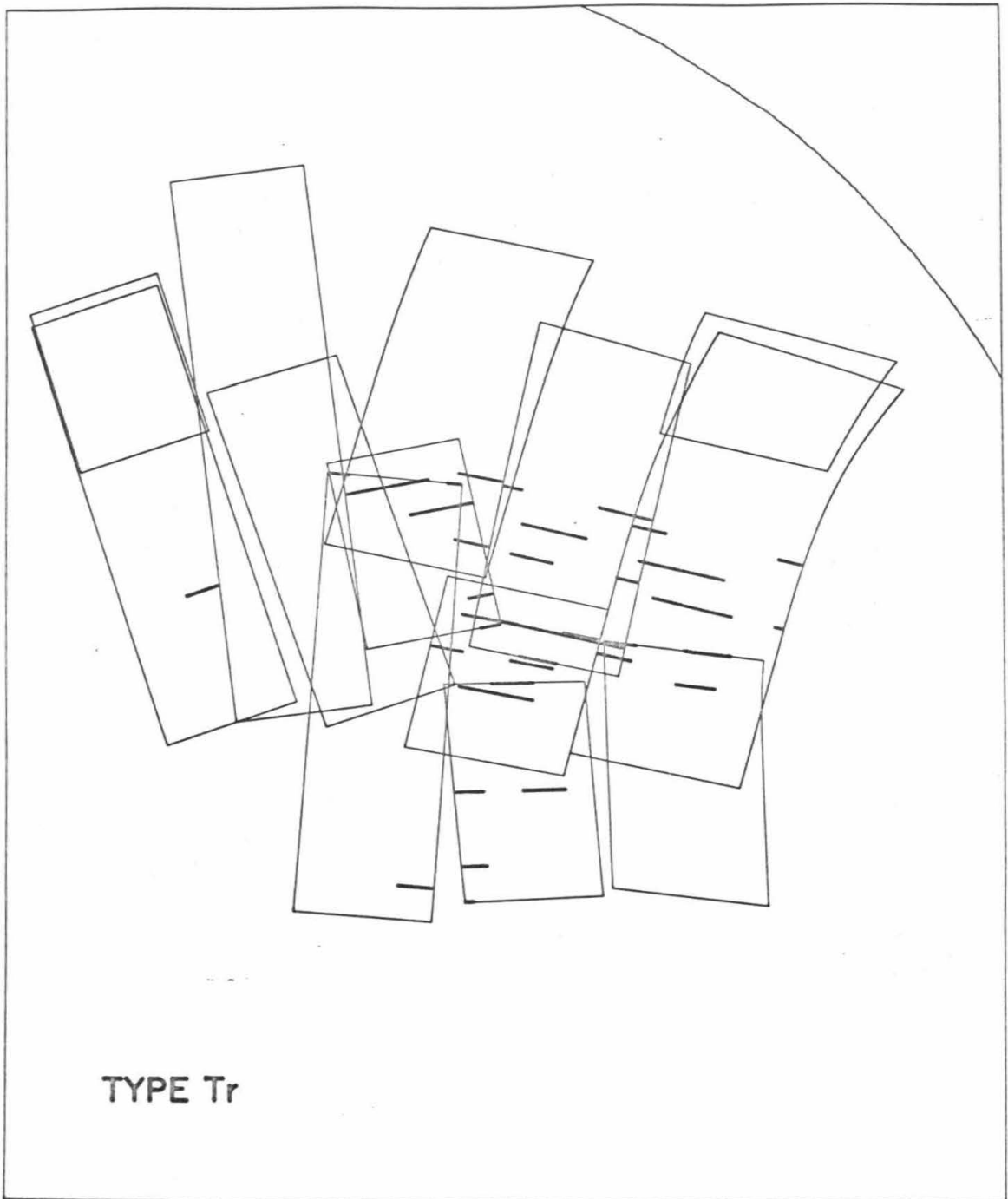


Figure 4e. The distribution of type Tr along individual scan lines.

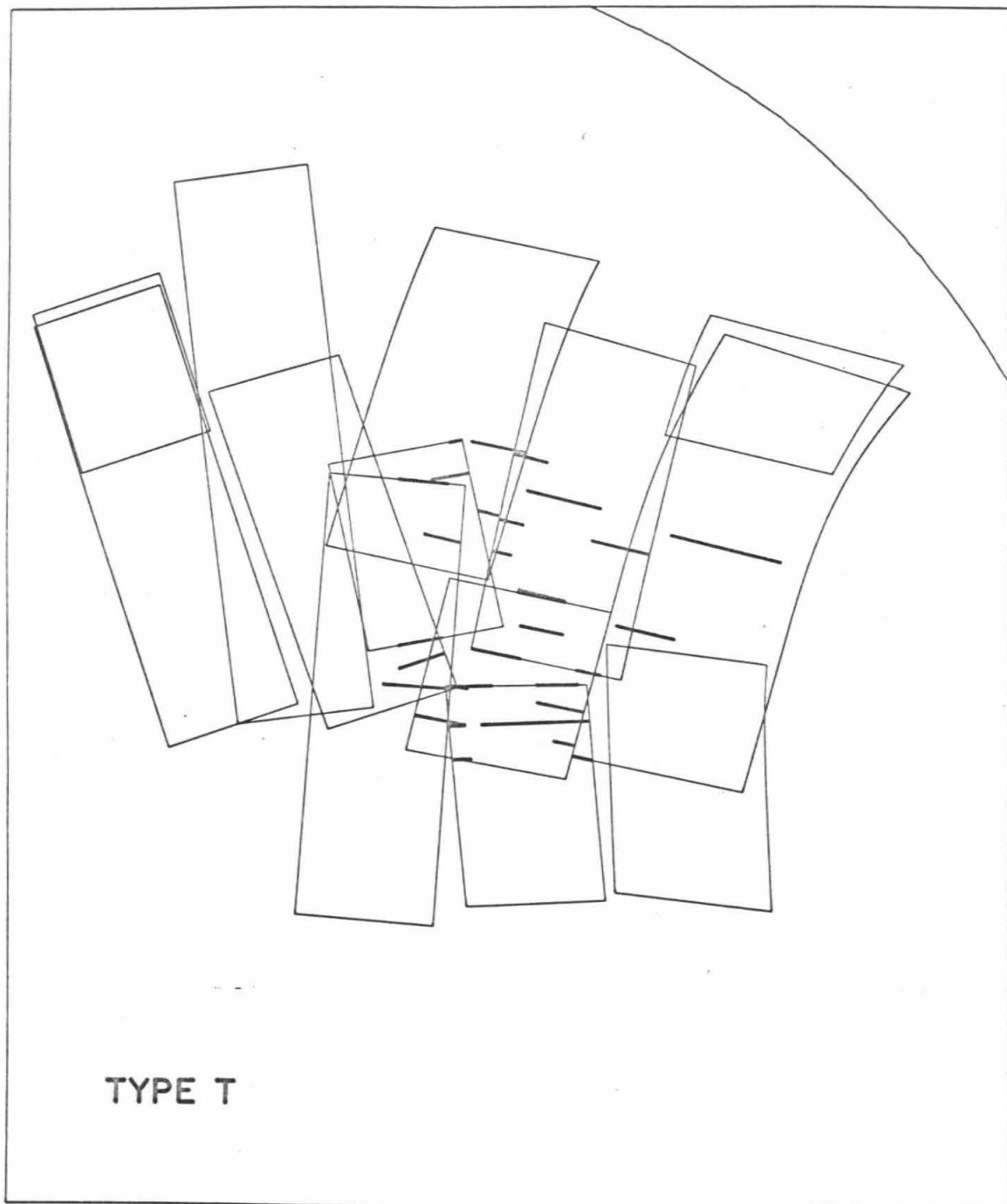


Figure 4f. The distribution of type T along individual scan lines.

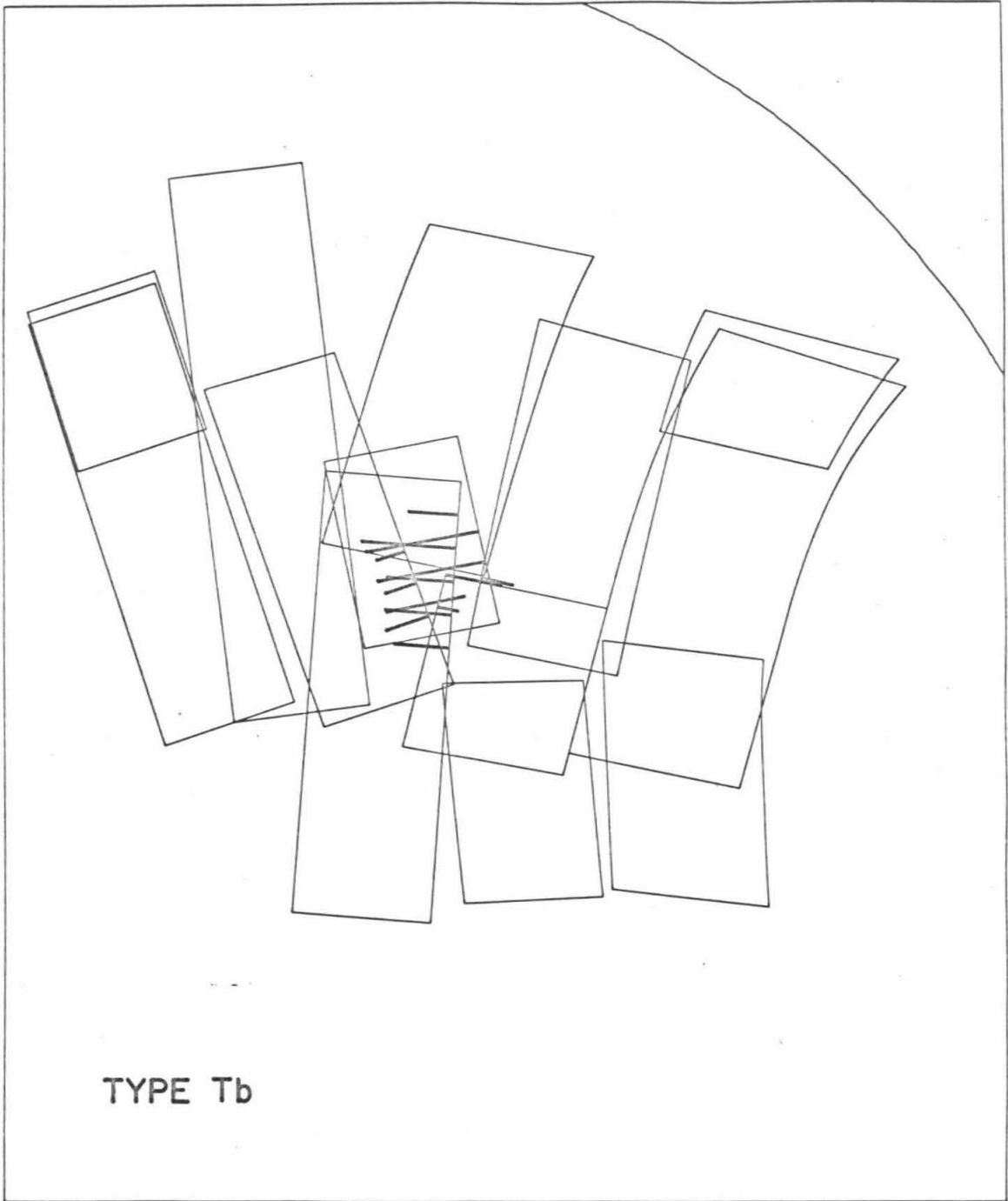


Figure 4g. The distribution of type Tb along individual scan lines.

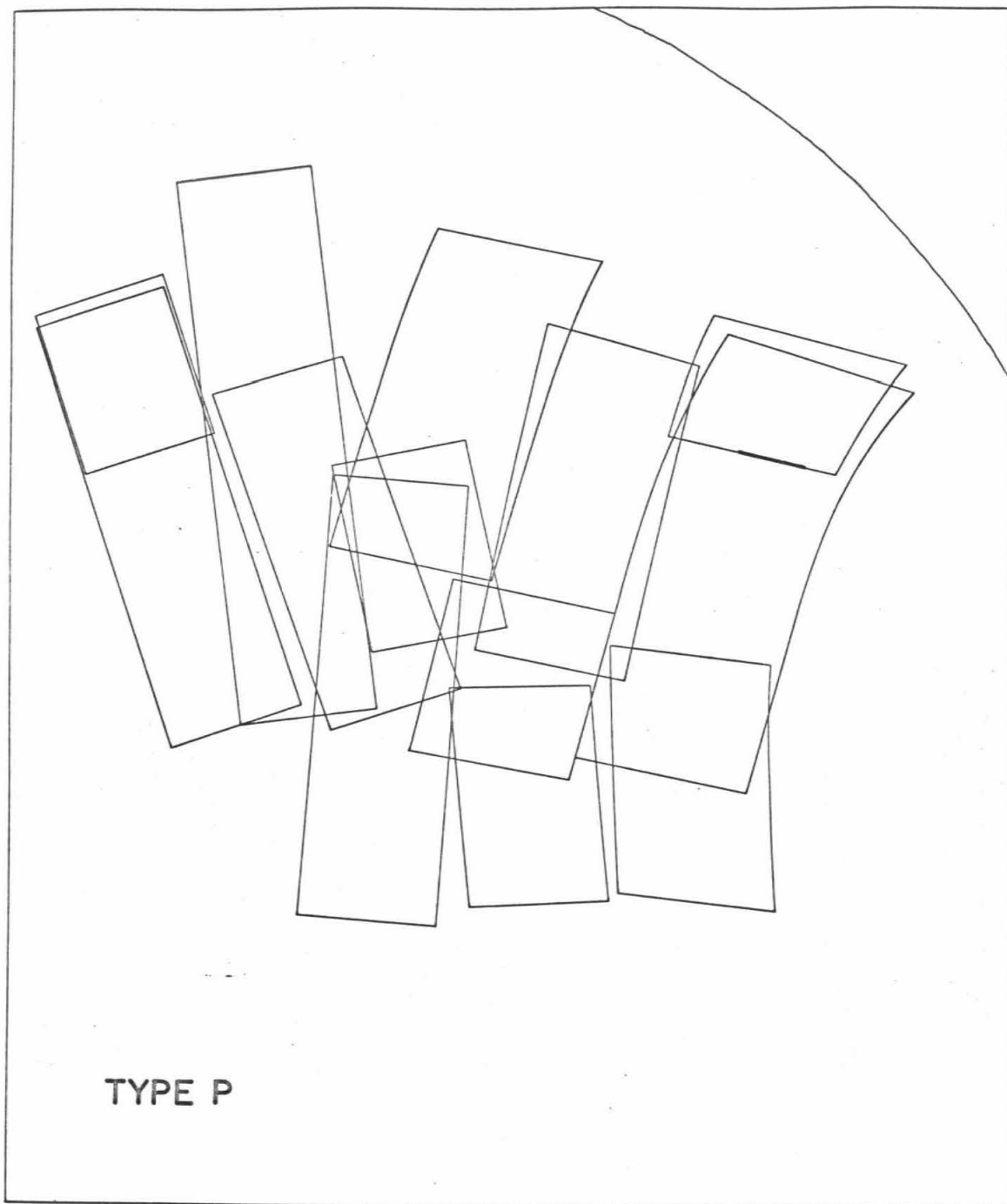


Figure 4h. The distribution of type P along individual scan lines.

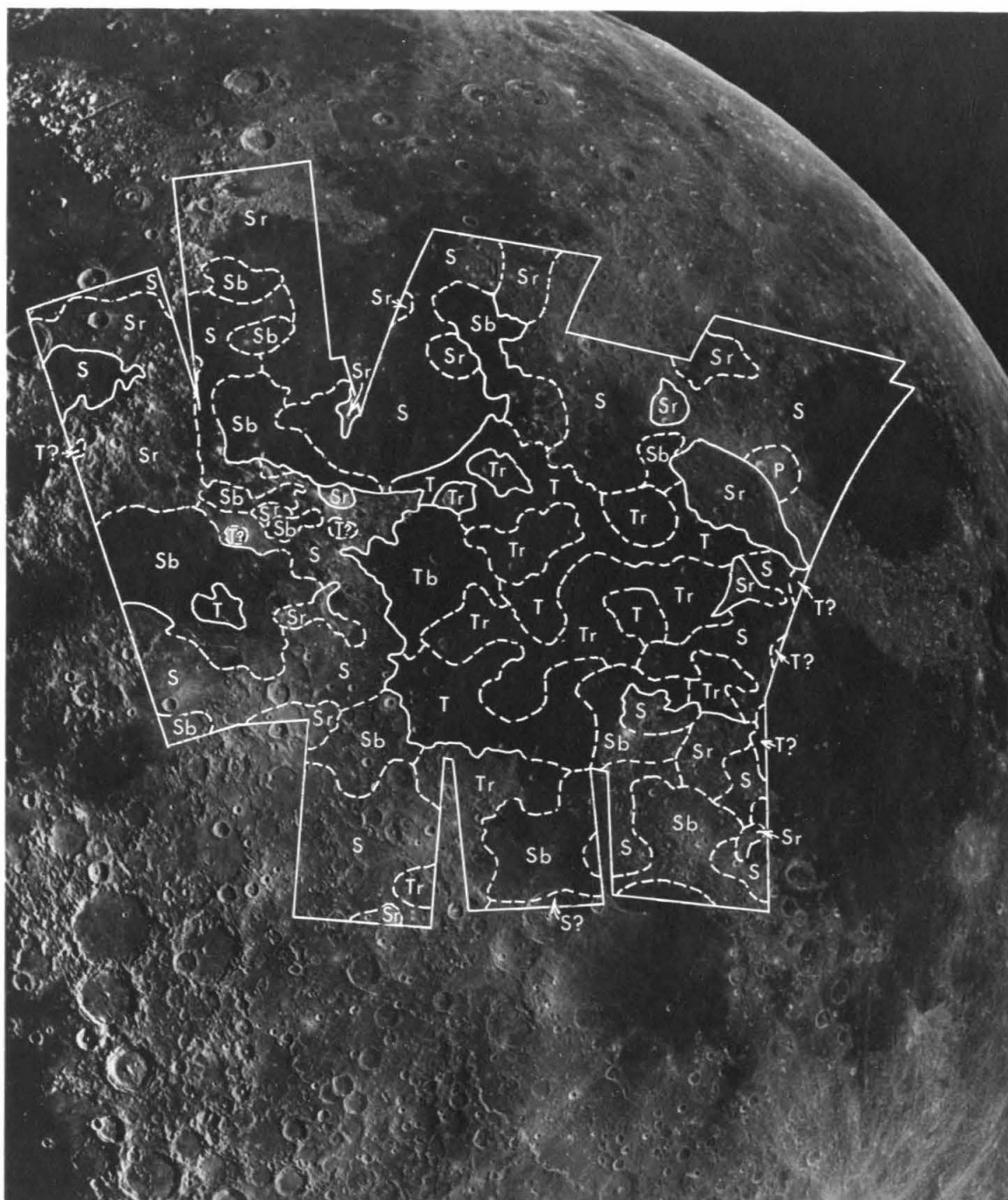


Figure 5. The distribution of the seven spectral types in the Mare Serenitatis and Mare Tranquillitatis regions. Solid lines are drawn where color boundaries coincide with sharp albedo boundaries. Dashed lines are drawn where color boundaries and albedo boundaries are not definitely correlated.



Figure 6. The distribution of the seven spectral types in the Mare Serenitatis and Mare Tranquillitatis regions. Boundaries are the same as in Figure 5.

regional map. The data of Figure 4 were transferred to a lunar photograph using tracking photographs taken during the observations. Solid lines were drawn along marked albedo boundaries coinciding with sharp color boundaries, under the assumption that some correlation exists. Hence the detail drawn along such boundaries is somewhat interpretive. Dashed boundaries were drawn at color boundaries which (1) appear as gradational boundaries, (2) coincide with diffuse albedo boundaries, (3) coincide with no visible albedo variation, or, (4) whose position is questionable.

DISCUSSION OF RESULTS

The map of spectral types shown in Figures 5 and 6 demonstrates the regional associations of each spectral type with particular morphologies and structures.

As is evident from Figures 1 and 6, the four Serenitatis spectral types are the most common in the region studied. All four of these types are found in uplands and in the three ring maria: Mare Crisium, Mare Nectaris, and Mare Serenitatis. The structure and morphology of these ring maria can be characterized by (1) large positive free-air gravity anomalies, (2) circular basins with associated concentric fault patterns, and, (3) thick deposits of mare material which appear to become thicker toward basin centers. The spectral types Tb, T, and Tr were found almost exclusively in Mare Tranquillitatis and Mare Fecunditatis. These maria are distinguished by (1) the lack of any positive gravity anomalies,

(2) irregular shapes which are not related to any circular structures or other apparent subsurface structure, (3) thin veneers of mare material through which pre-existing topography often protrudes, and, (4) a generally greater areal extent than the ring maria.

A variety of spectral types exists in the lunar uplands. Hence these regions are not homogeneous, as is commonly thought, but display considerable heterogeneity.

As can be seen in Figures 5 and 6, some mare-uplands boundaries, such as the boundary of Mare Crisium on the north and west, are not accompanied by detectable color variations. Further, color boundaries that exist within the upland terrains often exhibit no albedo variation. Color boundaries in the maria are, however, almost always accompanied by detectable albedo boundaries.

COMPARISON WITH PREVIOUS STUDIES

A comparison of the results of this research with those obtained by Whitaker (Kuiper, 1965) in a photographic study of lunar color indicates that Whitaker's photographic results contain numerous pseudo-color effects induced by large albedo variations. Since the dynamic response of the film was not linear over the large range of brightness, upland-mare boundaries show large artificial color differences. For example, Whitaker's photographs show that the uplands are generally red compared to the

materials in Mare Serenitatis. As can be seen from Figures 6 and 7, both the uplands and Mare Serenitatis contain materials with S-type spectral reflectances. If care is taken to compare only areas of similar albedo, however, such photographic studies can be used to extend the results of this program to other areas of the lunar surface.

The conclusion in this study that types Tr, T and Tb are associated with thin irregular maria based on the investigation of only one such region (Mare Tranquillitatis and western Mare Fecunditatis). This conclusion is strengthened by the photographic results of Whitaker (Kuiper, 1965) which suggest that Oceanus Procellarum, which is similar to Mare Tranquillitatis in all morphological and structural characteristics, also has the same spectral properties. Results of McCord, Johnson, and Kieffer (1969) have confirmed this suggestion. Their results show that Orbiter sites 11 P 13 and 111 P 11, which are in southern Oceanus Procellarum, are of spectral type T.

A further comparison with Whitaker's composite color difference photographs indicate that Mare Imbrium and Mare Humorum which have morphologies similar to Mare Serenitatis contain materials with spectral reflectances similar to those found in Mare Serenitatis. The southern portion of Mare Imbrium is covered by a thin T type maria which does not support the correlation between ring maria and S-type reflectances. As will be discussed in Chapter IV, however, this material is probably a northern extension of the T-type mare formation in Oceanus Procellarum.

SUMMARY AND CONCLUSIONS

The results presented in this chapter confirm the suggestions of McCord (1968) and McCord and Johnson (1969) that several distinct spectral types are present. Further, the results demonstrate that a variety of distinct kinds of material exist in both the uplands and in individual maria. The spectral type, Tr, may, however, represent some variable mixture of materials in Mare Tranquillitatis.

Seven distinct spectral types were found in this study. It is quite possible that this number could be substantially increased through the use of observational techniques with increased sensitivity, the inclusion of studies at other wavelengths, and the investigation of other regions.

The observation that albedo and color boundaries are not always coincident suggests that the physical and chemical properties of the surface that affect albedo and spectral reflectance are different. It should be stressed that differences in spectral reflectance do likely indicate differences in composition. It is not valid to conclude, however, that similarities in spectral reflectance necessarily indicate similar composition since the reflectance spectrum may be affected by only a small percentage of the minerals present.

The most important conclusion that can be made on the basis of these data is that there is a correlation between the morphology and composition of a lunar mare. The observations show that: (1) the circular

maria which have positive gravity anomalies and thick mare deposits (Mare Serenitatis, Mare Crisium, Mare Nectaris, Mare Imbrium, and Mare Humorum) contain materials which have S-type spectral reflectances (S_r , S , and S_b), and, (2) the thinner, larger, irregular maria which are not associated with regional structure or gravity anomalies (Mare Tranquillitatis, Mare Fecunditatis, and Oceanus Procellarum) contain T-type units (T_r , T , and T_b). The correlation between morphology and spectral type suggests that the two types of maria may be genetically different.

III. DETERMINATION OF RELATIVE AGE FROM CRATER MORPHOLOGY

INTRODUCTION

The morphology of the lunar surface has been produced both by internal processes, such as vulcanism, and by external processes, such as impact of meteoroids and comets. The relative importance of these processes in the formation and modification of lunar craters is explained in this chapter. Craters with diameters less than a few hundred meters vary in form from shallow, irregular depressions to sharp, circular craters with raised rims and blocky ejecta blankets. The approach taken here is to model the processes of crater production by impact and erosion due to bombardment by small particles and to compare the expected morphologies and size-frequency distributions of craters with those measured from lunar photographs.

The results of the model study show that erosion by impacting small bodies, which individually produce only minor changes in the shape of a crater being eroded, is the most important process by which the shape of craters of diameter less than 1 kilometer is changed. Thus the shape of a crater is a very sensitive indicator of the total number of small impacts that have occurred since the crater was formed. This measurement of total accumulated small impacts can be viewed as a relative age. By determining the relative age of the oldest crater on a given surface it is possible to date the formation of the surface in terms of the integrated flux of impacting particles. The time scale to which this age refers does not represent absolute but is distorted by the historical variations in the impact flux. Dating techniques based on these concepts were developed and applied to lunar photographs. The relative ages obtained from observations of

crater shape were then compared with the preliminary age determinations obtained for Apollo 11 and 12 samples in order to derive approximate absolute ages for the formation of various regional lithological units.

It is appropriate first to briefly review the general distribution of lunar craters and the present state of understanding of these distributions. Photographic surveys of the lunar surface by Ranger, Orbiter, and Surveyor imaging missions have provided information on the distribution of lunar craters down to diameters of a few centimeters. The general forms of these distributions are very similar for different regions. For crater diameters greater than about 3 kilometers, the areal density of craters can be represented by a function of the form

$$(1) \quad N = k D^{-1.7}$$

where N is the number of craters per unit area with diameters greater than D and k is a constant. Craters in this size range are generally thought to be of impact origin because of their characteristic morphologies, associated rays, and secondary craters. Between diameters of about 100 meters and 1 kilometer, the distributions can be approximated by the power function

$$(2) \quad N = k' D^{-3.0}$$

where k' is a constant. Theory predicts and observation confirms that craters in this size range are created mostly by secondary impact of fragments from craters larger than a few kilometers in diameter whose distribution is represented by equation (1). The constants k and k' vary from region to region. The size-frequency distributions for craters smaller than about 100 meters, however, are represented by a third equation which is the same for all mare localities.

The constancy of the distribution of craters of diameter less than 100 meters was first demonstrated by Trask (1965) who found the distribution in this size range to be

$$(3) \quad N_{ss} = 10^{10.9} D^{-2.0}$$

where N_{ss} is the number of craters per 10^6 square kilometers with diameters greater than D in meters. Recent surveys by Shoemaker, et. al. (1969) have confirmed that equation (3) characterizes the distributions at all Surveyor landing sites down to diameters of at least 10 centimeters. The constancy of the distribution of craters smaller than about 100 meters has led many observers to conclude that craters in this size range form a steady state population in which craters disappear at the same rate at which they are formed. The purpose of the discussion which follows is to explore the mechanism by which these craters disappear.

IMPACT EROSION MODEL

The modification of a lunar crater may be caused by a variety of processes including (1) slumping or creep of material down the crater walls, (2) impact erosion by particles which individually produce negligible changes in the form of the crater, (3) impact of bodies, each of which produces major changes in the overall shape of the crater, (4) blanketing or flooding of the crater by thin deposits of fluid or fluidized material, (5) blanketing of the crater by ejecta from distant large impacts, or, (6) internal processes of surface readjustment such as settling or collapse.

Observational evidence indicates that the most important process acting on small craters (diameters less than about 1 kilometer) is continuous erosion

by impacting bodies which produce individual effects that are small compared to the craters being eroded. Overlap by craters of comparable size does not appear to be an important process of crater modification as the number of recognizable overlapping craters is only a few percent of the total number of craters. Blanketing by ejecta from distant craters is not a large effect as only a small fraction of material ejected from a given crater is thrown farther than a few crater radii.

The process of erosion considered here is the downslope transport of material ejected from small craters. The formulation of the erosion model is briefly outlined here; a detailed discussion is available in Appendix II.

Experimental studies of hypervelocity impact (Gault, et. al., 1963) have shown that material is ejected from the perimeter of an expanding cavity into a conical sheet whose axis is approximately normal to the initial surface. The form of this conical spray of ejecta is nearly independent of the slope of the surface or angle of incidence of the impacting projectile. The thickness of the ejecta blanket of a crater formed on a level surface, as a function of distance from the center of the crater, is known from experiment. It is possible to estimate the form of the ejecta distribution had the crater been formed on a sloping surface. Such calculations show that the downslope displacement of the center of mass of the ejected material is given by

$$(4) \quad W = C R \tan \varphi$$

where W is displacement of the center of mass, R is the radius of the crater, φ is the slope of the surface, and C is a constant near one. It has been assumed that the slope of the surface does not vary significantly over distances of the order of R or W . This assumption is valid so long as the dimensions of the

eroding craters are small compared to the crater being eroded.

Studies of the observed size-frequency distribution of fresh craters with diameters between about 100 meters and 1 kilometer indicate that most of these craters are produced by impact of secondary fragments ejected from larger craters. It is reasonable to assume that the theoretical extension of this distribution to smaller sizes (down to diameters of centimeters) represents the production function for the smaller craters. Such a production function has the form

$$(5) \quad n = A R^{-\lambda}$$

where n is the number of craters formed per unit area per unit time with radii greater than R ; λ is the observed exponent of the size-frequency distribution of craters in the size range between 100 meters and 1 kilometer; and A is an unknown constant that depends on the rate of formation of primary craters.

From equations (4) and (5) it is possible to derive an expression for the rate of change of shape of a relatively large crater by impacts producing small craters of radii between 0 and some maximum radius, R_{\max} . R_{\max} is the upper limit of the distribution of eroding craters whose effects can be meaningfully averaged over the surface. Craters larger than R_{\max} produce catastrophic, isolated effects. R_{\max} increases with time as larger craters become more abundant and can be averaged into the distribution which has uniformly blanketed the surface. A stringent constraint on such an erosion model is that R_{\max} remain small by comparison to the relatively large crater being eroded. The differential equation which governs the time evolution of the surface topography is

$$(6) \quad K \nabla^2 h = \partial h / \partial t$$

and

$$(7) \quad K = c R_{\max}^{4-\lambda}$$

where h , the topographic elevation above some datum, is a function of horizontal coordinates and time; c is an unknown constant dependent on various scaling parameters. The explicit time dependence of R_{\max} is not included in equations (6) and (7). This must be determined after integration of equation (6) as K represents the average rate of erosion for the time interval between $t=0$ and some time at which the solutions are evaluated.

Equation (6) was solved for the erosion of a lunar crater formed on a flat, level surface. For convenience the initial form of the crater was approximated by

$$(8) \quad h(r,0) = \frac{H}{1.4} \left\{ 1 - J_0(\alpha_1 r/a) \right\}$$

where r is the radial coordinate, a is the crater radius, J_0 is the first harmonic of the spatial dependence of the solution of equation (6) written in cylindrical coordinates, α_1 is the root of $J_1(\alpha_1) = 0$, and H is the rim height above the crater floor. This form (Figure 23, Appendix II) was chosen because first, it reasonably describes the form of fresh lunar craters and, second, it is the longest lived harmonic in the solution of equation (6). The choice of this initial form contains the implicit assumption that the radius of the crater rim does not change as a function of time although during the erosion of real craters the radius does change slightly with time. From equations (6), (7), and (8) the evolution of crater form as a function of time is given by

$$(9) \quad h(r,t) = h(r,0) \exp(-\alpha_1^2 K t/a^2)$$

The explicit time dependence of K has not been included in equation (9). This dependence is determined by requiring the total integrated area of all craters larger than R_{\max} to be equal to twice the total surface area. By applying this definition of R_{\max} , equation (9) can be reduced to the form

$$(10) \quad t = B \ln^{1/2}(S_i/S) a^{\lambda-2}$$

where S_i is the maximum initial slope of the crater wall; S is the maximum slope at some time, t ; and B is a constant dependent on the rate of formation of small craters. The ratio R_{\max}/a was calculated as a function of S and found to remain less than about 0.3 for $S > \tan 10^\circ$. This value appears to be somewhat large, but as discussed below, other processes such as slumping inside the eroding craters would increase the erosion rate and substantially decrease this ratio. The rate of change of the general form of a lunar crater is dependent on two different effects: (1) the erosion rate increases as R_{\max} increases, and, (2) the erosion rate decreases as the crater slope decreases. The evolution of crater shape with time is shown in Figure 23 of Appendix II.

The lifetime, τ , of a crater is

$$(11) \quad \tau = B \ln^{1/2}(S_i/S_f) a^{\lambda-2}$$

where S_f is the lower limit of slope for crater recognizability. As λ is approximately 3, equation (11) states that the average period of time which a crater can last on the lunar surface is proportional to its radius. A result similar to this was obtained by Ross (1968) from a computerized erosion model.

Combining equation (11) for the lifetime of lunar craters and equation (5) for the rate of production of these craters, the following steady state

distribution can be derived

$$(12) \quad N_{ss} = C'(\lambda) D^{-2}$$

where N_{ss} is the cumulative number of craters whose diameters are greater than D . The exponent of the steady state distribution is -2 and is independent of A and λ of the production function (equation (5)); C' is a constant that is dependent on the exponent of the production function, the initial slope, the lower limit of slope for crater recognizability, and scaling parameters relating crater radius to mass ejected. For the appropriate ranges of these parameters equation (12) yields

$$(13) \quad N_{ss} = 10^{11.2 \pm 0.2} D^{-2}$$

which compares favorably with the observed steady state size-frequency distribution of craters (equation (3)). The small difference between the constants in equations (3) and (13) does not indicate the presence of other erosion processes, as only one effect of the eroding craters was modeled. Another effect, not considered in the model, is mass-transport by slumping in the eroding craters. The effectiveness of this transport mechanism will also depend approximately on the crater radius and the tangent of the slope of the surface. Thus such slumping would not seriously modify the form of the resulting size-frequency distributions but would increase the erosion rate and would decrease the constant in equation (13) bringing it into closer agreement with that in equation (3).

It has been assumed throughout the discussion of the impact erosion model that the flux of impacting particles has remained constant with time. Although this assumption is probably not valid over the entire span of lunar history, particularly in the very early history, the results of the erosion model are still

valid if the concept of time is replaced by that of the integrated flux. As is discussed in the sections which follow, evidence suggests that the flux of bodies forming craters in the smaller size range (diameter < 1 kilometer) has been nearly constant over at least the last 3 and 1/2 billion years.

It was also assumed in the development of the model that the form and exponent of the production curve has not varied with time. This assumption is probably valid for the maria because (1) the observed crater distributions for various maria of craters with diameters above the steady state limit differ by factors of two or three in total abundance but have the same exponential dependence on crater diameter, and, (2) the exponent of the crater production curve is related primarily to the distribution of secondaries of individual large craters.

In summary, the model predicts both the constant and the exponent of the power function which approximates the observed size-frequency distribution of craters in steady state and provides an explanation of the observed distribution of crater forms. The direct comparison of the erosion model with the observed slope-frequency distributions of crater walls is included in the next section.

METHOD OF DETERMINATION OF RELATIVE AGE

The erosion model which has been described can be used to estimate from Orbiter photographs relative age from the integrated flux on various lunar surfaces. A detailed description and validation of the dating technique is provided in Appendix III.

The advantage in determining accumulated flux from crater morphology, rather than by simply counting craters, lies in the fact that the shape of a crater is a sensitive indicator of the integrated flux of a large number of small particles. Uncertainties in the size-frequency distributions of lunar craters larger than the

steady state limit arise from clustering of secondary craters and variations in the distributions of primary craters. Thus a large number of craters must be counted in order to gain useful statistical precision. The integrated flux of small particles, however, can be quite accurately obtained from an examination of the shape of only a few large craters.

Because of large errors in photometric calibration of the Orbiter imaging system, it is not possible to obtain accurate slope-frequency distributions of crater walls through the use of standard photoclinometric techniques. It is possible, however, to obtain directly certain kinds of information which are closely related to these distributions. The dating technique is based on a measurement of the ratio of the number of craters with slopes less than some slope, S_s , to the number with slopes greater than S_s as a function of crater diameter. In practice the slope S_s is the elevation angle of the sun. The ratio, P , of the number of unshadowed to shadowed craters is measured as a function of crater diameter, D ; this relation and its variation with S_s are predictable from the erosion model. Craters larger than some diameter, D_s , are all shadowed as the total accumulated flux on the surface is less than that required to erode them to slopes less than S_s . D_s is the diameter of a crater whose wall would be eroded to a slope of S_s in the time elapsed since the surface was formed. Between D_s and C_s , the diameter of the largest crater in the steady state distribution, P has the predicted form

$$(14) \quad P = \frac{D}{D_s} - 1$$

and below C_s , P has the form

$$(15) \quad P = \frac{D_s}{C_s} - 1$$

This form shown in Figure 7 is an idealization, as the observed C_s varies in a complicated way as a function of sun elevation angle and photograph quality. C_s is a function of the lower limit of slope for crater recognizability, which, in turn, is a function of S_s and the photographic contrast. In this discussion the exact form of the function P near and below C_s is not of particular interest. A detailed explanation and examination of the observed variations is available in Appendix III. Figure 8 shows the observed form of the P versus D relation measured for one lunar area with Orbiter pictures taken at different sun elevation angles. The shaded areas denote the range of acceptable fit of the theoretical model to the data. Hence the erosion model predicts both the observed slope-frequency and size-frequency distributions of craters.

The observed form of the P versus D relation is affected by variations in the size-frequency distributions due to swarms of secondary craters and random variations in the distribution of primary craters. One feature of the observed form of the relation, however, which is not affected by these random variations is the diameter of the largest unshadowed crater, D_s .

Relative ages are presented in the form of the diameter, D_L , of a crater the walls of which would be eroded to some arbitrarily small slope, S_f , in time equal to the age of the surface. D_L is given by

$$(16) \quad D_L = \frac{\ln^{1/2}(S_i/S_s)}{\ln^{1/2}(S_i/S_f)} D_s$$

D_L differs from C_s in that its value does not vary as a function of illumination angle and photograph quality. This is an important feature of the dating technique as the results are independent of illumination angle.

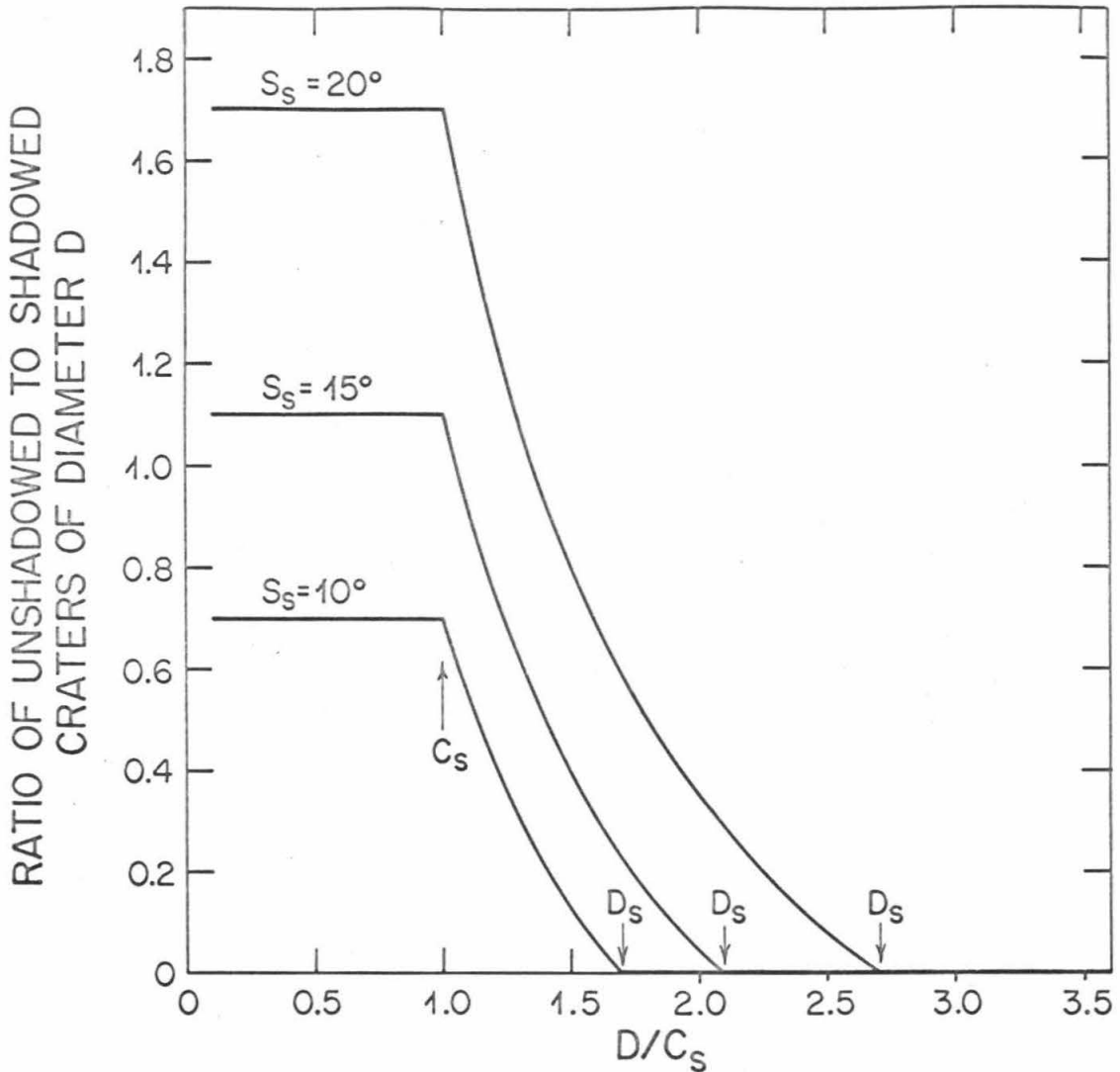


Figure 7. The ratio of unshadowed to shadowed craters as a function of crater diameter, as calculated from the erosion model. This ratio, P , is shown for three solar elevation angles, S_s . D_s is the diameter of the largest unshadowed crater and increases with increasing S_s . C_s is the upper limit of diameter of craters in steady state. It was assumed that C_s does not vary with solar elevation angle.

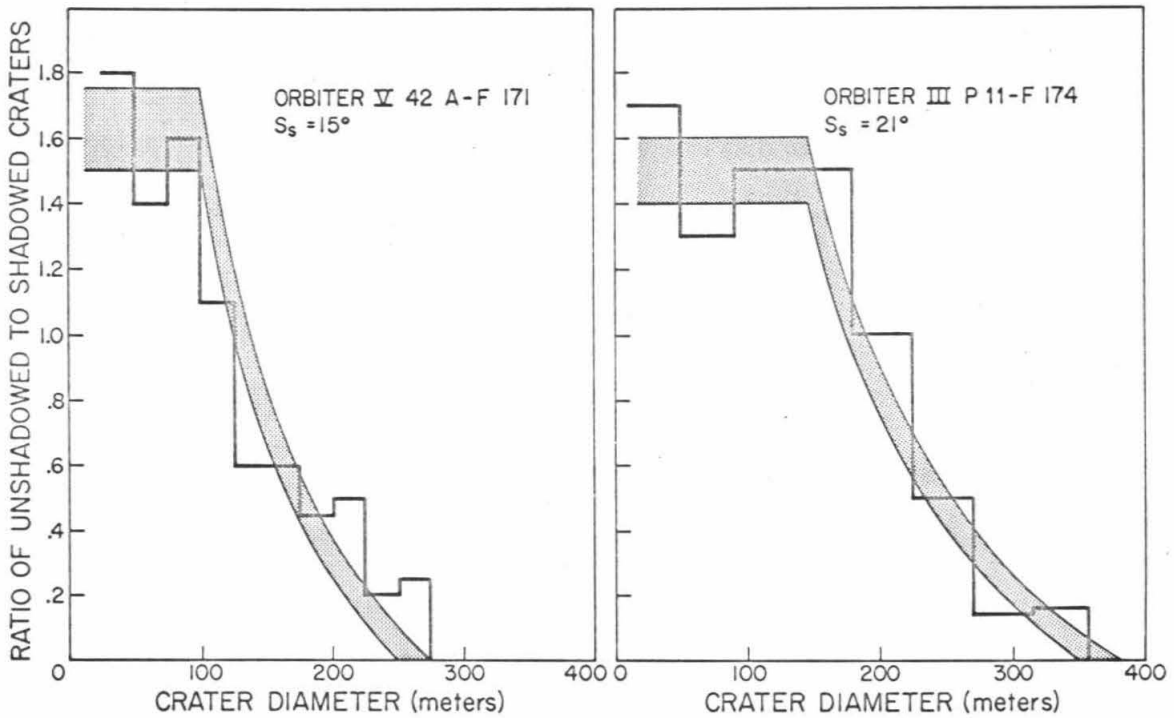


Figure 8. Comparison of the observed and predicted ratio of unshadowed to shadowed craters as a function of crater diameter. The Orbiter frames, V 42 A-F 171 and III P 11-F 174, cover the same area in Oceanus Procellarum but were taken at different solar elevation angles, S_s . The shaded areas represent the regions of acceptable fit of the theoretical model to the data. Notice that the steady state upper limit of diameter, C_s , varies with sun angle.

DISCUSSION OF RESULTS

Relative ages were determined for 73 lunar areas photographed by Lunar Orbiters III and V. A complete tabulation of the results can be found in Appendix IV. The results are presented in terms of D_L where S_f is the $\tan 4^\circ$. Figure 9 is a condensed display of the results for the major features and regions studied. Comparison of measurements by different observers using different photographic coverage imply errors in D_L of the order of 10%.

The results shown in Figure 9 indicate that the integrated flux of impacting particles varies among the different maria by as much as a factor of three. Furthermore, there are variations in the age of the surface within individual maria. This evidence indicates that not only were different maria filled at different times, but the filling of most individual maria occurred in several stages.

The rim deposits of the large rayed craters Eratosthenes, Copernicus, Aristarchus, and Tycho, were dated in this study. The integrated flux measured on these surfaces range from less than $1/30$ (Tycho) to $1/5$ (Eratosthenes) of the integrated flux on Mare Fecunditatis, the oldest mare surface dated.

Only one upland surface, the floor of the crater Hevelius, was included in this study. Upland surfaces are extremely difficult to date because they are rough and hummocky. The characteristic roughness wavelengths of these surfaces are often of the order of D_s . Hence it is difficult to recognize craters of size D_s or larger.

COMPARISON WITH PREVIOUS WORK

The chronology of the development of the lunar surface determined from the age dating methods discussed above can be compared with the results of (1) the determination of the general chronology from deposition and superposition criteria,

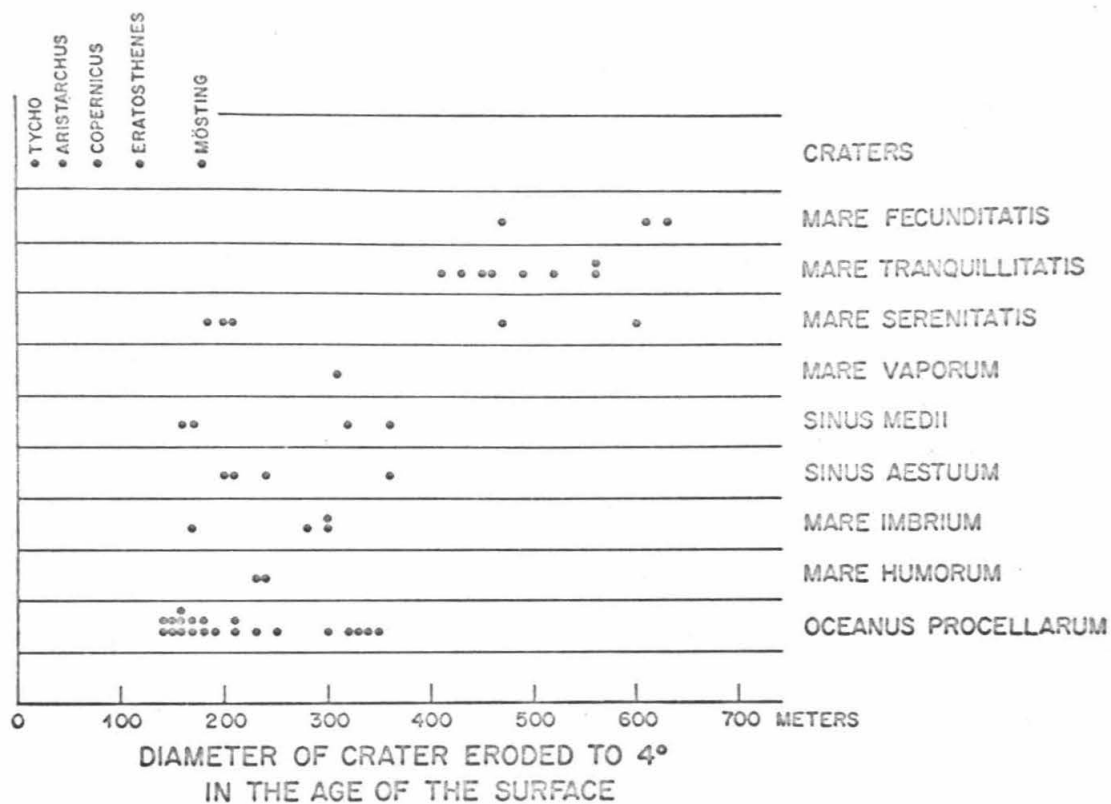


Figure 9. Relative ages of mare units and major craters. The diameter of a crater whose walls would be eroded to 4° in a time equal to the age of the surface is shown for each area studied in nine mare regions. Also shown are the relative ages of five major craters.

(2) measurements of C_s from crater counting methods, and, (3) studies of regolith thickness.

Comparison of the relative age results obtained in this study with the stratigraphic time scale developed by Shoemaker and Hackman (1962) shows good agreement. According to the lunar stratigraphic time scale the Copernican period which extended from the formation of the crater Eratosthenes to the present included the formation of large rayed craters. An examination of Figure 9 shows that the results of the present work support this theory as, Tycho, Kepler, Aristarchus, and Copernicus all have extensive ray systems. Further, both studies agree in that the formation of the crater Eratosthenes postdated the last major mare flooding event.

The upper limit of the steady state distribution, C_s , and the regolith thickness has been determined for various areas. The results of such investigations for three Surveyor landing sites (Shoemaker, et. al., 1969) and the Apollo 11 landing site (Shoemaker, et. al., 1970) are listed in Table 3 along with the values of D_L measured in this study for the same sites. The ratio of D_L to C_s is close to 3; these two diameters refer to different lower limits of slope for crater recognizability. The results are in general agreement and indicate that Surveyor VII (Tycho ejecta) is the youngest site; Surveyor I (Oceanus Procellarum) is the the youngest mare site; and Apollo 11 (Mare Tranquillitatis) is the oldest mare site.

Studies by Shoemaker, et. al. (1969) have shown that the regolith thickness increases approximately linearly with integrated flux. Thus a comparison between the radius of crater destroyed and the thickness of the regolith produced should be a linear function. The results listed in Table 3 confirm this linear relation for Surveyor sites I, V, and VII. Surveyor VI may disagree because of

local phenomena unrelated to impact.

Table 3. Comparison of results from direct crater counting (C_s) and regolith thickness with relative age measurements.

Site	C_s (meters)	D_L (meters)	Regolith Depth (meters)
Surveyor I	56	170	1 to 3
Apollo 11	141	440	3 to 6
Surveyor VI	100	330	8 to 10
Surveyor VII	3	<20	.05-.15

CALIBRATION OF RELATIVE AGE DETERMINATIONS WITH PRELIMINARY AGE RESULTS FROM APOLLO 11 AND 12

The concept of time was avoided in the preceding discussion as the history of the flux of impacting particles is not well established. It is useful to discuss absolute time scales that are implied by various cases of flux history. If the flux has remained constant since the beginning of the period of mare formation, D_L is approximately proportional to the age of the surface. Under these circumstances, the Imbrian or period of mare formation would have been by far the longest of the lunar geologic periods, greater than twice the length of the combined Eratosthenian and Copernican periods.

It is also possible that the period of mare filling was a relatively short period by comparison to the Eratosthenian and Copernican periods. The differences in integrated flux on different maria would then indicate that the flux rates were rapidly decreasing through the Imbrian period. Thus the whole period of mare formation could have been a short period following the accretion phase.

A third possibility is that the fluxes have actually increased since the beginning of the Imbrian period. In this case most of the lunar history would fall within the Imbrian period.

The preliminary age determinations for the Apollo 11 and 12 samples afford an opportunity to test these hypotheses. Although the results for the Apollo 12 site are still very rough, potassium-argon methods suggest that crystallization ages of rocks collected at the Apollo 12 landing site are of the order of a billion years younger than those of Apollo 11 (Lunar Sample Preliminary Examination Team, 1970). The integrated fluxes or sizes of crater destroyed at the Apollo 11 and 12 sites are about in the same proportion as the preliminary crystallization ages. It will be assumed here that the flux has been constant since the formation of Mare Tranquillitatis. On the basis of this assumption the absolute ages of Apollo 12 and future landing sites can be estimated from the crystallization ages of the Apollo 11 samples, using the integrated flux information obtained in this study. The degree to which these predictions agree with final results of direct age determinations for samples from Apollo 12 and future sites will test the assumption of constant flux. Figure 10 shows the relation between size of crater destroyed, D_L , and absolute surface age under the assumption of constant flux. The slope of the curve is controlled by rubidium-strontium crystallization ages of Apollo 11 samples determined by Albee, et. al. (1970). Also shown in Figure 10 are the ages of the surfaces at the Apollo 12 and the Marius Hills Apollo landing site that would be compatible with constant flux. The Marius Hills are located in western Oceanus Procellarum which contains the youngest mare surfaces found in this study. Thus, if the assumption of constant flux is approximately correct, the period of mare formation occurred from more than 4 billion to about 1.5 billion years ago.

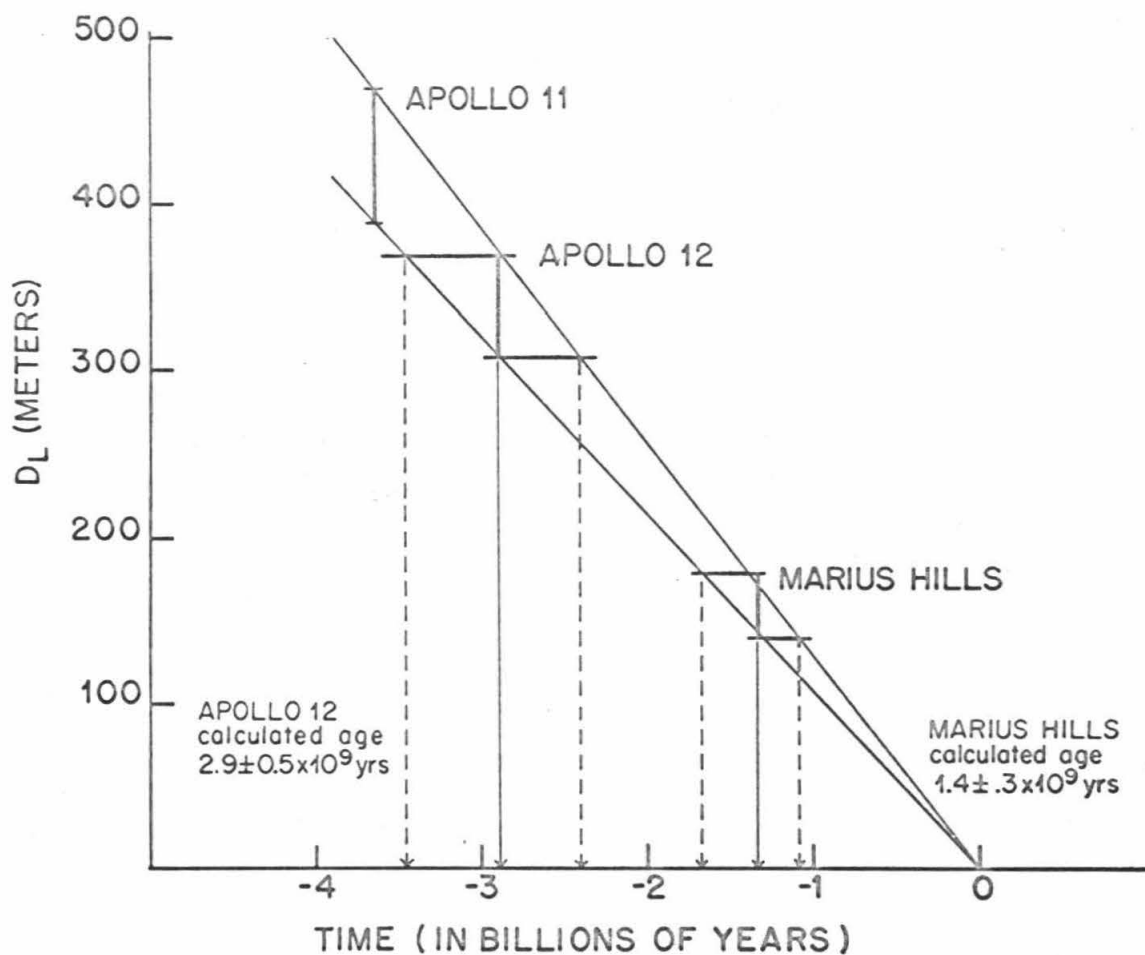


Figure 10. Absolute ages of Apollo landing sites derived from the crystallization age of Apollo 11 and assuming a constant flux of impacting particles.

Recent evidence from studies of the exposure ages of Apollo 11 rocks to solar particles and galactic cosmic rays are compatible with a constant turnover rate in the lunar regolith during the last 4 billion years. The exposure ages of various rocks are generally in the range from 50 to 500 million years. These lunar samples were taken near the surface. If the flux of meteoritic material was much greater 3 billion years ago than it has been in the last 1 billion years, for example, most of the observed regolith would have been developed during the early history of Mare Tranquillitatis and the surface left relatively undisturbed since that time. The residence time of a rock fragment would have been much greater than the observed exposure ages. Shoemaker, et. al. (1970) have shown that the observed exposure ages are, in fact, roughly compatible with a constant turnover rate throughout the age of Mare Tranquillitatis. This conclusion is valid provided the meteoritic, solar particle, and galactic cosmic ray fluxes have not had the same historical variations, which is rather unlikely. As the turnover rate is proportional to the flux, this evidence further suggests that the flux of impacting particles has been constant since the Tranquillity basalts were crystallized.

CONCLUSIONS

The conclusions of the studies described in this chapter are divided here into two groups: those conclusions that are based solely on estimated integrated fluxes and those conclusions that are based on the assumption of constant flux. Conclusions related to an assumed constant flux are less reliable as they rest on an assumption that is presently unverified.

From the impact erosion model and its application to Orbiter photography

it is concluded that:

(a) The erosion of lunar craters occurs primarily by downslope transport of material ejected by impact of small objects which individually produce small changes in the form of the eroded crater.

(b) The observed size-frequency distribution of craters on the maria with diameters less than about 100 meters can be explained as a steady state population produced from the action of such an erosion process on craters whose distribution follows the observed production distribution.

(c) The observed slope-frequency distribution of lunar crater walls agrees with that produced by such an erosion process.

(d) The measured integrated fluxes are compatible with observed regolith thicknesses.

(e) The variations in integrated flux between maria and within individual maria indicate that various maria were formed at different times and individual maria were formed in different stages.

Comparison of the relative ages determined in this study with the preliminary crystallization ages obtained for the Apollo 11 and 12 rocks indicate that:

(a) The absolute age of the Apollo 12 site estimated from the age determined from laboratory studies of Apollo 11 rocks and an assumption of constant flux is compatible with the preliminary results of direct age determination for the Apollo 12 rocks.

(b) The period of mare formation was the longest of the lunar geologic periods, lasting from about 4 billion to about 1.5 billion years ago.

IV. THE SEQUENCE OF FORMATION OF REGIONAL MARE UNITS

The results described in Chapters II and III can be combined to establish the broad outline of the evolution of the lunar maria. The history of the formation of the maria is complex; individual maria contain a variety of lithologic units which were emplaced at different times. Studies of cosmic ray exposure ages of Apollo samples and estimates of the integrated flux of particles in various mare regions suggest that the period of mare formation lasted billions of years. Furthermore, the studies of spectral reflectance demonstrate that there is a correlation between the structural and morphological types of lunar maria and the spectral classes of material which have been deposited within them. Such correlations between the ages, distributions, and morphologies of lithologies in the lunar maria place stringent restrictions on the genesis of maria and the evolution of the lunar interior. The purpose of this chapter is to outline those correlations and to provide a useful summary of the results of this work.

MAJOR STAGES OF MARE FORMATION

The distribution of mare lithologies mapped in this study is in the northeast quadrant of the moon. The distributions of material by spectral type in other regions was obtained from composite ultraviolet-infrared photographs taken by Whitaker (Kuiper (1965)) which were calibrated, where possible, with reflectance data taken by McCord (1968); McCord, Johnson, and Kieffer (1969); and McCord and Johnson (1969).

A direct comparison of the spectral types and relative ages of a large number of lunar areas is shown in Figure 11. Individual units of uniform

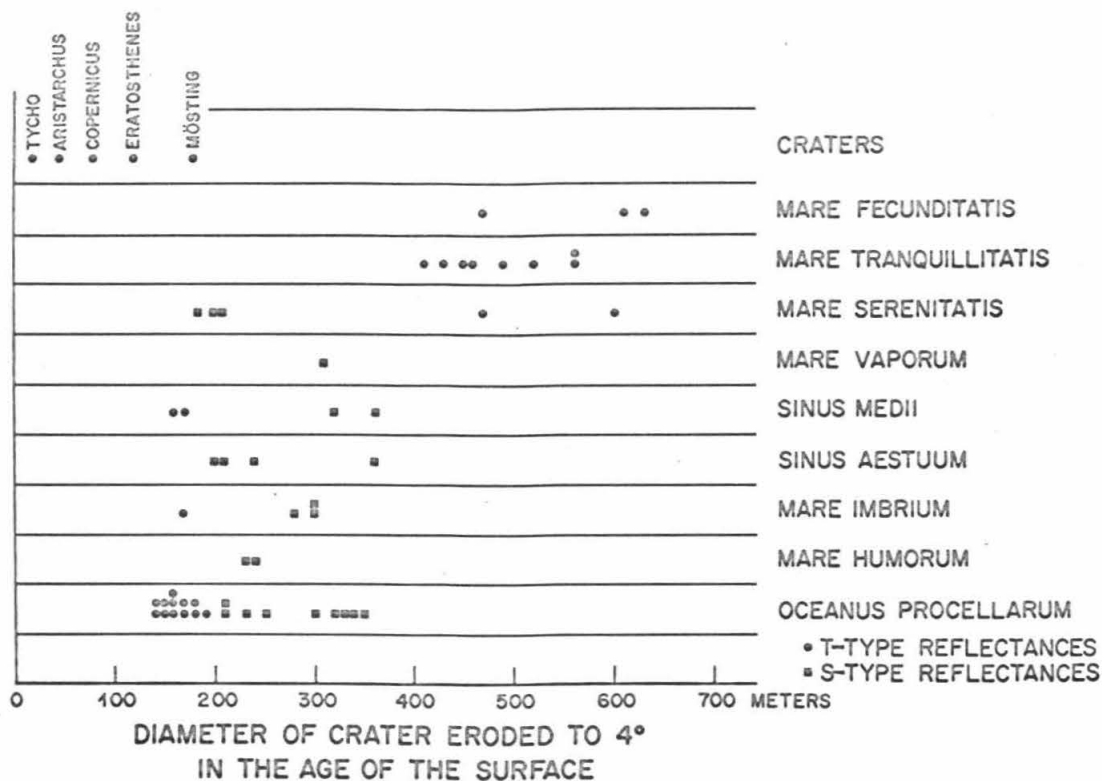


Figure 11. Spectral reflectance type and relative age of units in the lunar maria. Regions are included for which both the relative ages and spectral types are known. The T-type reflectance includes spectral types Tr, T and Tb; S-type includes Sr, S and Sb.

spectral reflectance have constant relative ages over their surfaces.

As shown by Figure 11, there have been three major stages in the deposition of mare materials. The first stage includes the formation of extensive units in Mare Tranquillitatis and Mare Fecunditatis and units on the perimeter of Mare Serenitatis (Littrow unit and material southwest of Sulpicius Gallus) all of which exhibit spectral reflectances similar to that of Mare Tranquillitatis (T-type, including Tr, T, and Tb). The second stage involved the filling of the circular maria, Mare Serenitatis, Mare Imbrium, and Mare Humorum, and the emplacement of various minor units in Oceanus Procellarum, Sinus Medii, and Sinus Aestuum all of which have spectral reflectances similar to those found in Mare Serenitatis (S-type, including Sr, S, and Sb). The last major epoch in the formation of the lunar maria includes the deposition of extensive thin deposits in Oceanus Procellarum, Mare Imbrium, and Sinus Medii all of which have spectral reflectance like that of Mare Tranquillitatis (T-type, including Tr, T, and Tb).

A fourth period, apparently devoid of major events of mare formation extended from the end of deposition of the maria of the third stage to the present. This last period has a length, assuming constant flux of impacting bodies, of $1.4 \pm .3$ billion years (See Figure 10, Chapter III) and includes the formation of the Copernican and Eratosthenian craters: Mösting, Eratosthenes, Copernicus, Aristarchus, Kepler, and Tycho.

SEQUENCE AND DISTRIBUTION OF LITHOLOGIES IN INDIVIDUAL MARIA

Mare Fecunditatis

Mare Fecunditatis contains the oldest mare surface dated in this study. Units in that mare are of spectral type T and were emplaced during the first

stage of mare formation described above.

Mare Tranquillitatis

This region is the type locality in this study for the T-type maria and contains units which were deposited in the first stage of mare formation. Units appear to have been deposited at several different times; as errors in relative age are large for the old maria, however, this observation is tentative.

Mare Serenitatis

The deposition of mare units in Mare Serenitatis occurred both in the first and second stages of mare formation. Two small units along the perimeter of the basin, the Littrow unit and material southwest of the crater Sulpicius Gallus, are T-type and were formed in the first stage of mare formation. The major part of Mare Serenitatis consists of S-type or red materials. The ages of these materials fall within a small range within the second stage. Mare Serenitatis is the type locality in this study of material with S-type spectral reflectances.

Mare Vaporum

The main rock type in Mare Vaporum has S-type reflectance and was emplaced during the second stage of mare formation.

Mare Imbrium

The largest circular mare on the moon, Mare Imbrium, contains units that were deposited during the second and third stages of mare formation. The predominant unit within this basin consists of S-type materials layed down during the second stage of mare formation. This unit is found in north, northwestern and eastern Mare Imbrium. Whitaker's composite photographs show that this unit is bounded around the northern and eastern

perimeter of Mare Imbrium by the Fra Mauro Formation. A second major unit found in this basin is a thin T-type deposit emplaced during the third stage. Because of the similarity in morphology, age, and spectral reflectance of this unit to units in Oceanus Procellarum immediately to the southwest, this unit in Mare Imbrium is probably a northern extension of these Oceanus Procellarum flows.

Sinus Medii

Sinus Medii includes material deposited in the second and third stages of mare formation. The region south of a small mare ridge near the Surveyor VI landing site has S-type spectral reflectance (McCord, Johnson, and Kieffer, 1969) and was deposited during the second stage of mare formation. Materials north of the ridge, however, were deposited during the third stage of mare formation. Examination of Whitaker's composite photographs suggest that this area represents T-type material; identification is difficult, however.

Mare Humorum

Mare Humorum was filled during the second stage of mare formation with material exhibiting S-type spectral reflectance. Identification of the spectral type is questionable.

Oceanus Procellarum

The emplacement of mare material in Oceanus Procellarum occurred during the second and third stages of mare formation. Two minor units of S-type reflectance were deposited during the second stage. These units are north of Aristarchus and southwest of Landsberg in the vicinity of the Apollo 12 landing site. The major part of the Oceanus Procellarum was flooded with T-type mare material in the third state of mare formation. The

areal extent of these later units is of the order of one-half of a million square kilometers.

CONCLUSIONS

The general results of this study are summarized in Figure 12, which compares the lunar stratigraphic time scale, the integrated flux scale, and the approximate absolute time scale. Also shown is the relationship between crater morphology and spectral type (T and S). The error bars in the diagram refer to uncertainties in measured integrated flux or diameter of crater eroded to 4°.

The following important conclusions implied by this research can be summarized as follows:

(a) The formation of the lunar maria can be divided into three major epochs, each epoch associated with the deposition of materials of one spectral type.

(b) Two distinct kinds of maria exist which are distinguished in their morphologies, relations with regional structure, thicknesses, associations with gravity anomalies, times of formation in the lunar record, and spectral types.

(c) On the basis of an assumption of constant flux it is estimated that the major period of mare formation (Imbrian) lasted from about 4 billion until about 1.5 billion years ago.

(d) Individual maria have complicated histories; they contain a variety of lithic units emplaced at different times.

(e) The dominant surface process, other than mare formation, which has created and destroyed topography is impact of primary and secondary fragments.

Variations from region to region in the size-frequency distribution of craters, slope-frequency distribution of crater walls, and regolith thickness are compatible with processes of impact crater production and erosion.

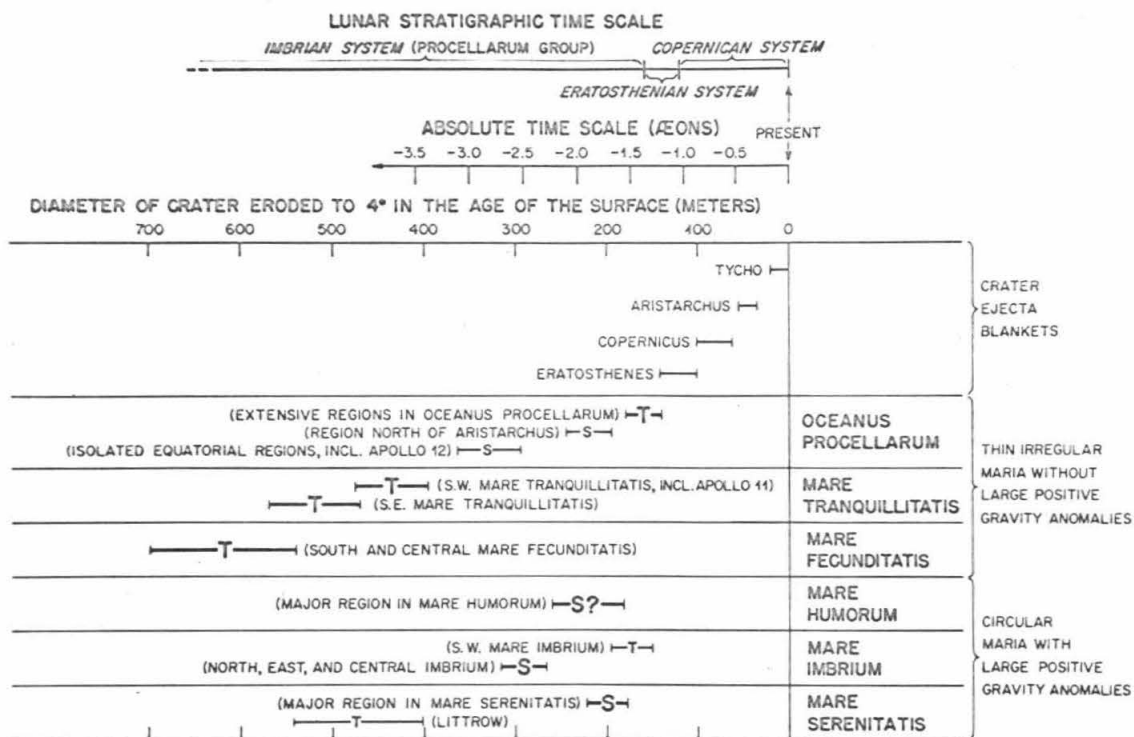


Figure 12. Comparison of ages, regional morphologies and spectral reflectance types of units in the lunar maria. The spectral reflectance types T (including T_r , T and T_b) and S (including S_r , S , and S_b) are shown for individual units in the maria. Boldface letters are used for major units; smaller letters are used for minor units of small areal extent. The error bars denote uncertainties in measurements of the diameter of crater eroded to 4° in a time equal to the age of the surface. The absolute time scale was derived from Apollo 11 crystallization ages under an assumption of constant flux of impacting particles. Also shown is the Lunar Stratigraphic Time Scale developed by Shoemaker and Hackman (1962).

APPENDIX I

SPECTRAL REFLECTANCE MAPPING: OBSERVATIONAL
TECHNIQUES AND DATA REDUCTION

INTRODUCTION

The importance and relevance of visible reflectance spectra in determining the composition and studying the compositional variations of planetary surfaces has been discussed by several authors. With the return of lunar samples such remote sensing techniques have become exceedingly important tools for extending the knowledge of the composition of a few landing sites to other areas of the moon.

There are two approaches to interpretation of reflectance spectra in connection with the formation and modification of a planetary surface. The first involves a direct determination of the surface composition in the ordinary sense of spectral analysis. In the case of visible reflectance spectra, the solid absorptions are not at all well understood. A unique determination of composition is very difficult to achieve since so many variables concerned with structure and mineralogy of geologic materials control their reflectance spectra. Little progress has been made in that particular direction.

The second approach is to map the areal variations of the reflectance spectra in order to study the relationships between mappable spectral units and variations in albedo, morphology, and age. This is the approach taken in this investigation.

Normalized lunar relative reflectance curves obtained by McCord (1968) indicate that a minimum of three narrow-band reflectance measurements between 0.4 microns and 0.7 microns are required to resolve each of the spectral types. The centers of these bandpasses were chosen at 0.4 microns,

0.52 microns and 0.7 microns. The mapping was done photoelectrically rather than photographically in order to permit measurement of small spectral variations ($\sim 1\%$) across the large albedo variations (50% - 200%). Such measurements are not possible photographically because sufficiently precise and consistent calibrations of films over the required dynamic range cannot be achieved.

INSTRUMENTATION AND OBSERVATION

Observations were made at the bent-Cassegrain focus of the Mount Wilson 24-inch telescope. A single beam of photoelectric photometer was used with an 18 arc sec aperture corresponding to a diameter of about 30 km at the sub-earth point on the lunar surface. The narrow band ($.02\mu$ width) interference filters centered at .4 microns, .52 microns and .7 microns were placed between the aperture and a cooled ITT FW 130 (S-20) photomultiplier tube. The signals were recorded with a highspeed pulse-counting data system.

Lateral variations in the lunar reflectance spectrum were measured by scanning strips 130 arc sec in length and 18 arc seconds in width twice in each of the three filters. The telescope was moved continuously during each scan at the rate of 13 arc sec/sec. Samples were taken along the scan after integration periods of .35 seconds separated by .80 seconds of recording time. This allowed an overlap of about 35% between consecutively sampled areas. This choice of spacing was made to minimize aliasing and to maximize coverage. Nine samples were taken per scan. Before and after each line was scanned a standard area in Mare Serenitatis (17.6°N , 19.4°E) was measured. The period between standard measurements was about 5 minutes.

GENERAL METHOD AND DATA REDUCTION

The measurement of such reflectance variations is complicated by scan position errors, short and long period atmospheric transmission errors, and statistical pulse counting errors. This section is intended to describe how these effects are minimized and to provide a foundation for interpreting the results.

At some time, t , and at a lunar phase angle, α , a strip along the lunar surface reflects radiation in the direction of an observer. The width of the strip is controlled by the field of view of the instrument. This radiation can be represented by a function $B(x, \lambda)$ which is the brightness averaged across the strip in the intervals $x \rightarrow x+dx$ and $\lambda \rightarrow \lambda+d\lambda$, where x is the coordinate along the strip and λ is the wavelength of the radiation. Without loss of generality, $B(x, \lambda)$ can be written

$$B(x, \lambda) = G(x) C(x, \lambda) S(\lambda)$$

and (1)

$$C(x, \lambda_0) = 1$$

where $S(\lambda)$ is the solar insolation, $G(x)$ the albedo variations along the strip, and $C(x, \lambda)$ the differential wavelength dependence along the strip. Here λ_0 is taken to be 0.52 microns, so that, the reflectance spectrum, $C(x, \lambda)$, is normalized at 0.52 microns. In general, variations in $C(x, \lambda)$ from area to area seldom exceed 10% whereas $G(x)$ can vary by factors of 2 or 3.

The transmission of the earth's atmosphere can be written as the sum of two functions

$$(2) \quad A(\lambda, z, t) = T(\lambda, z) + V(\lambda, t)$$

$T(\lambda, z)$ is a secular variation dependent on wavelength and the thickness of the atmosphere traversed; $V(\lambda, t)$ is a smaller, high frequency variation, the amplitudes of which are of the order of 2% under nominal conditions. Some periods of $V(\lambda, t)$ are longer than the integration times of the measurement, and thus it constitutes a major source of noise.

The instrument response is characterized by the spatial and spectral windows $W(x)$ and $F_i(\lambda)$ where the index, i , refers to the i th filter. $W(x)$ has the form of a symmetric trapezoid and depends on the instrument aperture diameter and the scan rate; $F_i(\lambda)$ is the transmission of the i th filter (Figure 13). The j th sample along a scan taken in the i th filter can be written

$$(3) \quad S_{i,j} = \int_{-\infty}^{\infty} \int_{-\infty}^{\infty} G(x') C(x', \lambda) T(\lambda, z) S(\lambda) \\ \cdot F_i(\lambda) W(j\Delta x - x') d\lambda dx' \\ + \text{noise from } V(\lambda, t)$$

To a high degree of precision (<0.1% error for lunar areas), $C(x, \lambda)$ can be considered constant over the bandpass ($\sim 0.3\mu$). Then equation (2) becomes

$$(4) \quad S_{i,j} = \int_{-\infty}^{\infty} T(\lambda, z) S(\lambda) F_i(\lambda) d\lambda \\ \cdot \int_{-\infty}^{\infty} G(x') C_i(x') W(j\Delta x - x') dx' \\ + \text{noise}$$

where $C_i(x)$ is the wavelength average of $C(x, \lambda)$ over the bandpass of the i th filter. The unknown atmospheric dependencies in the first integral in equation (4) are eliminated by forming the ratio between the scan sample, $S_{i,j}$, and a

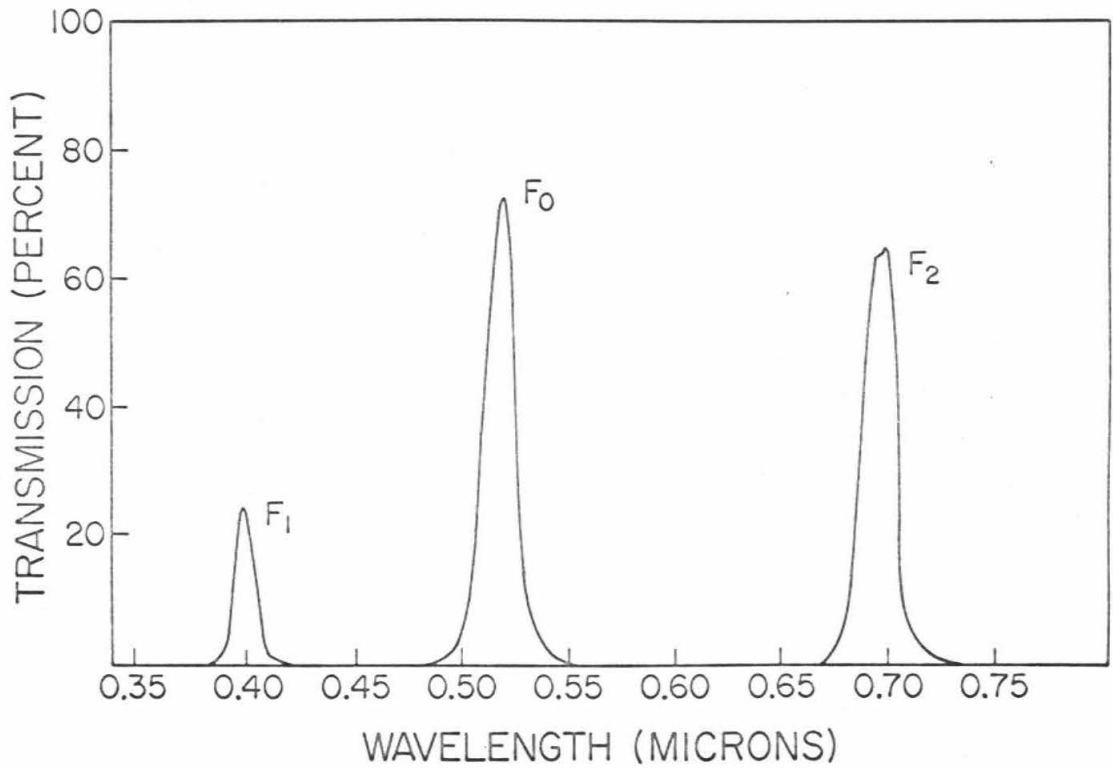


Figure 13. The transmissions of the three narrow band filters. The band-passes are centered at 0.4μ , 0.52μ , and 0.7μ .

stationary observation of the standard area. This ratio, $R_{i,j}$, can be written

$$(5) \quad R_{i,j} = \frac{\int_{-\infty}^{\infty} G(x') C_i(x') W(j\Delta x - x') dx'}{A G_s C_{s_i}}$$

G_s and C_{s_i} are the functions $G(x)$ and $C_i(x)$ evaluated at the standard; A is the area of the aperture.

$R_{i,j}$ is then normalized to one wavelength, that is, divided by $R_{o,j}$ where "o" refers to the wavelength λ_o . The ratio, $D_{i,j}$, is

$$D_{i,j} = \frac{1}{C_{s_i}} \frac{\int_{-\infty}^{\infty} G(x') C_i(x') W(j\Delta x - x') dx'}{\int_{-\infty}^{\infty} G(x') W(j\Delta x - x') dx'}$$

In practice $D_{i,j}$ cannot be obtained directly by dividing $R_{i,j}$ by $R_{o,j}$, because, due to errors in the position of the initial sample in each scan, the sampled points of $R_{i,j}$ are shifted relative to those of $R_{o,j}$. Since the variations in $G(x)$ are large compared to those of $C_i(x)$, small shifts in sample point position produce large pseudo-color variation in the ratio, $D_{i,j}$. The relative shift between the two scans is found by considering $C_i(x)$ a small residual and shifting the scans relative to one another until the pseudo-color variations are minimized. The numerical technique used in this operation adds high frequency noise which is later removed by low pass filtering (Figure 14). The filter used has an upper cutoff slightly below the Nyquist frequency of the original sampling. Thus the low frequency content is preserved. The reduced data appears in the form

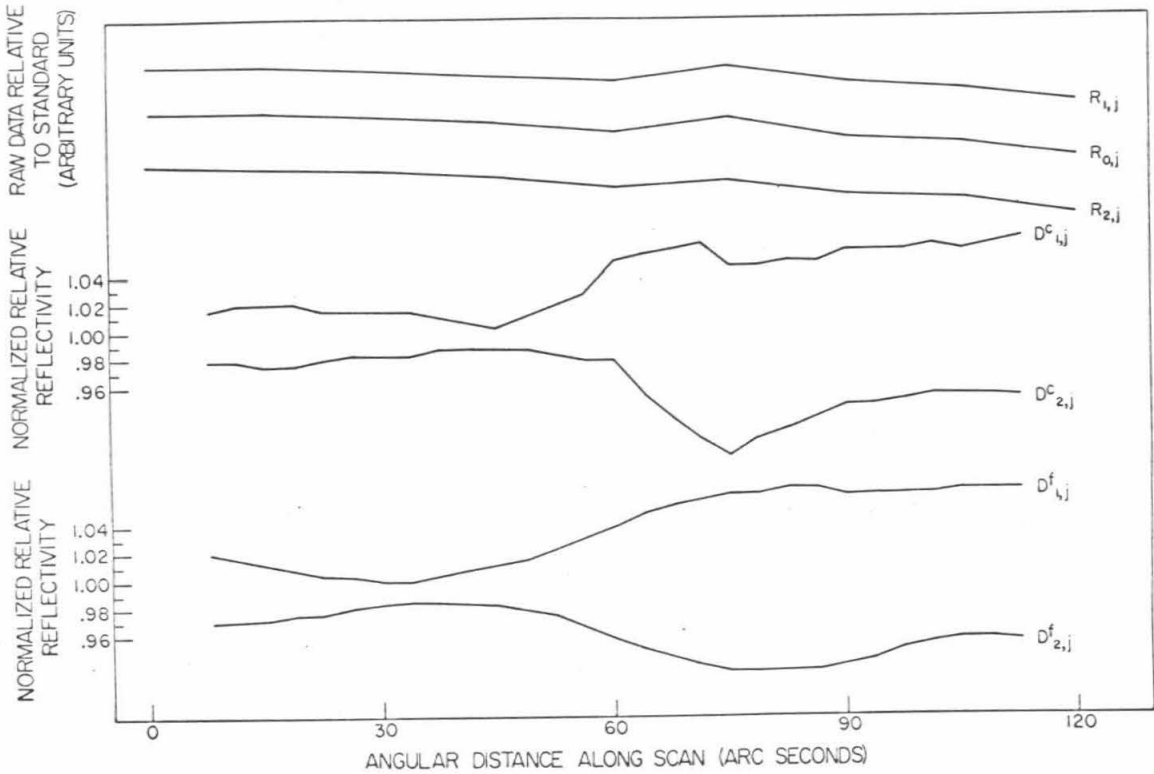


Figure 14. Data reduction sequence. Curves $R_{1,i}$, $R_{0,i}$, and $R_{2,i}$ represent the luminance measured along a scan line in the three filters relative to the luminance measured at the standard area in Mare Serenitatis. Subscripts 1, 0 and 2 refer to 0.4μ , 0.52μ and 0.7μ respectively. Curves $D_{1,i}^c$ and $D_{2,i}^c$ are the simple ratios: $R_{1,i}/R_{0,i}$ and $R_{2,i}/R_{0,i}$. Curves $D_{1,i}^f$ and $D_{2,i}^f$ are the smoothed versions of $D_{1,i}^c$ and $D_{2,i}^c$ obtained by low-pass filtering. The filter has an upper cut-off below the spatial frequency of the sampling and is used to remove registration artifacts in $D_{1,i}^c$ and $D_{2,i}^c$.

$$(7) \quad D_{i,j}^f = \frac{1}{C_{s_i}} \frac{\int_{-\infty}^{\infty} G(x') C_i(x') W(j\Delta x - x') dx'}{\int_{-\infty}^{\infty} G(x') W(j\Delta x - x') dx} * F$$

where F is the low pass filter.

This form minimizes the effects of the albedo and insolation function $G(x)$. Along those portions of a scan where $C_i(x)$ is constant $D_{i,j}^f$ becomes

$$(8) \quad D_{i,j}^f = \frac{C_i(x)}{C_{s_i}}$$

and represents the normalized reflectance along the scan relative to the normalized reflectance of the standard. Equation (7) is applicable at color boundaries and will be used in a later section concerning the recognition and location of such boundaries.

Four determinations of $D_{i,j}^f$ were made for each line in each filter pair. These were averaged to reduce random noise.

BOUNDARY RECOGNITION AND CLASSIFICATION OF SPECTRAL TYPES

Because of the presence of noise in $D_{i,j}^f$, due primarily to variations in atmospheric transmission (nominally 2%), it is not possible to simply equate variations in $D_{i,j}^f$ of amplitude 2% or smaller with minor spectral variation or color boundaries. In order to recognize minor color boundaries, it is necessary to invoke one of two criteria: (1) the variations are correlated between scan lines or, (2) the change is anticorrelated between the two color ratios, $D_{i,j}^f$ ($i = 1, 2$), along the scan. The first criterion is obvious as the lines are independent of one another; the second requires explanation. If the scans are anticorrelated, the variation cannot be due to noise in a

single filter, as $R_{o,i}$ appears in the denominator of both $D_{i,i}^f$ ($i = 1, 2$). The functions $R_{i,i}$ ($i = 1, 2$) are independently determined. This criterion is sensitive to rotations of the spectra about .52 microns which include most major spectral variations.

The positions of the boundaries can be obtained by using a model boundary and comparing it with features in $D_{i,i}^f$. This was done by using a step-function model of a boundary and calculating its form as it would appear in $D_{i,i}^f$ from equation (7) (Figure 15). This forward-calculated model boundary was used as a matched filter and autocorrelated with $D_{i,i}^f$. The positions of the positive and negative peaks in the autocorrelation correspond to the boundary positions. If the peaks are out of phase, then the changes in $D_{i,i}^f$ are anticorrelated. An example of the autocorrelation of this match filter with $D_{i,i}^f$ is shown in Figure 16.

The next step in the treatment of the data is to obtain the distribution of spectral types. It is important to discern whether these types represent a continuous distribution or fall into discrete categories. This is done by contouring the density of all lunar points in a plot of normalized relative reflectance at 0.4 microns versus that at 0.7 microns (Figure 17a). Points which occur at or near color boundaries are not included in this plot since they would display an artificial mixing between two distinct spectral types. The boundary positions are taken from the autocorrelation spectra described above. From the plot in Figure 17a at least four discrete types are recognizable. It is also apparent from this figure that the variation between spectral types occurs primarily in the form of a rotation of the spectrum about 0.52 microns. Thus the technique for boundary recognition which was outlined above should be sensitive to most color boundaries.

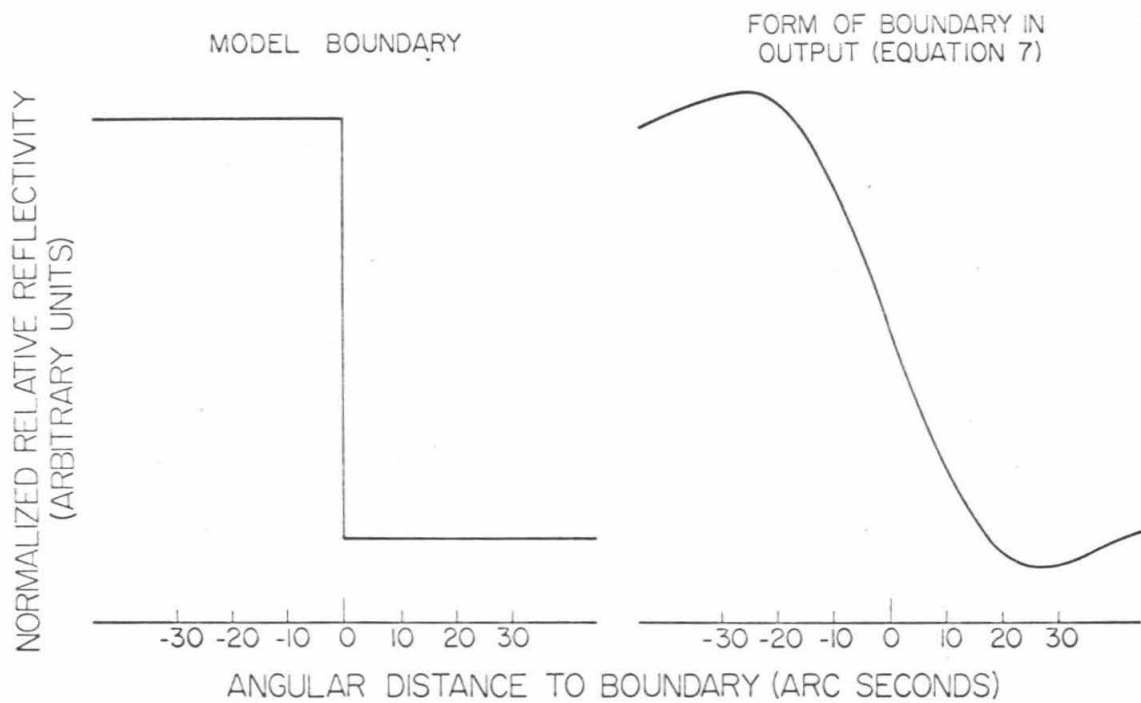


Figure 15. The step-function model boundary and its output from used to recognize and locate color boundaries in $D_{1,i}^f$ and $D_{2,i}^f$.

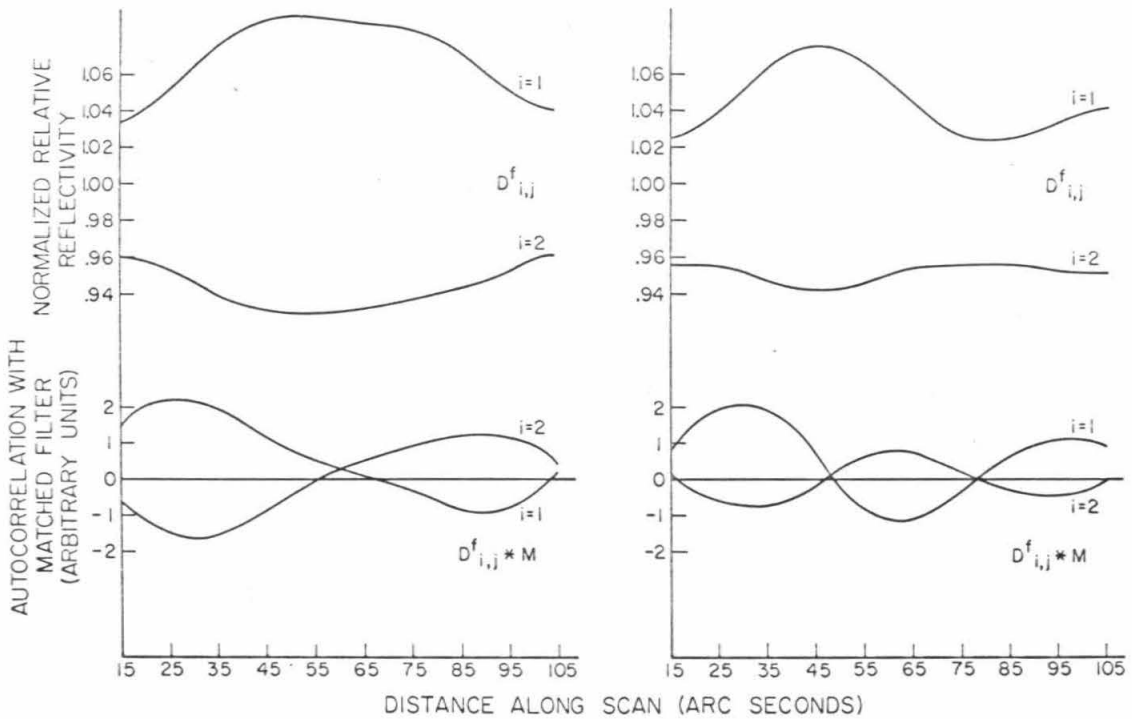


Figure 16. Location of color boundaries. Examples of $D_{i,j}^f$ are shown along with the autocorrelations of $D_{i,j}^f$ with the model boundary, M , in its output form shown in Figure 15. Peaks in the autocorrelation give the positions of color boundaries. Notice that the autocorrelations are anticorrelated at color boundaries.

The spectral type of each point along a scan is identified by comparing its reflectance values with the type fields shown in Figure 17b. Final maps are then compiled from the boundary position data and the spectral types which occur between the boundaries. Figures 18a and 18b show two stages in the development of such maps. In Figure 18a the boundary and type information is plotted in the scan grids. Figure 18b was produced by transferring this information to a lunar photograph. Solid lines are drawn when color boundaries coincide with albedo boundaries. Dashed lines are used when no sharp morphologic or albedo boundary is visible at a color boundary.

VALIDATION AND ACCURACY

The consistency and precision of the mapping technique can be tested in a variety of ways. Figure 19 shows normalized reflectance curves taken from McCord (1968) compared with reflectance values for the same lunar area measured in this study. Both sets of data are normalized to the same standard area in Mare Serenitatis. The mean deviation of the scanned data from the data of McCord (1968) is about 1%.

A second test of consistency is shown in Figure 18a. Maps of one area produced from data taken on different nights and at different phase angles are compared to demonstrate that both the spectral types and boundary positions were reproducible. Since the scans were not taken at precisely the same lunar positions, albedo boundaries which coincide with color boundaries are sketched in to better demonstrate the agreement.

The linear response of the photoelectric system over a wide range of luminance is demonstrated at boundaries such as that between Mare Crisium and the uplands to the west. The albedo changes approximately a factor of

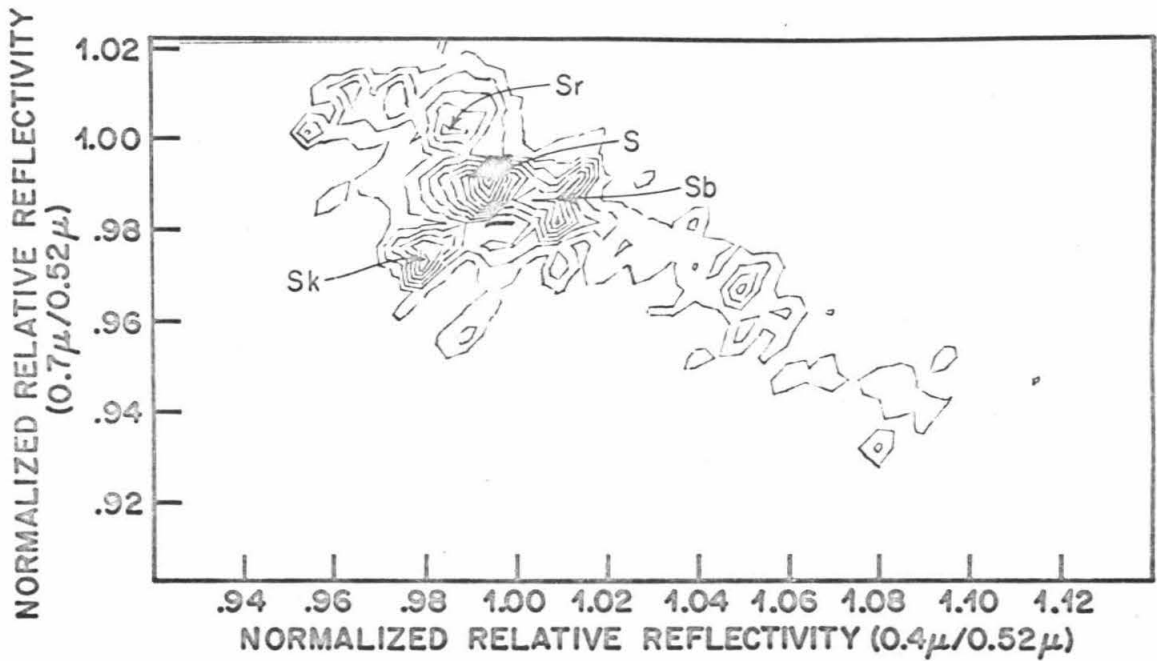


Figure 17a. The bivariate frequency distribution of lunar reflectance spectra. Each point was plotted as a point representing its normalized relative reflectance at 0.4μ and 0.7μ . The density of all such points was contoured. The contour interval is 5 points per grid cell (0.005 on each side in units given in the figure).

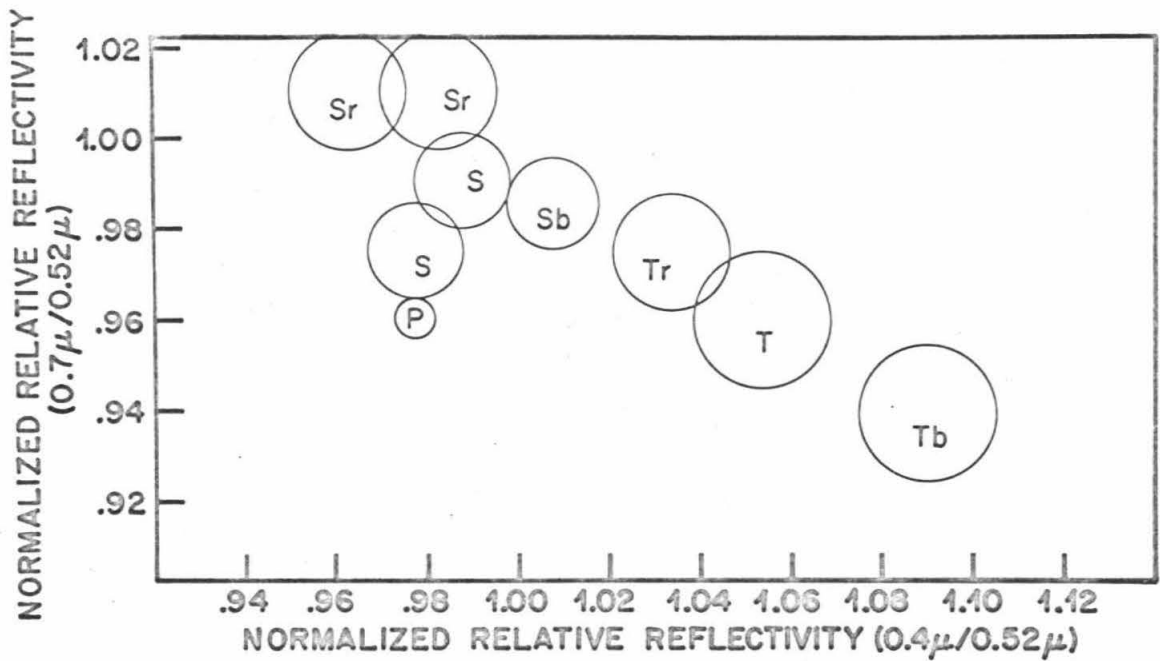
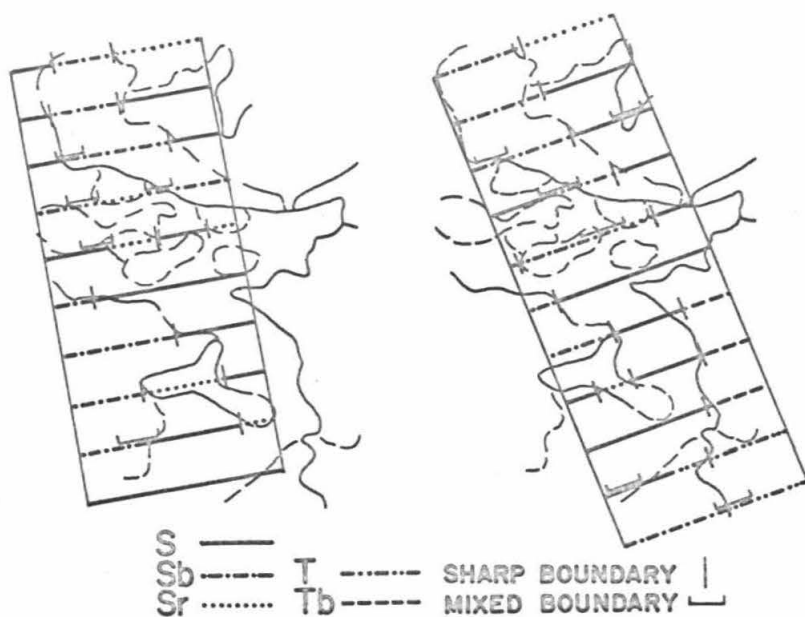
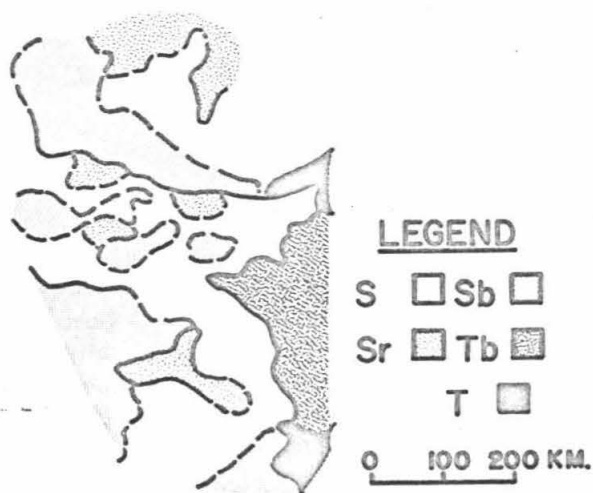


Figure 17b. The regions used to classify the reflectance of each point along the lunar scans. Points resting outside of all or within two of the circles were not classified. Points resting inside individual circles were labeled with the corresponding symbols that are shown.



(a)



(b)

Figure 18. Stages in the construction of regional maps. (a) The positions of color boundaries and distributions of spectral types identified along two sets of scans of one area are compared with the albedo boundaries in that area. (b) A map of the distribution spectral types is produced by comparing albedo boundaries with color changes along scan lines.

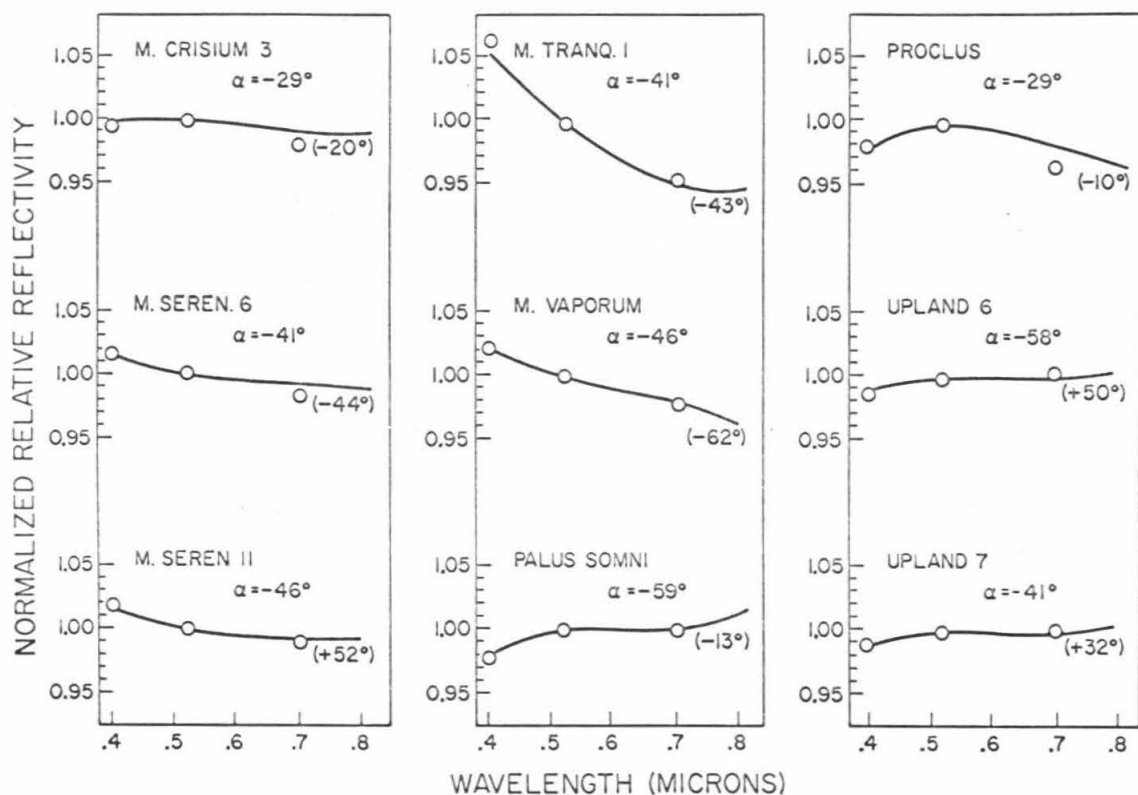


Figure 19. Comparison of normalized relative reflectance values with those measured by McCord (1968). The circles represent the values obtained in the present study; the phase angle α , is given for each measurement. Solid lines represent the reflectance spectra obtained by McCord (1968); phase angles of those observations are given in parentheses. Site names are those used by McCord.

2 across this boundary; no color boundary was detected (Figure 20). The similarity of the spectral types to the east and west of this boundary was documented by McCord (1968).

The validity of the method is further demonstrated by the correlation in spectral type and boundary position between independent scan lines. In addition, many of the boundaries are coincident with marked albedo boundaries. By comparison with the position of such marked albedo boundaries, the errors in the measured positions of color boundaries are estimated to be generally less than $1/2$ the aperture diameter (about 15 km). Much higher resolutions (< 3 km) can be obtained by using smaller apertures and slower scan rates. This would reduce the areal coverage, however, and require a much more accurate telescope tracking capability.

The dominant sources of noise are statistical pulse counting errors ($1/N^{1/2}$ about 1%) and variations in atmospheric transmission (nominally about 2%) which have periods less than a few minutes. Hence the mean deviation of the average of four determinations of $D_{i,i}^f$ is expected to be about 1%.

SUMMARY

The technique presented here is adequate to (1) map variations in the normalized reflectance of the moon with amplitudes greater than about 1%, (2) locate the boundaries between major spectral units with an accuracy of about 15 km, and, (3) identify the spectral types of the units mapped and determined whether these types form a continuous progression or fall into distinct categories.

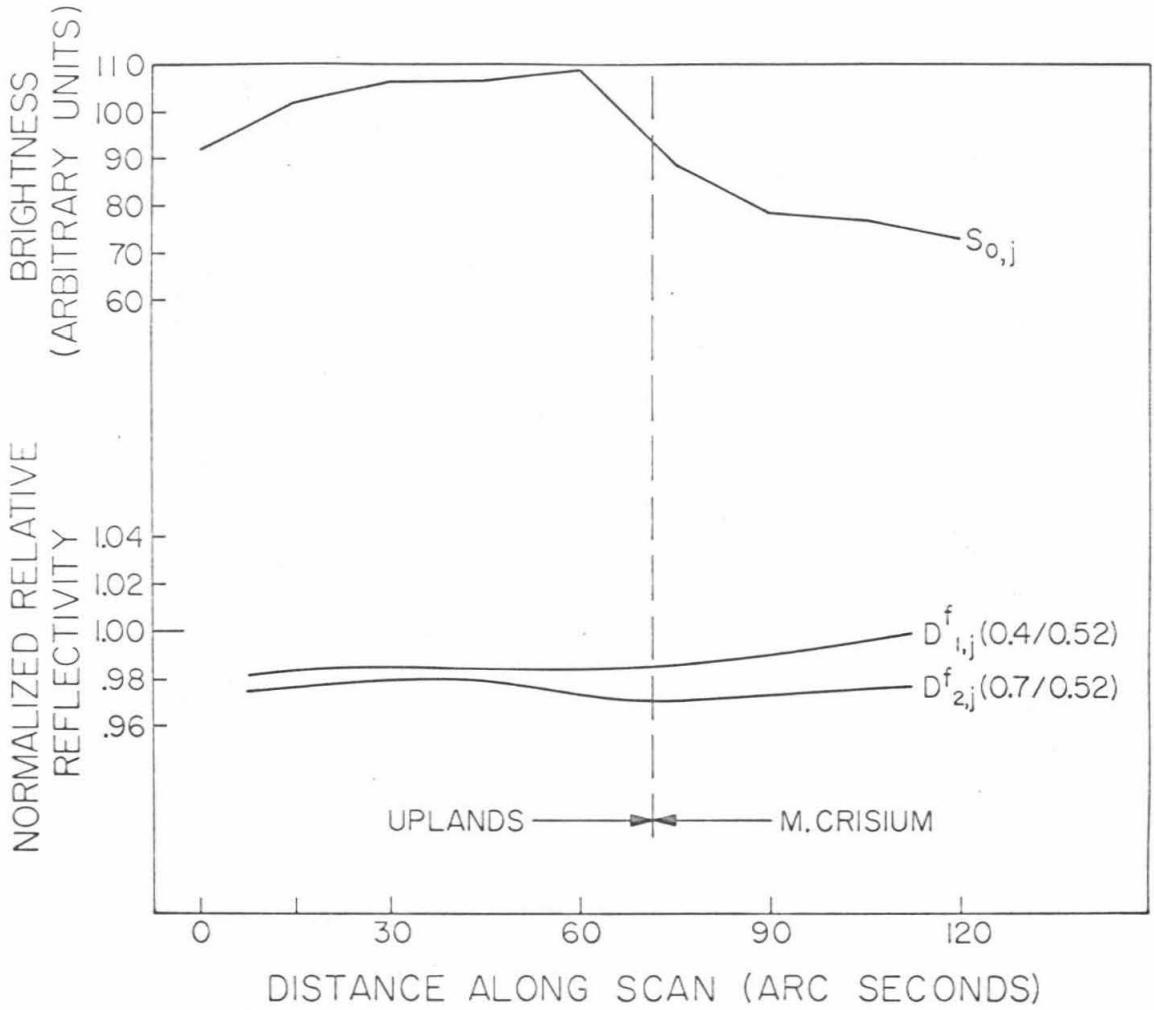


Figure 20. Comparison of albedo ($S_{0,j}$) and normalized spectral reflectance variations across upland - Mare Crisium boundary.

APPENDIX II

A MODEL FOR SMALL-IMPACT EROSION
APPLIED TO THE LUNAR SURFACE

Laurence A. Soderblom

Division of Geological Sciences
California Institute of Technology
Pasadena, California 91109

Submitted to the Journal of Geophysical Research

Publication: May, 1970

Contribution No. 1656 of the Division of Geological Sciences
California Institute of Technology

ABSTRACT

A model for erosion of the lunar surface by impact of small projectiles is developed which provides an analytic representation of the change of crater shape as a function of time. The model is applied to the erosion of craters approximately 1 m to 1 km in diameter. The lifetime of a crater in this size range, which is steadily eroded by impact, is approximately proportional to its radius. The model predicts the observed steady state size frequency distribution of small lunar craters and the dependence of this distribution on the crater production curve.

INTRODUCTION

During recent years knowledge of the distribution of lunar craters has been extended to craters smaller than 10 cm in diameter by Ranger, Orbiter and Surveyor imaging systems. The formation and morphologic evolution of craters smaller than about 1 kilometer are the subjects of this paper. The general form of the observed diameter-frequency relation for craters in the lunar maria is shown in Figure 21. The observed slope of the total cumulative distribution changes from -1.7 ($R \geq 1$ km) to about -3.0 ($10^2 \text{ m} \leq R \leq 1$ km). From observed secondary distributions produced with large lunar craters and nuclear craters and from the observed distribution of large lunar craters, investigators have predicted that the population of secondary craters should exceed that of primary craters for diameters less than about 1 km (Shoemaker, 1965; Brinkmann, 1966). This domination of the total distribution by secondaries below about 1 km diameters is further demonstrated by an extrapolation of the distribution of telescopically observable secondaries to smaller sizes (see Figure 21).

The predicted slope of the population in the range $R < 1$ km is between -3.3 and -4.0 (Shoemaker, 1965; Brinkmann, 1966; Walker, 1966). The discrepancy between the observed and predicted exponents is probably due to the sensitive dependence of the secondary distribution of a single impact on the proximity to that impact. Any prediction of the secondary population over the lunar surface must take into account this effect. In any case the observed and predicted increase in slope ($R \leq 1$ km) provides an insight into the nature of the production of these smaller craters. The observed distribution maintains a steep slope (~ -3.0) down to diameters of a few hundred meters. Below this diameter the observed distribution departs markedly

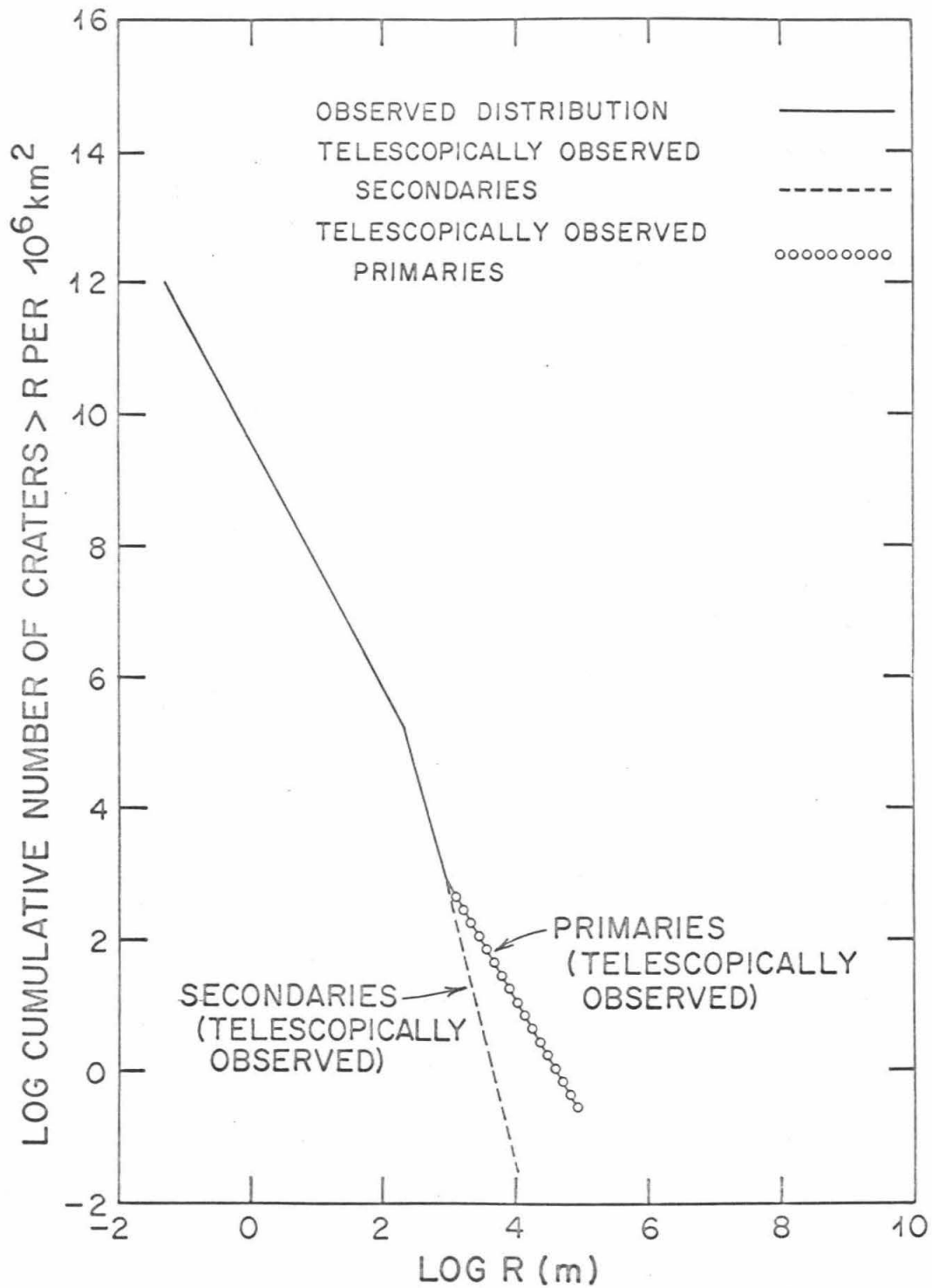


Figure 21. The observed distribution of craters in the lunar maria (after Shoemaker, 1965).

from the predicted distribution as the slope changes to -2.0 . In attempting to explain the scarcity of these smaller craters ($R \leq 10^2$ m) several investigators have concluded that these craters form a steady state population such that craters disappear at the same rate as others are formed (Shoemaker, 1965; Moore, 1965).

The investigation of the mechanism by which craters are destroyed has produced two theories. Marcus (1964) considered the erosion or disruption of topography by impacts producing craters of size comparable with the topography affected. Shoemaker (1965) and Ross (1968) have suggested erosion by small particle bombardment, more accurately: bombardment by meteoroids and secondary lunar fragments producing craters small compared to the topography. The problem considered here is the steady erosion of a surface by repetitive impacts producing individual effects small compared to the topographic scale. It is assumed that the observed distribution in the range 100 m to 1 km represents the crater production curve applicable below 100 m diameters. In this paper the model is to be applied specifically to the erosion of fresh craters with diameters of a few meters to a few hundred meters. Erosion of these craters, as will be shown, is effected primarily by craters in the size range 1 to 100 meters. An analytic solution of morphological change is desirable in order to predict crater frequency distributions in radius and slope as functions of surface age and particle flux.

FORMULATION OF EROSION MODEL

In forming an analytic theory of impact cratering erosion, the basic problem is to mathematically describe the effect of a single impact. Consider first an impact on a level surface which forms a crater of radius R and some

ejecta distribution $F(r)$ (cylindrical coordinates). Experimental evidence indicates that most of the mass is ejected at a nearly constant angle, θ , the angle measured from the surface normal, and that angle is approximately independent of the angle of impact except for cases of grazing incidence which form a small percentage of all impacts (Gault, et al., 1963). It will be assumed that all mass is ejected into a cone of apex angle θ from a ring of radius R . Since it will be demonstrated that the transport of mass by a single impact is an insensitive function of $F(r)$, each of these two assumptions imposes negligible error.

The time of flight of an ejected particle which lands at a distance r is given by

$$(1) \quad t = \left[\frac{2(r-R) \cot \theta}{g} \right]^{1/2}$$

where g is the acceleration due to gravity.

Consider now an impact on a flat surface tilted at angle $\bar{\theta}$. This system can be described in terms of a reduced normal gravity $g \cos \bar{\theta}$ with a horizontal acceleration $g \sin \bar{\theta}$ (Figure 22).

From equation (1) the time of flight is

$$(2) \quad t = \left[\frac{2(r-R) \cot \theta}{g \cos \bar{\theta}} \right]^{1/2}$$

The center of mass of a ring arriving at time t on a horizontal surface is shifted downslope by B on the tilted surface where

$$(3) \quad B = \frac{1}{2} g t^2 \sin \bar{\theta}$$

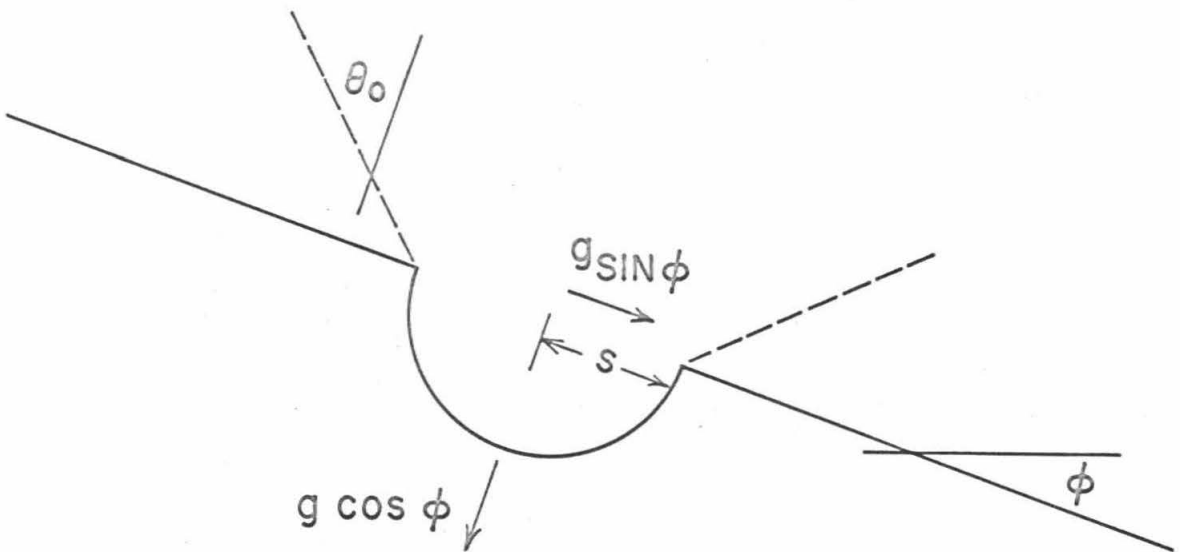


Figure 22. The geometry of the trajectories of material ejected from a crater eroding a surface with slope ϕ .

The displacement, W , of the center of mass of the whole ejecta pattern downslope is then

$$(4) \quad W = \frac{\int_R^\infty F'(r) (r - R) \tan \bar{\phi} \cot \theta 2 \pi \rho r \, dr}{\int_R^\infty F'(r) 2 \pi \rho r \, dr}$$

where $F'(r)$ is the ejecta pattern $F(r)$ under reduced normal gravity, $g \cos \bar{\phi}$, on a level surface. In order to test the sensitivity of W on $F'(r)$ in equation (4), consider an ejecta profile of the form

$$(5) \quad F'(r) = \begin{cases} 0, & r < R \\ \zeta & R < r < \beta R \\ \beta^{-1} & r < \beta R \\ 0, & r < \beta R \end{cases}$$

where ζ and β are the vertical and horizontal dimensions of the ejecta blanket.

Using equation (5) in equation (4) the displacement becomes





$$(6) \quad W = \frac{R}{2} \frac{(\beta + 1)(\beta - 1)}{\beta + 2} \tan \bar{\phi} \cot \theta$$

The dependence of W on β is shown in Table 4. Clearly W is not a sensitive function of $F'(R)$ between the extreme cases shown in Table 4. For craters about a meter or larger in diameter, experimental evidence indicates that most of the ejecta falls within a few crater radii (D.E. Gault, personal communication, 1969). A reasonable choice for β is between 3 and 4.

For geologic materials $\theta \sim 45^\circ$ and equation (6) becomes

$$(7) \quad W \sim R \tan \bar{\phi}$$

Table 4. The dependence of the constant in equation (6) on the form of the ejecta profile or eroding craters.

β	$\frac{(\beta + 1)(\beta - 1)}{2(\beta + 2)}$	PROFILE: $F'(r)$
2	0.4	
3	0.8	
4	1.2	
5	1.7	

A simple differential equation for the steady modification of the surface by random impacts of small bodies may be derived through the use of equation (7). Suppose two relations to exist. The first is

$$(8) \quad Me = C_1 \rho R^3$$

where Me is the mass ejecta; ρ , its density; R , the crater radius; and C_1 , a constant (approximately 1/2). All craters are assumed to have similar initial shapes, which is approximately true for craters of a few kilometers in radius or smaller (Shoemaker, 1965). The second relation is

$$(9) \quad N = \frac{A}{R^\lambda}$$

where N is the cumulative number of craters formed per unit time and area with radius greater than R ; A and λ are constants. From the production curve for smaller craters (diameter $10^2 \text{ m} \leq R \leq 1 \text{ km}$) λ is approximately 3.0 (Morris and Shoemaker, 1969).

Next consider a two-dimensional topography in which the height, h , is a function of only one variable, x . At x_1 and x_2 are two vertical planes separated by Δx . Consider eroding impacts which form craters of radius $R \rightarrow R + dR$. Using equations (7), (8), and (9), the mass moved across the plane at x_1 in Δt is

$$(10) \quad \Delta M_1 = C_1 \rho A \frac{\partial h}{\partial x} \Delta t R^{3-\lambda} dR$$

Here it is assumed that $W \frac{\partial^2 h}{\partial x^2}$ is small compared to $\frac{\partial h}{\partial x}$; that is the slope $\frac{\partial h}{\partial x}$ does not change significantly between x_1 and $x_1 \pm W$. This assumption is valid because, as will be shown, erosion is caused chiefly by

particles forming craters which are smaller than the feature being eroded. Like equation (10), at x_2 we write

$$(11) \quad \Delta M_2 = C_1 \rho A \left[\frac{\partial h}{\partial x} + \frac{\partial^2 h}{\partial x^2} \right] \Delta x \Delta t R^{3-\lambda} dR$$

Integration of equation (10) over R from 0 to some R_{\max} yields

$$(12) \quad M_1 = \frac{C_1 \rho A}{4-\lambda} R_{\max}^{4-\lambda} \Delta t \frac{\partial h}{\partial x}$$

R_{\max} is the upper limit of the distribution of eroding craters whose effects can be meaningfully averaged over the surface. Craters larger than R_{\max} produce catastrophic, isolated effects which do not change the average form of the topography. Further, R_{\max} increases with time as larger craters become more abundant and can be included in the uniform distribution of craters which have saturated the surface. The explicit time dependence of R_{\max} must be determined after integration of equations (13) and (14) since k represents the average rate of erosion for the time interval between $t=0$ and some time at which the solutions are evaluated.

A similar expression for M_2 can be derived from equation (11). From conservation of mass the following simple differential equation for the height is obtained

$$(13) \quad k \frac{\partial^2 h}{\partial x^2} = \frac{\partial h}{\partial t}$$

where

$$(14) \quad k = \frac{C_1 A R_{\max}^{4-\lambda}}{4-\lambda}$$

This equation is common in diffusion problems such as heat flow; the solutions present no difficulty.

For the example and application of this paper we will consider a freshly formed crater as the initial topography. In cylindrical coordinates, assuming radial symmetry, the differential equation becomes

$$(15) \quad k \left\{ \frac{\partial^2 h}{\partial r^2} + \frac{1}{r} \frac{\partial h}{\partial r} \right\} = \frac{\partial h}{\partial t}$$

The initial crater profile is

$$(16) \quad h(r,0) = H(r)$$

Assume that the radius to the crater rim crest does not change, that is

$$(17) \quad \left. \frac{\partial h}{\partial r} \right|_a = 0$$

where a is the radius of the crater being eroded. This particular boundary condition was chosen because the resulting solution is a series of Bessel functions rather than the Fourier-Bessel integral as is the most general solution. With this series it is then easier to note the dependence of time constant on spatial frequency in the solution. Also the series solution contains the characteristic length scale of the problem. In any case, both solutions give the same results as will be evident from the initial form chosen for $H(r)$. Then

$$(18) \quad h(r,t) = \frac{2}{a^2} \int_0^a r' H(r') dr' + \frac{2}{a^2} \sum_{n=1}^{\infty} \exp(-k \alpha_n^2 t/a^2) \frac{J_0(\alpha_n r/a)}{J_0(\alpha_n)} \int_0^a r' H(r') J_0(\alpha_n r'/a) dr'$$

where α_n are the roots of $J_1(\alpha_n) = 0$.

In order to facilitate computation, it is convenient to assume an initial crater profile given by

$$(19) \quad H(r) = \frac{H}{1.4} (1 - J_0(\alpha_1 r/a))$$

which is shown in Figure 3 ($\alpha_1 = 3.83$). This is a logical choice of initial shape because the first root is the longest lived in the solution.

Using equation (19) in equation (18) we have

$$(20) \quad h(r,t) = \frac{H}{1.4} \left\{ 1 - J_0(\alpha_1 r/a) \right\} \exp(-k\alpha_1^2 t/a^2)$$

The maximum slope inside the crater as a function of time is

$$(21) \quad \left. \frac{\partial h}{\partial r} \right|_{\max, t} = \left. \frac{\partial h}{\partial r} \right|_{\max, t=0} \exp(-k\alpha_1^2 t/a^2)$$

Solving equation (21) for t we have

$$(22) \quad t = \frac{a^2}{k\alpha_1^2} \ln \left[\frac{\left. \frac{\partial h}{\partial r} \right|_{\max, t=0}}{\left. \frac{\partial h}{\partial r} \right|_{\max, t}} \right]$$

where t is the time at which the maximum slope inside the crater is

$\left. \frac{\partial h}{\partial r} \right|_{\max, t}$. Note that the explicit time dependence of k has not yet been determined.

Next consider the meaning of R_{\max} in equation (14). R_{\max} is the maximum eroding crater radius considered in the model. Craters smaller than

R_{\max} are so abundant and overlapping that their effect can be considered spatially continuous, whereas craters larger than R_{\max} are distinct and isolated. R_{\max} is taken to be the lower limit of that crater size distribution which just blankets the surface in time t . Assuming that the surface is blanketed when the total crater area is twice the surface area, then

$$(23) \quad \int_{R_{\max}}^{\infty} \frac{A \pi R^2 t}{R^{\lambda+1}} dR = 2$$

or

$$(24) \quad R_{\max} = \frac{\pi A t}{2(\lambda-2)} \frac{1}{\lambda-2}$$

The interval R_{\max} to $3 R_{\max}$ contributes 70% of the total integral of equation (23). Hence, although the definition of R_{\max} is rather arbitrary, R_{\max} itself is insensitive to the value of the integral that is chosen. Using the time dependence of R_{\max} (equation (24)) and the expression defining k (equation (14)), the history of the crater shape can be obtained (See Figure 23). The "lifetime" of a crater, τ , is defined as the time after which the maximum slope in the crater is less than some arbitrary small slope, S_f . Then using equations (14) and (24) in (22) we have

$$(25) \quad \tau = \frac{1}{A} \left[\frac{(4-\lambda) \ln \left(\frac{S_i}{S_f} \right)}{C_1 \alpha_1^2} \right]^{\frac{\lambda-2}{2}} \left\{ \frac{2(\lambda-2)}{\pi} \right\}^{\frac{4-\lambda}{2}} a^{\lambda-2}$$

where S_i is the initial slope, $\partial h / \partial r |_{\max}$, $t=0$. Using the observed slope λ of the crater production curve, the "lifetime" depends on the radius raised

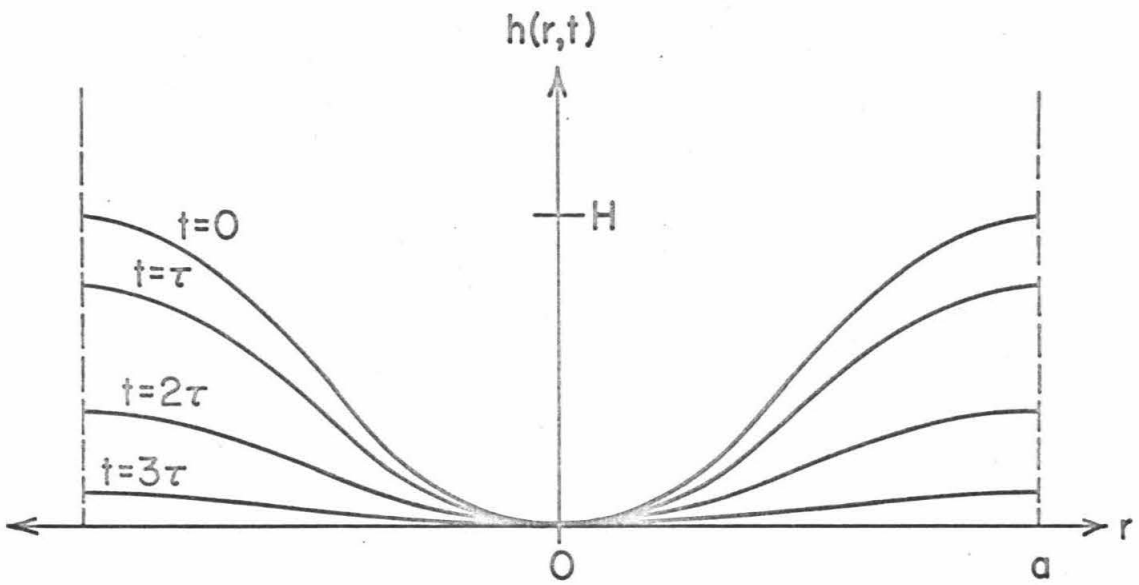


Figure 23. The evolution of the profile of the idealized crater considered in the model. τ is an arbitrary unit of time.

to an exponent between 1.0 and 1.2. Finally we wish to calculate the ratio of R_{\max} to a

$$(26) \quad \frac{R_{\max}}{a} = \left[\frac{(4-\lambda) \pi \ln \left[\frac{S_i}{\left. \frac{\partial h}{\partial r} \right|_{\max, t}} \right]}{C_1 \alpha_1^2 2(\lambda-2)} \right]^{\frac{1}{2}}$$

This relation is plotted as a function of crater slope in Figure 24 over a range of values for C_1 from 0.5 to 1.0 and for λ from -3.0 to -3.2. The intent of Figure 24 is to show that erosion of a crater is a rather continuous process down to slopes of 10° to 15° , a 100m crater being primarily effected by craters smaller than a few tens of meters. Below 10° to 15° the surface becomes mottled and crater shape irregular as erosion by larger craters becomes effective. This effect is obvious on comparing Orbiter photographs taken at low solar incidence angles (ie. $\sim 70^\circ$) with those taken at high incidence (ie. $> 80^\circ$).

Hence, until the slope drops below a few degrees, erosion by impacts producing craters small compared to the topographic scale is more effective than is disruption of topography by large impacts over all sizes for which equation (9) holds.

From equation (9) the steady state distribution for $t > \tau$ is

$$(27) \quad N_c = \int_D^\infty \frac{A \tau \eta^{-(\lambda+1)}}{4} d\eta$$

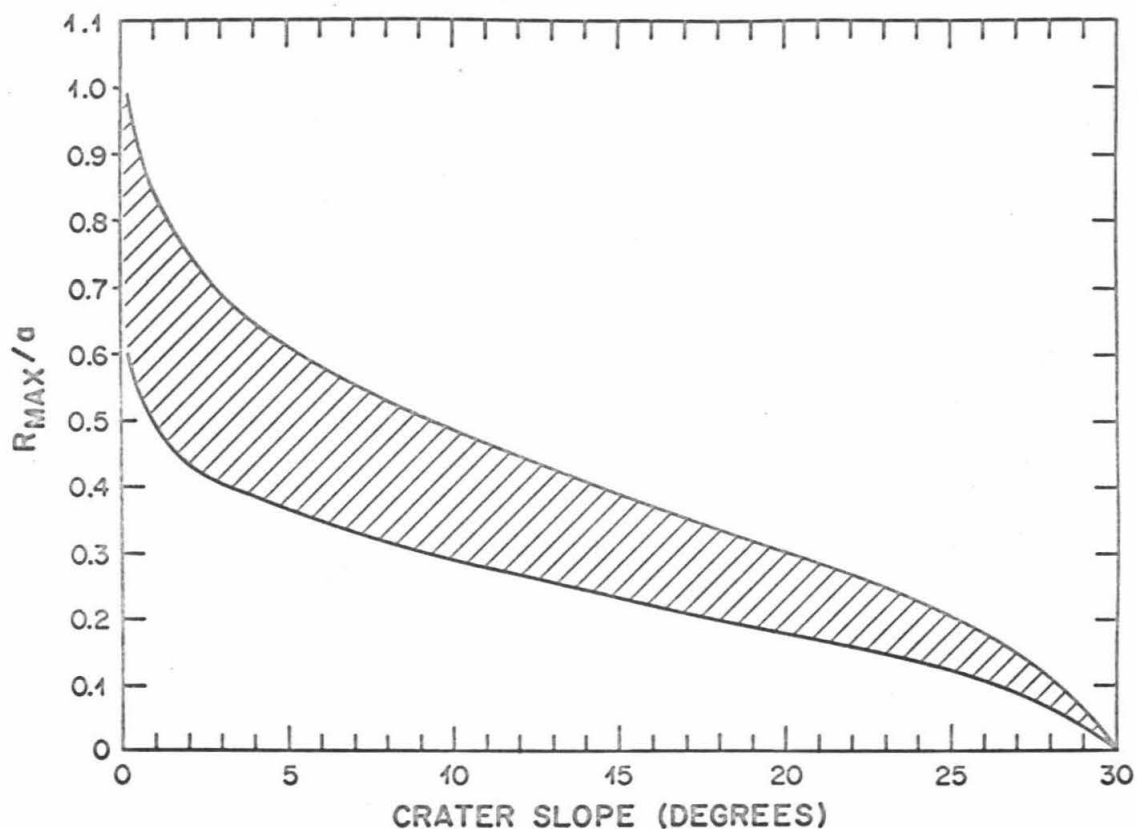


Figure 24. The relation between R_{max} , the maximum radius of craters effecting erosion, and a , the radius of the crater being eroded as a function of the maximum slope inside the eroded crater. The field is plotted over ranges of C_1 between 0.5 and 1 and λ between -3.0 and -3.2. The plot is intended to demonstrate a functional relationship and not a precise numerical prediction since the ratio is very sensitive to the values of C_1 , λ and the erosion rate.

where N_c is the cumulative number of craters per unit area larger than diameter D (η is a dummy variable of integration over diameter). Using equation (25) in equation (27) we finally have

$$(28) \quad N_c = \frac{1}{2} \left[\frac{(4-\lambda) \ln \left(\frac{S_i}{S_f} \right)}{\alpha_1^2 C_1} \right]^{\frac{\lambda-2}{2}} \left[\frac{2(\lambda-2)}{\pi} \right]^{\frac{4-\lambda}{2}} D^{-2}$$

COMPARISON WITH OBSERVED DISTRIBUTIONS

The observed distribution of craters with diameters less than about 10^2 m (Figure 21) is

$$(29) \quad N_o = 10^{10.9} D^{-2}$$

where N_o is the observed cumulative number per 10^6 km² with diameters greater than D (in meters) (Trask, 1965; Morris and Shoemaker, 1969). The observed slope of the power function representing the production of smaller craters (<1 km) is generally between -2.9 and -3.2 (Morris and Shoemaker, 1969). Over this range λ and for S_f between 1° and 5° and C_1 between .5 and 1, equation (28) gives for the steady state distribution

$$(30) \quad N_c = 10^{11.2 \pm 0.2} D^{-2}$$

The observed distribution (equation (29)) was measured from Ranger and Orbiter photographs, and it remains unresolved as to what the lower limit of the slopes of craters included in that observation is. A range of final slope (S_f) between 1° and 5° was used in calculating equation (30) for comparison with observation. The model predicts the relation between the production

rate and the observed steady state distribution. The slope of the steady state distribution is -2 , independent of all other parameters; the constant in the steady state distribution is a function only of the slope of the production curve or transient distribution (100 m to 1 km, Figure 21)

It should be noted that the appropriate slope for the crater production curve for craters smaller than about 10^2 m might be somewhat steeper than the observable production curve of craters with diameters between 10^2 m and 1 km. As was pointed out in the introduction, the predicted secondary population slopes range from -3.3 to -4.0 . For example, a slope of -3.8 yields

$$(31) \quad N_c = 10^{10.5D} D^{-2}$$

As the slope approaches -4.0 the model breaks down because the erosion rate depends on the lower limit of the eroding craters rather than an upper limit (R_{\max}). The observed distribution is probably the most appropriate to use for the crater production curve, and equation (30) is a better prediction of the steady state population than is equation (31).

DISCUSSION

It is important to examine the stability and sensitivity of the model to several assumptions implicit in its development. The definition of R_{\max} is rather arbitrary. It represents that size crater below which craters eroding the surface can be treated as spatially continuous. Craters larger than R_{\max} are discrete and discontinuous and affect only a small percentage of the total area during the time required to erode a crater. Any error arising due to the ambiguity in R_{\max} would be represented by a multiplicative constant in the relation between a and R_{\max} since the relation is linear in the radius of the crater. Hence, the expression for the lifetime, τ , as a function of

radius is only affected by a multiplicative constant and the relative lifetimes of different size craters are unaffected. Due to the uncertainty in A , the determination of absolute lifetimes is not presently possible anyway.

Slumping was not considered in the model although it is probably the dominant eroding process early in a crater's history. However the crater slope remains high for only a small part of its lifetime and the inclusion of slumping would only serve to complicate the model.

It should also be pointed out that the model as it is presented is valid only over the range $2 < \lambda < 4$. When $\lambda < 2$ larger craters effects the topography before smaller ones. That is to say the total area of craters formed greater than any particular diameter is always greater than the total area of those craters smaller than that diameter. Such a distribution with a low slope was likely involved in the formation of the lunar uplands (Gault, 1969). When $\lambda > 4$ the erosion rate is controlled by the lower limit of the distribution of eroding craters. Integration of equation (11) must then be from some minimum radius, R_{\min} , to ∞ . Thus when $\lambda > 4$, k is independent of R_{\min} since the same R_{\min} would apply to all craters. The predicted slope of the steady state distribution would then be $2 - \lambda$.

Erosion for a λ typical of the lunar maria is effected primarily by craters between $.1 R_{\max}$ and R_{\max} . Although the number of impacting masses per unit size range increases with decreasing mass, the eroding power or mass flux, decreases faster with decreasing mass. This is important because we then need only to require that the power function for crater production hold over a limited range.

The lifetime, τ , of a crater was calculated assuming a constant meteoritic flux during its erosion. This may not be a realistic assumption,

particularly for craters formed shortly after accretion during which the flux was probably rapidly decreasing. The model is still valid if τ is thought of as the integrated flux that has fallen on the surface since the formation of the crater. Thus the time scale used in the model is distorted by the flux history. As absolute crystallization ages become available from the Apollo samples it will be possible to obtain the flux history using this erosion model. That subject will be considered in detail in a future paper.

SUMMARY

The model presented here is an idealization of erosion of a radially symmetric crater formed in a flat level topography. It is also possible to apply the differential equation governing mass transport to other kinds of topographic features such as rilles, ridges, and domes and to examine the evolution of their morphologies with time. In the case of the radially symmetric crater, the morphology approaches the form of the Bessel function J_0 as it is smoothed by the erosion process. The erosion model developed here applies to craters a few meters to a few hundred meters in diameter as they are fairly uniform in initial shape, that is: few flat floors, as shown by Ranger photography (Shoemaker, 1965).

Finally, it is important to point out that the model predicts the continuous distribution of morphologies from sharp fresh craters to smooth and shallow craters, and it may not be necessary to invoke different mechanisms of crater formation in order to explain the various morphologies of the bulk of the craters.

ACKNOWLEDGMENT

The author wishes to thank Dr. Eugene M. Shoemaker for initially suggesting the problem and for valuable discussion concerning the nature of the process. The work was completed under NASA Grant NGL-05-002-003.

REFERENCES

- Brinkmann, R. T., Lunar crater distributions from Ranger 7 photographs, *J. Geophys. Res.*, 71, 340, 1966.
- Gault, D. E., Saturation and equilibrium conditions for impact cratering on the Lunar surface: Criteria and implications, *URSI Journal Radio Science* (in press), 1969.
- _____, E. M. Shoemaker and H. J. Moore, Spray ejected from the Lunar surface by meteoroid impact, NASA Rpt. TND-1767, 1963.
- Marcus, A. H., A stochastic model of the formation and survival of Lunar craters. I. Distribution of clean craters, *Icarus*, 3, 460, 1964.
- Moore, H. J., Density of small craters on the Lunar surface, United States Geological Survey, Astrogeological Studies Annual Progress Report, August 25, 1962 to July 1, 1963, pt. D (1964), pp. 34-51.
- Morris, E. C. and E. M. Shoemaker, Television observations: Craters, in Surveyor Program Results, NASA, Washington, 1969.
- Ross, H. P., A simplified mathematical model for Lunar crater erosion, *J. Geophys. Res.*, 73, 1343, 1968.
- Shoemaker, E. M., Preliminary analysis of the fine structure of the Lunar surface in mare cognitum, in the Nature of the Lunar Surface, pp. 23-78, The Johns Hopkins Press, Baltimore, 1965.
- Trask, N. J., Size and spatial distribution of craters estimated from Ranger photographs. Ranger VIII and IX. Part II: Experimenters' analyses and interpretations, Tech. Rept. 32-800, Jet Propulsion Laboratory, Pasadena, California, pp. 249-338, Mar. 15, 1966.
- Walker, E. H., Statistics of crater accumulation on a surface exposed to a distribution of impacting bodies, SP1 Rept. 46603, Univ. of Miami, Coral Gables, Florida.

APPENDIX III

A TECHNIQUE FOR OBTAINING RELATIVE AGES
FOR REGIONS OF THE LUNAR SURFACE

INTRODUCTION

The development of techniques employing lunar photography to establish relative ages is paramount to understanding the geologic history of the lunar surface. The crystallization ages obtained from Apollo lunar samples provide absolute calibration for such relative age dating methods. It is then possible to obtain absolute ages for many lunar regions and features. The technique used here to obtain relative age is based on a determination of the total accumulation of craters on an initially flat and featureless surface. Relative ages obtained with this method, coupled with absolute age measurements of Apollo lunar samples, can be used to establish the meteorite flux history in the earth-moon environment and to determine absolute ages for many lunar regions and features.

The continued accumulation of impacts on a surface produces a changing distribution of craters which at any time reflects the integrated flux of all projectiles striking that surface since it was featureless. The production of craters with diameters less than about 1 kilometer can be represented by

$$(1) \quad N = AD^\lambda$$

where N is the cumulative number of craters formed per unit time area with diameters greater than D ; A and λ are constants. The slope of the production curve (λ) is between -2.9 and -3.2 (Shoemaker, et al., 1969). Initially the distribution of craters formed on a surface has the same slope as the production curve. As time elapses, craters smaller than some specific diameter reach steady state; that is, these craters are destroyed as fast as

they are generated. The paper in Appendix II (hereafter referred to as Paper 1) was concerned with the relation between steady state and production curves. The time history of the overall distribution as predicted in Paper 1 is shown in Figure 25. Also shown in that figure is the size-frequency distribution for the Surveyor VI landing site (Shoemaker, et al., 1969). As might be expected, the steady state portions of distributions at all sites lie along the same curve, which has the form

$$(2) \quad N_{ss} = 10^{10.9} D^{-2.0}$$

where N_{ss} is the cumulative number per 10^6 km^2 and D is measured in meters. This distribution was first documented by Trask (1965) and has been found to persist at all Surveyor landing sites down to crater diameters of less than a meter (Shoemaker, et al., 1969).

The diameter of the largest size crater in steady state (C_s) gives a measure of the relative age of the surface. To determine that point by simply counting craters is at best difficult. Laborious counting over large areas is required to obtain adequate statistics. Furthermore, the distribution in any region may be quite irregular due to swarms of secondaries; thus a local region may not accurately reflect the idealized distribution depicted in Figure 25. Any technique that depends on the statistics of craters with diameters greater than C_s suffers because of this randomness.

A second technique used to measure relative age is based on a determination of the regolith thickness (Oberbeck and Quaide, 1968; Shoemaker, 1970). Shoemaker (1970) has mathematically related this thickness to the accumulated crater population and to C_s . This method suffers from difficulties in that (1) relatively high resolution photographs (resolution of the order of a

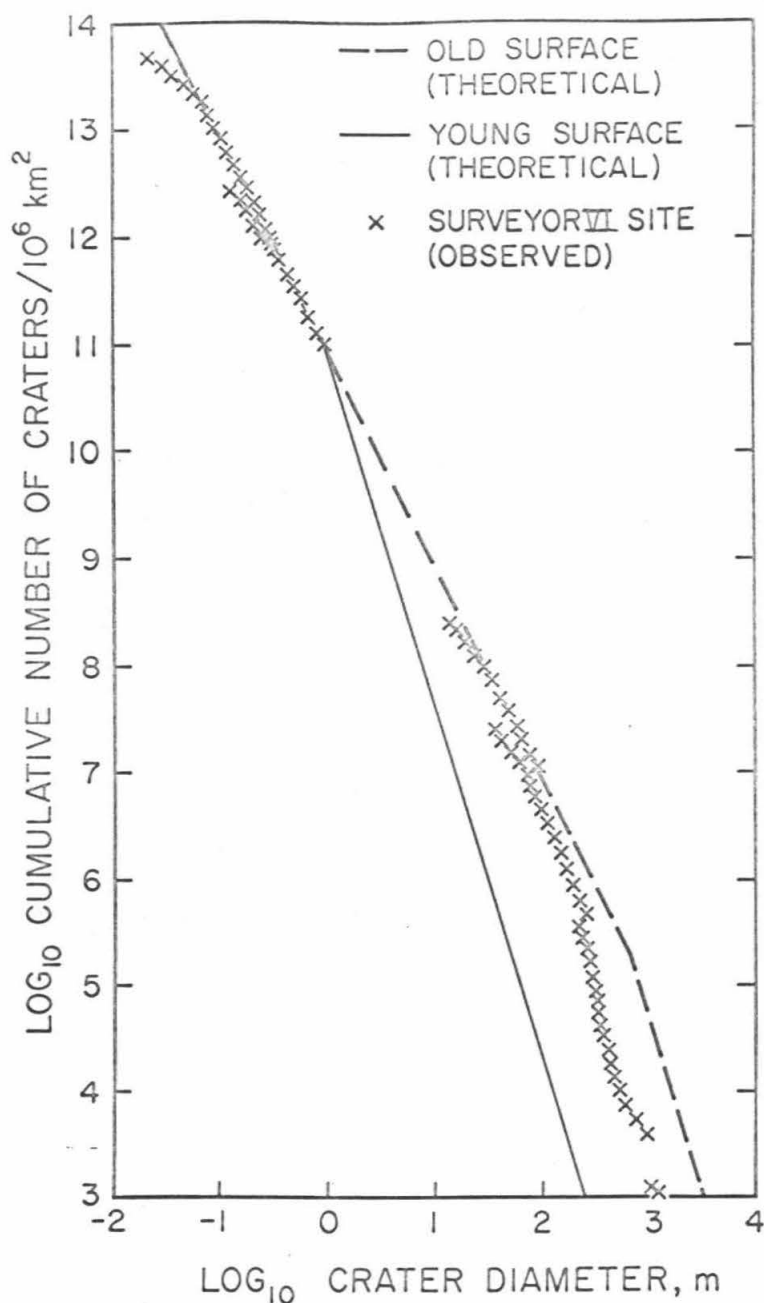


Figure 25. Comparison of observed and predicted size-frequency distributions of lunar craters. The size-frequency distributions of craters on surfaces of arbitrary age, as derived from the erosion model, are compared with the size-frequency distribution of craters at the Surveyor VI site determined by Shoemaker, et al. (1969).

meter) are required to estimate the regolith thickness, (2) the thickness of the debris layer is far from uniform and many measurements within a single area are necessary to establish the mean thickness, and, (3) the method is affected by local variations in the competence of different strata such as thin volcanic flows, ash flows, and other blankets which might be misinterpreted as a regolith layers.

The method presented here is not affected by random variations in the distribution of large craters (diameters greater than C_s); thus it can be applied to small areas (of the order of 1000 km^2). The method involves a minimum of time and labor and does not require high resolution photography as do measurements of regolith thickness.

METHOD

The technique described here depends on the shape of large craters (diameters near C_s). The change of shape as shown in Paper 1 is effected by impacts which produce craters that are small compared to the crater being eroded. During the period of time in which a crater is eroded, the number of small eroding craters formed becomes so great that random statistical variations in their distribution are averaged out. The shape of a large crater is therefore a very sensitive indicator of the total number of small impacts that have occurred on the surface since the crater was formed.

The shape of a crater can be parameterized by its maximum interior slope. The slope-frequency distributions for three arbitrary crater diameter ($0.8 D$, D , and $1.2 D$) shown in Figure 26 are calculated from the model in Paper 1 for some time, t , since the surface was featureless. In principle, it is possible to obtain the surface age by measuring any one of the

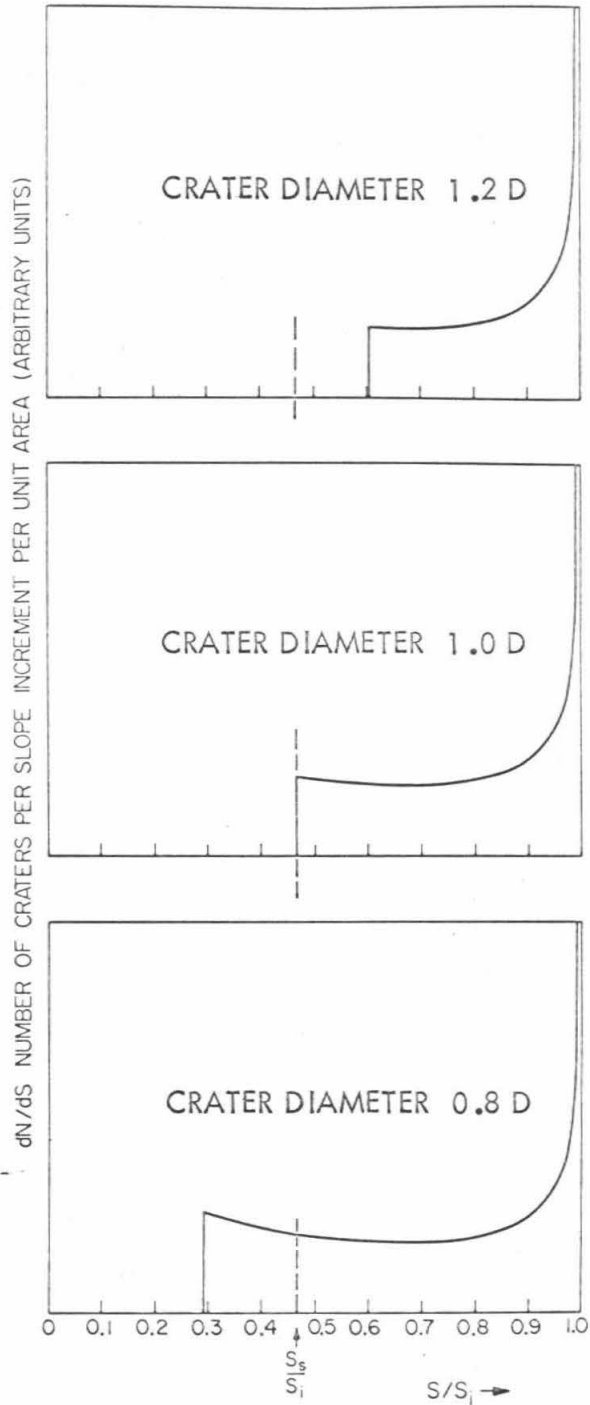


Figure 26. Frequency of craters as a function of the slope of the crater wall. The slope-frequency distributions of crater walls is shown for craters of three arbitrary diameters as predicted by the erosion model.

distributions shown in Figure 26. The age of the surface is just the time required to erode a crater of a given radius to the slope which terminates the slope-frequency distribution of craters of that radius. From the model in Paper 1 the relative age, τ , is then

$$(3) \quad \tau = C \ln^{1/2} (S_i/S_t) D$$

where C is an arbitrary constant; S_i is the initial crater slope ($\sim \tan 30^\circ$); D is the crater diameter; and S_t is the termination slope.

The determination of relative age directly from these slope-frequency distributions is not practical since sufficiently precise measurements of slope, using standard photoclinometric techniques, are not possible. However, the crater size (D_s) whose slope-frequency distribution is terminated at a slope equal to the elevation of the sun above the horizon (S_s) is directly measurable from photography. The slope-frequency distribution for craters of diameter D in Figure 26 is drawn so its termination slope is equal to the sun elevation angle, S_s . All craters larger than D_s have shadowed interiors. From equation (3) the relative age of the surface is

$$(4) \quad \tau = C \ln^{1/2} (S_i/S_s) D_s$$

In practice, the most precise way to determine D_s photographically is to first measure the ratio of unshadowed to shadowed craters as a function of diameter. The ratio is zero for craters larger than D_s . The form of such a ratio-diameter relation as predicted from the erosion model of Paper 1 and shown in Figure 27 is given by

$$\begin{aligned}
 P &= 0, D > D_s \\
 (5) \quad P &= \frac{D_s}{D} - 1, C_s < D < D_s \\
 P &= \frac{D_s}{C_s} - 1, D < C_s
 \end{aligned}$$

where P is the ratio of unshadowed to shadowed craters and C_s is the diameter of the largest size crater in steady state. The constant value of P for $D < C_s$ is dependent on the photo quality since C_s is controlled by the lower limit of slope at which a crater is recognizable. Although over the range of crater diameter between C_s and D_s the observed ratio may not precisely fit the predicted ratio because of random statistical variations, the diameter above which P is zero remains D_s .

Equation (3) and (4) contain the implicit assumption that the meteorite flux has remained constant throughout time. The flux probably has not been constant, however, and the time scales used in equation (3) and (4) are likely distorted by the flux history. The concept of time can be removed if τ is thought of as the integrated flux fallen on the surface. In order to avoid these conceptual problems and to provide a standard for comparison "ages" are stated in terms of the size of crater, D_L , which would be eroded below some small slope, S_f , in the lifetime of the surface. D_L is given by

$$(6) \quad D_L = \frac{\ln^{1/2}(S_i/S_s)}{\ln^{1/2}(S_i/S_f)} D_s$$

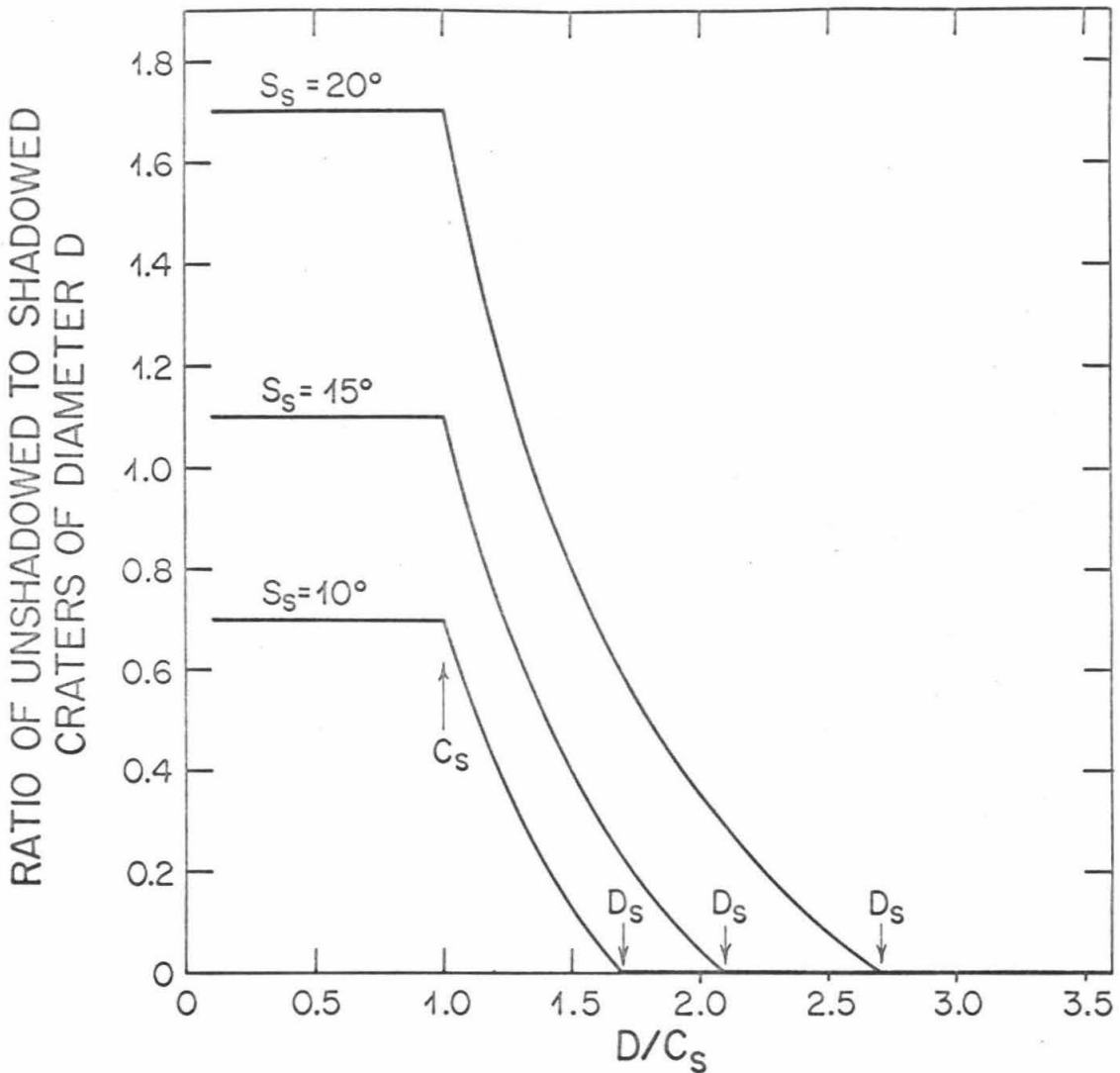


Figure 27. The ratio of unshadowed to shadowed craters as a function of crater diameter, as calculated from the erosion model. This ratio, P , is shown for three solar elevation angles, S_s . D_s is the diameter of the largest unshadowed crater and increases with increasing S_s . C_s is the upper limit of diameter of craters in steady state. It was assumed that C_s does not vary with solar elevation angle.

In applying the method outlined above it is necessary to develop consistent criteria to measure the distribution depicted in Figure 27. Paramount to this is the photographic definition of a shadow. The most consistent definition is that a crater is unshadowed when features (slump marks, fractures, craterlets) are visible in the nearly shaded portion of the wall. This definition overcomes most ambiguity in classifying an individual crater

It was found that a rapid visual evaluation of a photograph could be used to obtain D_s with nearly the same accuracy as obtained by fully defining the distribution shown in Figure 27. This technique involves looking for the largest clearly unshadowed craters as a lower limit for D_s and the largest crater whose shadow profile has just disappeared as the upper limit. It is necessary to avoid anomalous depressions which may have initially had low slopes. This difficulty can be avoided if one tests that the unshadowed craters smaller than the "largest unshadowed crater" become rapidly and increasingly more abundant with decreasing size. A determination of D_s by this technique has an uncertainty of about 10% based on the variation between measurements of different observers and from comparison with calculations made from observations which define the complete P vs D relation shown in Figure 27.

VALIDATION

The technique requires confirmation that (1) age determinations for one area made from different photographs with different solar incidence angles must give the same value for D_L ; (2) the measured relation between P and D must on the average approach the predicted curve of Figure 27; and, (3) age measurements for different regions formed at the same time must agree

irrespective of local random variations in the size-frequency distributions.

Table 5 lists the relative ages determined for several lunar sites. The size of crater eroded below 4° in the age of the surface was determined for each site from two different photographs taken at different solar illumination angles. Comparison of the different measurements for each site shows that although the measured values of D_s and S_s differ, the calculated values for D_L remain constant.

Table 5. Comparison Of Determinations Of Relative Ages Of Individual Surfaces From Different Photographs

Region	Orbiter Site and Frame	S_s	D_L
Oceanus Procellarum (250 kilometers east of Surveyor 1)	{ V 27a M111 III P7a M86	18°	175 ± 30
		13°	160 ± 20
Oceanus Procellarum (NE corner of III P10 M170)	{ III P10 170 III S25 M161	12°	300 ± 80
		18°	330 ± 70
Sinus Medii (North of NW-SE Mare Ridge)	{ V 42a M171 III P11 M174	15°	160 ± 20
		21°	170 ± 20

Figure 28 compares the predicted and observed relations between P and D for one site measured at two different solar illumination angles. The shaded areas represent the regions of acceptable fit of the theoretical functions to the data. The slope-frequency distributions predicted from the erosion model are in good agreement with those observed.

In order to apply the third test mentioned above, it is necessary to locate different areas which are likely to be the same age. From the relative visible reflectivity data of McCord, Johnson, and Kieffer, (1969) three areas (II P 13, III P 11, and Surveyor 1) were selected for comparison

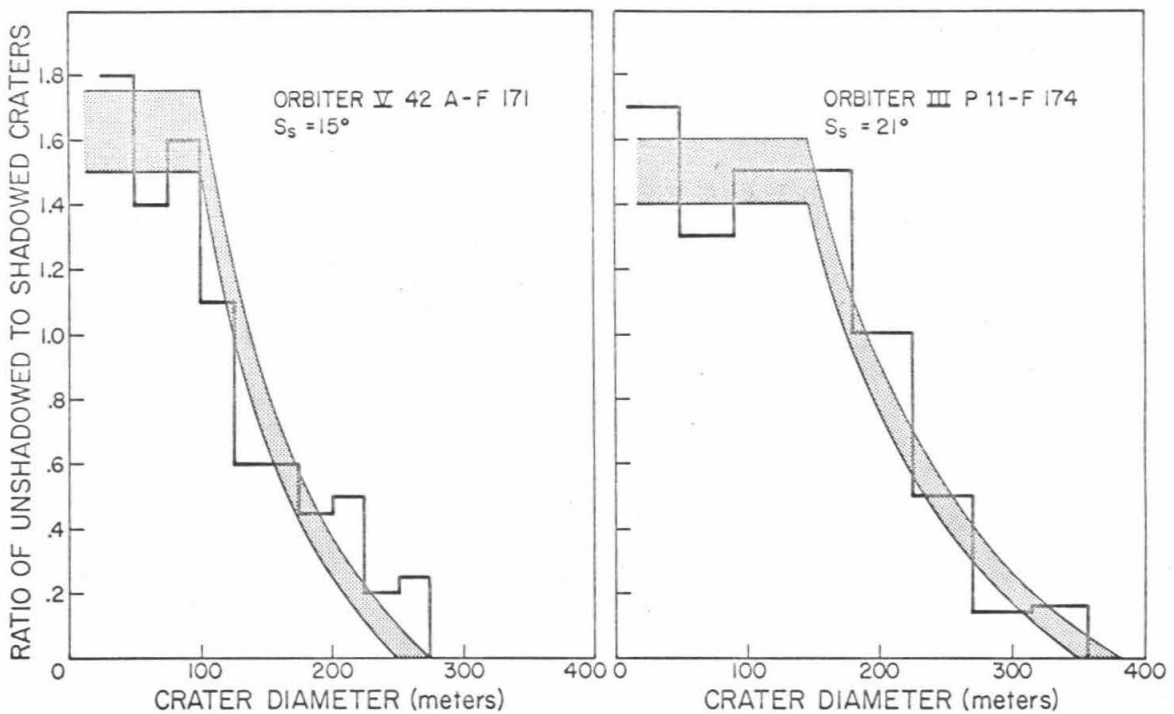


Figure 28. Comparison of the observed and predicted ratio of unshadowed to shadowed craters as a function of crater diameter. The Orbiter frames, V 42 A-F 171 and III P 11-F 174, cover the same area in Oceanus Procellarum but were taken at different solar elevation angles, S_s . The shaded areas represent the regions of acceptable fit of the theoretical model to the data. Notice that the steady state upper limit of diameter, C_s , varies with sun angle.

because (1) the spectral reflectivity curves are nearly identical, (2) they are in the same general province (Southern Oceanus Procellarum), and, (3) there are no significant albedo or morphological boundaries between them. On these criteria there is some basis for presuming these sites to be of the same age. Furthermore, site II P 13 is riddled with a large number of Keplerian secondaries and affords a good opportunity to test the effect of irregular distributions of large craters ($D \sim D_s$) on the technique. The relative ages measured at each of these three sites are compared in Table 6.

Table 6. Comparison Of Relative Ages Determined For Various Areas In Oceanus Procellarum.

Orbiter Site	Region	D_L
II P 13	Oceanus Procellarum	160 ± 30
	200 Kilometers North of Surveyor I	170 ± 30
III P 11	Oceanus Procellarum	160 ± 20
	250 Kilometers East of Surveyor I	170 ± 20
Surveyor I	South Central	160 ± 30
	Oceanus Procellarum	140 ± 20
		150 ± 20

The erosion model, on which the dating technique is based, includes only the process of material transport by impacts producing individual effects which are small compared to the feature being eroded. When the crater is steeper than 20° to 25° , other processes such as slumping are most certainly more effective erosive mechanisms. Processes such as blanketing by ejecta from large nearby craters and crater overlap are more important for slopes less than 5° to 10° . Therefore the technique is only valid for a range of solar incidence between about 10° and 20° . The dominance of the erosion

process described in the model in Paper 1 in the crater slope range of 10° to 20° is well documented by observation. First, the model predicts the relation between the observed production and steady state size-frequency distributions. Second, the observed slope-frequency distribution of craters is predicted by the erosion model (Figure 28). Third, well formed craterlets are visible on the walls of craters in this slope range; and therefore, slumping does not play an important role in the erosion of craters in this range (10° to 20°). Fourth, the total area of craters with slopes greater than 10° is only a few percent of the total surface area. Hence crater overlap and ejecta blanketing by craters of size similar to that being eroded are not dominant mechanisms over the 10° to 20° slope range.

LIMITATIONS AND ERRORS

There are primarily two sources of error. These arise from topographic irregularities of the original surface and from variations in the dynamic range, contrast, and density in the available Orbiter photography.

It was assumed in developing the method that the original surface upon which craters began to accumulate was initially flat and featureless. This is usually valid for surfaces formed by flows or blankets which were thick enough to obscure any topography of original surface on which they were deposited. When deposits were too thin to conceal pre-existing topography, craters larger than a certain size are visible as shallow depressions which become steeper and fresher in appearance with increasing size. If care is not exercised to recognize such surfaces, D_5 may be overestimated by a large amount. These areas can be identified visually since the crater populations consist of two diameter-ranges of predominantly unshadowed craters separated by a diameter-range in which unshadowed craters are

scarce. Such regions can also be recognized from bumps and irregularities which appear in P versus D relations which appear at diameters greater than D_s .

The second kind of surface which violates the assumption of "an initially flat and featureless surface" is the ejecta blanket. These surfaces are typically rubbly and hummocky. To model the development of the distribution of small craters on such a blanket is a very difficult task. Craters will generally last for shorter periods of such surfaces. A reasonable estimate of the relative age can be made for blankets whose typical roughness wavelength is large compared to D_s . Care must be taken to measure distributions only on the flatter portions of the blanket and to avoid steep portions. Such measurements give an upper limit for D_L since craters tend to disappear more rapidly than they would on an initially flat surface.

Young craters such as Copernicus and Tycho are datable by this technique. Older ejecta blankets such as the ejecta from the formation of the Imbrium basin (Fra Mauro Formation) cannot be dated since D_s exceeds their typical roughness wavelengths.

The second source of error arises from nonuniformities in the processing of the Orbiter photography. An extreme example of this effect can be seen in comparing Orbiter V 11a frame M55 with Orbiter III P1 frame M5. The first of these was photographed with a solar incidence angle (above the horizon) of 22° . Numerous craters in this frame appear to be flat bottomed with a portion of the crater walls shaded. In the second of these photographs in which the solar elevation angle is only 14° , these same craters appear shallow, smooth, and unshadowed. This peculiarity arises because the range

of insolation variation in Orbiter Vlla frame M55 exceeds the dynamic range of the photograph. Thus brightness levels below a certain value appear black or shaded. An effect which is this extreme is rare. It is extremely difficult to distinguish this artificially induced morphology from that of craters which are actually flat-bottomed. The only foolproof method of avoiding large errors in the determination of relative age is to reject such photographs which show an inordinant number of flat-bottomed craters.

SUMMARY

The technique presented here can be used to determine D_L , the largest crater that can be continuously eroded below the limit of recognizability in the age of the surface to an accuracy of about 10%. The advantages of the technique are: (1) the determined value of D_L is independent of the illumination angle, (2) the measurement is independent of statistical variations in the population of craters with diameters near to or larger than D_L and, (3) the application of the method is neither time consuming nor laborious allowing one observer to make a large number of precise measurements in a short period of time. It should finally be noted that D_L is a nearly linear function of the integrated flux fallen on a surface. Thus, in the case of constant flux, D_L is linear with the absolute surface age.

APPENDIX IV

RELATIVE AGE DATA

This appendix contains a list of the data used to calculate the relative ages of a number of regions on the lunar surface. Measurements were made from Orbiter III and Orbiter V photographs. D_s is the diameter in meters of a crater which would be eroded from an initial maximum interior slope of 30° to a slope equal to the elevation angle of the sun (S_s) in the lifetime of the surface. $\cos S_s$ is the incidence angle of the solar illumination angle measured from the zenith. D_L is the calculated diameter in meters of a crater which would be eroded to a slope of 4° in the time equal to the age of the surface.

Lunar Orbiter Site and Frame	Lunar Area	Comments	D _s (meters)	CoSs	D _L (meters)
III P 1 M5	S E Tranquillitatis		800-980	76.8°	560 ± 40
III P 1 M13	S E Tranquillitatis		760-1050	75.6°	560 ± 90
III P 1 M19	S E Tranquillitatis		750-950	74.7°	520 ± 60
III S13 M85	Murchison Floor	Oblique photograph	350-570	77.9°	320 ± 80
III P7a M86	Sinus Medii	North of ridge	210-280	77.3°	160 ± 20
III S14 M102	Sinus Aestuum	Oblique photograph	370-560	81.3°	360 ± 70
III S15 M106	W Sinus Medii		505-670	75.1°	360 ± 50
III S16 M107	Mosting Ejecta		300-390	72.4°	180 ± 20
III S18 M112	S W Sinus Medii	Areas too small	> 725	71.5°	> 350
III S18 H113	S W Sinus Medii	Small crater	10-20m	71.3°	8 ± 3
III S18 M115	S W Sinus Medii	Area too small	> 800	71.0°	> 370
III PB M124	E. Procellarum		550-620	72.8°	320 ± 20
III P9a M137	Apollo 12 site		570-790	70.8°	340 ± 60
III P9b M145	Apollo 12 site		660-900	68.8°	350 ± 60
III P10 M163	Procellarum		180-260	79.4°	160 ± 30
III P10 M170	Procellarum	S W Corner	210-290	78.4°	170 ± 30
III P10 M 170	Procellarum	N E Corner	320-530	78.4°	300 ± 80

Lunar Orbiter Site and Frame	Lunar Area	Comments	D_s (meters)	CoS_s	D_L (meters)
III P 11 M173	S C Procellarum		350-400	68.8°	170 ± 20
III P 12b 2 M181	S C Procellarum		240-330	73.3°	160 ± 30
III P 12b 1 M201	S C Procellarum		270-360	69.8°	150 ± 20
III P 12a M 185	S C Procellarum		220-280	72.7°	140 ± 20
III P 12c M 205	S C Procellarum		260-340	69.3°	140 ± 20
III S 31 M215	Hevelius	{ Upper limit from Orbiter IV-F 162	> 1300	84.3°	1300 ± 100
III P 25 M 161	S C Procellarum		500-750	72.1°	330 ± 70
V-1 M33	Petavious		1000-1500	71.9°	600 ± 130
V-2 M37	S Fecunditatis		1060-1500	70.8°	630 ± 100
V-5.1 M41	Fecunditatis		900-1300	72.5°	610 ± 100
V-8a M44	W Fecunditatis		840-1210	68.8°	470 ± 70
V-9.1 M52	S E Tranquillitatis		750-1100	72.5°	490 ± 100
V-11a M55	S E Tranquillitatis		850-1190	69.2°	460 ± 80
V-13 M64	Apollo II		650-1050	73.4°	470 ± 100
V-14 M68	Littrow		850-1280	68.8°	470 ± 70
V-14 M68	M Serenitatis		300-500	70.0°	185 ± 45

Lunar Orbiter Site and Frame	Lunar Area	Comments	D (meters)		CoSs	D (meters)	
			s	L		s	L
V-15.1 H70	Dawes		100-150	55 ± 5	69.5°	100-150	55 ± 5
V-16 M74	Apollo 11		825-1000	430 ± 40	70.0°	825-1000	430 ± 40
V-18 H80	Dianysius		90-110	45 ± 5	69.3°	90-110	45 ± 5
V-18 M80	S W Tranquillitatis		780-950	410 ± 40	69.3°	780-950	410 ± 40
V-21 M86	N Serenitatis		610-770	350 ± 40	71.4°	610-770	350 ± 40
V-22 M93	S Serenitatis	S W Corner	1000-1400	200 ± 50	70.7°	1000-1400	200 ± 50
V-23.1 M94	M Vaporum		430-640	310 ± 50	71.6°	430-640	310 ± 50
V-25 H102	Alpine Valley		360-570	310 ± 50	77.8°	360-570	310 ± 50
V-25 H102	M Imbrium		330-500	300 ± 60	78.8°	330-500	300 ± 60
V-26 M106	Palus Putredinis	Old Area	600-1000	400 ± 10	71.5°	600-1000	400 ± 10
V-26 M105	Palus Putredinis	Young Area	220-440	180 ± 60	73.0°	220-440	180 ± 60
V-27 M108	Sinus Medii	South of Ridge	510-680	320 ± 50	72.2°	510-680	320 ± 50
V-27a M111	Sinus Medii	North of Ridge	260-400	175 ± 30	72.1°	260-400	175 ± 30
V-28 M119	Alphonsus	Rough Area	690-920	800 ± 100	72.9°	690-920	800 ± 100
V-28 M 119	Procellarum		360-450	230 ± 30	74.4°	360-450	230 ± 30
V-29 M 120	N E Aestuum		350-440	200 ± 30	72.0°	350-440	200 ± 30
V-30 H 128	Tycho	Playa	< 25	< 20	80.7°	< 25	< 20

Lunar Orbiter Site and Frame	Lunar Area	Comments	D (meters)		CoSs
			s	L	
V-31 M129	N Imbrium		410-610	280 ± 50	73.0°
V-32 M133	Sinus Aestuum	Confused by Ejecta	360-550	240 ± 50	72.0°
V-32 H133-136	Eratothenes		190-280	120 ± 20	72.0°
V-33 M137	S W Sinus Aestuum		330-490	210 ± 40	71.5°
V-34 M138	Fra Maura	Crater Floor	638-810	420 ± 50	74.0°
V-35 M145	S Imbrium		470-660	300 ± 50	72.0°
V-36 M146	Copernicus		130-180	80 ± 20	72.5°
V-38 M159	Imbrium		280-350	170 ± 20	72.7°
V-40 M 164	N E Procellarum		280-380	180 ± 30	73.0°
V-41 M168	S Humorum		220-370	220 ± 60	80.4°
V-42a M169	Apollo 4		250-275	160 ± 20	75.2°
V-43.2 M177	N Humorum		280-400	220 ± 60	77.0°
V-45.1 M182	N Procellarum		290-440	210 ± 50	74.6°
V-46 M193	N E of Aristarchus		250-375	175 ± 30	73.9°
V-46 M193	N E of Aristarchus		330-450	210 ± 40	72.9°
V-48 M201	Aristarchus		60-90	45 ± 10	73.0°
V-50 M209	Procellarum	N W Corner	200-300	165 ± 40	74.9°
V-50 M209	Procellarum	West Side	310-440	250 ± 40	74.9°
V-51 M215	Procellarum		200-300	150 ± 30	75.0°

LIST OF REFERENCES

- Adams, J.B., "Lunar and Martian Surfaces: Petrological Significance of Absorption Bands in the Near-Infrared," *Science*, 159, 1453, (1968).
- Adams, J.B., "Spectral Reflectivity of Lunar Samples," *Science*, 167, 737, (1970).
- Adams, J.B. and A. L. Filice, "Spectral Reflectance 0.4 to 2.0 Microns of Silicate Powders," *J. Geophys. Res.*, 72, 5705, (1967).
- Albee, A.L., D.S. Burnett, A.A. Chodos, O.J. Eugster, J.C. Huneke, D.A. Papanastassion, F.A. Podosek, G. Price Russ II, H.G. Sanz, F. Tera and G.J. Wasserberg, "Ages, Irradiation History, and Chemical Composition of Lunar Rocks from the Sea of Tranquillity," *Science*, 167, 463, (1970).
- Gault, D.E., E.M. Shoemaker and H. J. Moore, "Spray Ejected from the Lunar Surface by Meteoroid Impact," NASA Report TND-1767, (1963).
- Goetz, A.F.H., "Differential Infrared Lunar Emission Spectroscopy," *J. Geophys. Res.*, 73, 1455, (1968).
- Goetz, A.F.H. and L.A. Soderblom, "Differences Between Proposed Apollo Sites: 3. Far Infrared Emissivity Evidence," *J. Geophys. Res.*, 74, 4389, (1969).
- Gold, Thomas, M. J. Campbell and B.T. O'Leary, "Optical and High-Frequency Electrical Properties of the Lunar Sample," *Science*, 167, 707, (1970).
- Hagfors, T., in Physics and Astronomy of the Moon, Z. Kopal, ed., to be published, (1970).
- Hagfors, T., J.L. Green and A. Guillén, "Determination of the Albedo of the Moon at 6 Meters," *Astronomical Journal*, 74, 1214, (1969).
- Hansen, O.L. and D.O. Muhleman, to be published, (1970).
- Jaffe, L.D., "The Surveyor Lunar Landings," *Science*, 164, 775, (1969).
- Kuiper, G.P., "Interpretation of Ranger VII Records, Communication No. 58, Lunar and Planetary Lab.," University of Arizona, 4, 18, (1966).

- Lincoln Laboratory Final Report: "Radar Studies of the Moon," V. 2, Massachusetts Institute of Technology, (1968).
- Lunar Sample Preliminary Examination Team, "Preliminary Examination of Lunar Samples from Apollo 12," *Science*, 167, 1325, (1970).
- McCord, T.B., "Color Differences on the Lunar Surface," Ph.D. Dissertation, California Institute of Technology, Pasadena, (1968).
- McCord, T.B., "Spectral Reflectivity of the Moon," in preparation, (1969).
- McCord, T.B. and T.V. Johnson, "Relative Spectral Reflectivity 0.4 to 1.1 Microns of Selected Areas of the Lunar Surface," *J. Geophys. Res.*, 74, 4395, (1969).
- McCord, T.B., T.V. Johnson, and H.H. Kieffer, "Differences Between Proposed Apollo Sites: 2. Visible and Infrared Reflectivity Evidence," *J. Geophys. Res.*, 74, 4385, (1969).
- Muhleman, D.O., W.E. Brown, Jr., L. Davids, J. Negus de Wys, and W.H. Peake, "Lunar Surface Electromagnetic Properties," in Surveyor Program Results, NASA SP-184, pp. 203-270, (1969).
- Murray, B.C. and R.L. Wildey, "Surface Temperature Variations During the Lunar Nighttime," *Astrophys. J.*, 139, 743, (1964).
- Oberbeck, V.R. and W.L. Quaide, "Genetic Implications of Lunar Regolith Thickness Variations," *Icarus*, 9, 446, (1968).
- Petit, E., "Radiation Measurements on the Eclipsed Moon," *Astrophys. J.*, 91, 408, (1940).
- Petit, E. and S.B. Nicholson, "Lunar Radiation and Temperatures," *Astrophys. J.*, 71, 102, (1930).
- Ross, H.P., "A Simplified Mathematical Model for Lunar Crater Erosion," *J. Geophys. Res.*, 73, 1343, (1968).
- Scott, R.F. and F.I. Roberson, "Soil Mechanics Surface Sampler," in Surveyor Program Results, NASA SP-184, pp. 171-180, (1969).
- Shoemaker, E.M., R.M. Batson, H.E. Holt, E.C. Morris, J.J. Rennilson, and E.A. Whitaker, "Observations of the Lunar Regolith and the Earth from the Television Camera on Surveyor 7," *J. Geophys. Res.*, 74, 6081, (1969).

- Shoemaker, E.M., M.H. Hait, G.A. Swann, D.L. Schleicher, D.H. Dahlem, G.G. Schaber, R.L. Sutton, "Lunar Regolith at Tranquillity Base," *Science*, 167, 452, (1970).
- Shoemaker, E.M. and R.J. Hackman, "Stratigraphic basis for a Lunar Time Scale," in *The Moon - Symposium of the International Astronomical Union*, Z. Kopal and Z. K. Mikhailov, eds. Academic Press, New York, pp. 289-300, (1962).
- Shorthill, R.W. and J. M. Saari, "Infrared Observations on the Eclipsed Moon," Z. Kopal, ed., to be published, (1970).
- Silver, L.T., "Uranium - Thorium - Lead Isotopes in Some Tranquillity Base Samples and Their Implications for Lunar History," to be published in *Geochimica et Cosmochimica Acta*, (1970).
- Sinton, W.M., "Temperatures on the Lunar Surface," in *Physics and Astronomy of the Moon*, Z. Kopal, ed., Academic Press, New York, pp. 407-428, (1962).
- Trask, N.J., "Size and Spatial Distribution of Craters Estimated from Ranger Photographs," in *Ranger VII and IX, Part II: Experimenters' Analyses on Interpretations*, NASA Tech. Rpt. 32-800, Jet Propulsion Laboratory, Pasadena, California, pp. 289-324, (1966).
- Troitsky, V.S., "Investigations of the Surfaces of the Moon and Planets by Thermal Radiation," *Radio Science*, 69D, 1585, (1965).
- Turkevich, A.L., W.A. Anderson, T.E. Economou, E. J. Frangote, H.E. Griffin, S.L. Grotch, J.H. Patterson, and K.P. Sowinski, "The Alfa Scattering Chemical Analysis Experiment on the Surveyor Lunar Missions," in *Surveyor Program Results*, NASA SP-184, pp. 271-350, (1969).